

TECHNISCHE UNIVERSITÄT MÜNCHEN
Fakultät für Physik

Diagnostic Applications of Grating-Based X-Ray Phase-Contrast and Dark-Field Imaging

Eva-Maria Prexl

Vollständiger Abdruck der von der Fakultät für Physik der Technischen Universität München zur Erlangung des akademischen Grades einer

Doktorin der Naturwissenschaften (Dr. rer. nat.)

genehmigten Dissertation.

Vorsitzender: Prof. Dr. Ulrich Gerland

Prüfer der Dissertation: 1. Prof. Dr. Franz Pfeiffer

2. Prof. Dimitrios Karampinos, Ph.D

Die Dissertation wurde am 18.01.2021 bei der Technischen Universität München eingereicht und durch die Fakultät für Physik am 30.11.2021 angenommen.

Abstract

In recent years, Talbot-Lau interferometry has created a possibility to extract additional image contrasts from an X-ray image. In addition to the conventional attenuation image, a phase-contrast image and a dark-field image can be obtained. While the phase image is characterized by improved soft-tissue contrast and the dark-field image makes non-resolvable micro-structures visible, the simultaneous availability of the conventional image allows the integration into existing diagnostic routines. The use of three micro structured gratings makes it possible to extract the signals from clinical, i.e. incoherent, polychromatic X-ray sources. Immediately after the new method was presented in 2006, the scientific community started to evaluate possible applications for clinical imaging. Today the method has reached a state where dedicated prototypes for the most promising applications - mammography and lung imaging - have already been presented for first human studies.

The aim of this work is to identify new diagnostic applications of grating-based phase-contrast and dark-field imaging and to evaluate their feasibility experimentally. Two application directions can be distinguished. On the one hand, there are applications whose technical implementation is already possible with the current state of the art, and on the other hand, there are approaches for potential applications which still require technical progress and development of individual components or methods, but which could be made available to large patient groups in the event of successful implementation.

Among the applications with lower technical requirements, the detection of foreign bodies in the extremities was identified. While metallic objects are reliably found in conventional radiography, wood particles often remain undetected and can lead to severe complications in wound healing. With a Talbot-Lau interferometer, however, it is possible to clearly visualize even smallest wood splinters by means of a strong dark-field signal. The simultaneous availability of the conventional image enables identification of metallic particles at the same time.

Further, we discovered that gout-causing crystal depositions produce an enhanced dark-field signal. In conventional radiography it is not possible to visualize these crystals directly. Instead, gout is radiographically only detected at a late stage when irreversible cartilage damage becomes visible. In a diagnostic study with ex-

vivo mice, we showed that the crystal deposits were identified significantly better in the dark-field than in conventional radiography. Here, sensitivity and specificity increased to 100 % when both images - the conventional image and the dark-field image - were available to the radiologists for diagnosis.

Due to the special sensitivity for scattering materials, the dark-field signal offers the possibility to explore new contrast agents for angiography applications. Ultrasonic contrast media consisting of micrometer-sized spheres were identified early on as potential candidates for this purpose. Using a new contrast enhancement approach could provide an alternative to iodine-based contrast media, which can lead to severe side effects or kidney failure in certain patient groups. Previous work has already been able to show experimentally that some of these agents actually produce a strong dark-field signal. In this work, the ultrasound contrast agents available on the market are systematically evaluated for their signal strength, previous research results are summarized and conclusions are drawn for the development of a dark-field contrast agent. While the commercially available agents show very different signal strength and make quantitative experiments difficult due to low stability, so-called PLGA spheres were identified as potential candidates for further investigations.

Additionally, a method has been developed to use the three simultaneous signals for quantitative material decomposition. By that, grating-based computed tomography can provide similar image information as dual-energy imaging, which has been successfully introduced into clinical imaging in recent years. The grating-based approach provides several advantages, whereof the availability of the dark-field image is certainly the greatest. In this work, it is shown how this method can be used to quantify iodine contrast agent and how the threefold image information can assure the diagnosis in an unclear stroke situation.

With the collective of these results, the application spectrum of grating-based phase-contrast and dark-field imaging will be expanded. The two dark-field applications for musculoskeletal imaging of the extremities entail fewer technical requirements and could be made available to affected patients in a timely manner. Although the other two approaches still require further technical development steps in order to allow their use in humans, they open up large medical fields of application which should drive the further development of the method.

The current progress in the field of mammography and lung imaging show us that through continuous technical and methodological development Talbot-Lau interferometry can achieve the prerequisites for approval for medical imaging.

Zusammenfassung

In den letzten Jahren wurde mit der Talbot-Lau Interferometrie eine Möglichkeit geschaffen, zusätzliche Bildkontraste aus einer Röntgenaufnahme zu extrahieren. Neben dem konventionellen Absorptionsbild, kann ein Phasenkontrastbild und ein Dunkelfeldbild gewonnen werden. Während sich das Phasenkontrastbild durch einen verbesserten Weichteilkontrast auszeichnet und das Dunkelfeld nicht auflösbare Mikrostrukturen sichtbar macht, erlaubt die gleichzeitige Verfügbarkeit des konventionellen Bilds die Integration in existierende diagnostische Abläufe. Dabei ermöglicht es eine Kombination aus drei mikrostrukturierten Gittern, die Signale an klinischen, das heißt inkohärenten, polychromatischen Röntgenquellen zu extrahieren. Direkt nach Vorstellung der neuen Methode im Jahr 2006 begann die wissenschaftliche Gemeinschaft, die möglichen Anwendungen für klinische Bildgebung zu evaluieren. Heute hat die Methode einen Status erreicht, bei dem für die vielversprechendsten Anwendungen - Mammographie und Lungenbildgebung - bereits dedizierte Prototypen für erste Humanstudien vorgestellt wurden.

Das Ziel dieser Arbeit ist es, neue diagnostische Anwendungen der gitterbasierten Phasenkontrast- und Dunkelfeldbildgebung mit Röntgenstrahlung zu identifizieren und deren Machbarkeit experimentell zu evaluieren. Hierbei können zwei Anwendungsgruppen unterschieden werden. Auf der einen Seite stehen Anwendungen, deren technische Umsetzung im Rahmen des aktuellen Stands der Technik bereits möglich ist, auf der anderen Seite stehen Anwendungen, die noch einen technischen Fortschritt einzelner Komponenten oder Methoden erfordern, im Falle einer erfolgreichen Umsetzung aber großen Patientengruppen zur Verfügung gestellt werden können.

Unter den Anwendungen mit geringeren technischen Anforderung wurde die Detektion von Fremdkörpern in den Extremitäten identifiziert. Während metallische Objekte in konventioneller Radiographie sicher erkannt werden, bleiben Holzpartikel oft unentdeckt und können zu teils schweren Komplikationen in der Wundheilung führen. Mit einem Talbot-Lau Interferometer ist es dagegen möglich, selbst kleinste Holzsplitter durch ein starkes Dunkelfeldsignal dazustellen. Die gleichzeitige Verfügbarkeit des konventionellen Bildes ermöglicht die simultane Identifizierung von metallischen Partikeln.

Außerdem wurde festgestellt, dass Kristallablagerungen, die Gicht verursachen, ein Dunkelfeldsignal erzeugen. In konventioneller Radiographie ist es nicht möglich, diese Kristalle direkt zu visualisieren. Statt dessen wird Gicht radiographisch erst in einem späten Stadium erkannt, wenn irreversible Knorpelschäden sichtbar werden. In einer diagnostischen Studie mit ex-vivo Mäusen wurde gezeigt, dass die Kristallablagerungen im Dunkelfeld signifikant besser identifiziert wurden, als im konventionellen Röntgenbild. Darüber hinaus stiegen Sensitivität und Spezifität auf 100 % an, wenn den Radiologen beide Bilder - das konventionelle Bild und das Dunkelfeldbild - für die Diagnose zur Verfügung standen.

Durch die besondere Sensitivität für streuende Materialien bietet das Dunkelfeldsignal die Möglichkeit, neue Kontrastmittel für Angiographieanwendungen zu erforschen. Als potentieller Kandidat hierfür wurden bereits früh Ultraschallkontrastmittel identifiziert, die aus Mikrometer großen Kügelchen bestehen. Damit könnte eine Alternative zu den bisher verwendeten iodhaltigen Kontrastmitteln geschaffen werden, die bei bestimmten Patientengruppen zu schweren Nebenwirkungen oder zu Nierenversagen führen können. Es konnte bereits in vorangehenden Arbeiten experimentell gezeigt werden, dass manche dieser Mittel tatsächlich ein starkes Dunkelfeldsignal erzeugen. In dieser Arbeit wurden die auf dem Markt verfügbaren Ultraschallkontrastmittel systematisch auf ihre Signalstärke hin evaluiert, bisherige Forschungsergebnisse zusammengetragen und Schlussfolgerungen für die Entwicklung eines Dunkelfeldkontrastmittels gezogen. Während die kommerziell verfügbaren Mittel sehr unterschiedliche Signalstärke aufweisen und quantitative Experimente durch geringe Stabilität erschweren, wurden sogenannte PLGA-Kügelchen als potentielle Kandidaten für weitere Untersuchungen identifiziert.

Darüber hinaus wurde eine Methode entwickelt, um die drei komplementären Signale eines Talbot-Lau Interferometers für quantitative Materialzerlegung verwenden zu können. Dadurch kann mit der gitterbasierten Computertomographie eine ähnliche Bildinformation geliefert werden, wie mit der in den letzten Jahren erfolgreich eingeführten Dual-Energy Bildgebung. Der gitterbasierte Ansatz liefert hierbei verschiedene Vorteile, wobei die Verfügbarkeit des Dunkelfeldbildes sicherlich den Größten darstellt. Hier wird gezeigt, wie diese Methode zur Quantifizierung von Iodkontrastmittel verwendet werden kann und wie die dreifache Bildinformation in einer unklaren Schlaganfallsituation die Diagnose sichern kann.

Diese Ergebnisse erweitern das Anwendungsspektrum der gitterbasierten Phasenkontrast- und Dunkelfeldbildgebung. Die beiden Dunkelfeldanwendungen für muskuloskelettale Bildgebung der Extremitäten bringen geringere technische Anforderungen mit sich und könnten den betroffenen Patienten zeitnah zur Verfügung gestellt werden. Obwohl die beiden anderen Anwendungen noch weitere technische Entwicklungsschritte benötigen, um Humananwendungen zuzulassen, erschließen sie

große medizinische Anwendungsgebiete, die die weitere Entwicklung der Methode vorantreiben sollen.

Die aktuellen Erfolge auf dem Gebiet der Mammographie und der Lungenbildung zeigen, dass die Talbot-Lau Interferometrie durch kontinuierliche technische und methodische Weiterentwicklung die Voraussetzungen zur Zulassung für medizinische Bildgebung erreichen kann.

Contents

1	Introduction	1
2	Theoretical background of X-ray imaging	5
2.1	X-ray interaction with matter	6
2.1.1	Attenuation contrast	6
2.1.2	Phase contrast	8
2.1.3	Dark-field contrast	9
2.2	Grating-based phase-contrast imaging	11
2.2.1	Talbot effect	11
2.2.2	Detection of the refraction angle	12
2.2.3	Interferometry with clinical X-ray sources	13
2.2.4	Stepping curve and signal extraction	14
2.2.5	Signal sensitivity and image contrast	18
2.3	Clinical X-ray imaging components	20
2.3.1	X-ray tubes	20
2.3.2	X-ray detectors	22
2.3.3	CT reconstruction algorithms	23
2.3.4	Clinical protocols and standards	25
3	Review of potential clinical applications	29
3.1	Mammography	30
3.2	Lung imaging	32
3.3	Musculoskeletal imaging	34
3.4	Dark-field contrast agents	35
3.5	Further applications	36
4	Experimental studies	39
4.1	Experimental setups and methods	39
4.1.1	Compact synchrotron source	40
4.1.2	X-ray tube setups	41
4.1.3	Image processing, reconstruction and analysis	44
4.2	Foreign body detection	47

4.2.1	Clinical background	47
4.2.2	Experimental evaluation	48
4.2.3	Conclusion	56
4.3	Gout diagnosis	57
4.3.1	Clinical background	57
4.3.2	Experimental evaluation	58
4.3.3	Conclusion	63
4.4	Dark-field contrast agents	64
4.4.1	Clinical background	64
4.4.2	Experimental evaluation	71
4.4.3	Conclusion	84
4.5	Quantitative material decomposition	86
4.5.1	Clinical background	86
4.5.2	Decomposition approach	88
4.5.3	Monochromatic proof of principle	91
4.5.4	Three-material decomposition at polychromatic X-ray tube sources	102
4.5.5	Conclusion	111
5	Conclusion and outlook	113
	Bibliography	117
	Appendix	147
	List of publications	157

Chapter 1

Introduction

Within the 20th century, numerous diagnostic imaging methods were developed and brought to an advanced technological level. The concepts vary greatly in terms of the underlying physical interaction between the tissue of interest and the used modality. There was big success with endoscopy and microscopy, ultrasound imaging, magnetic resonance imaging, nuclear imaging and of course X-ray imaging. All these techniques have specific advantages in different clinical scenarios (see Sec. 2.3.4). Ultrasound imaging is widely available at low cost and works without ionizing radiation. Magnetic resonance imaging (MRI) can differentiate soft tissues with very high contrast and clarify diagnosis in the field of mammography, joint imaging or brain imaging, among others. Nuclear imaging can provide functional information e.g. in the form of an increased metabolic rate as associated with tumor growth. X-ray imaging is fast and reproducible and is nowadays available at such low radiation doses that it can even be used for screening mammography. Computed tomography (CT) allows to visualize virtual slices of the body in a quantitative and reproducible manner. The method provides a high availability, fast image acquisition and a broad range of applications at moderate cost. Even though the general principle was demonstrated already in 1970, there is still an intense research activity in improving and innovating CT imaging. The first steps in CT development concerned the decrease of the measurement time, the increase of the detector coverage and improvements of the X-ray tube technologies. Later, the availability of higher computational power enabled the implementation of iterative reconstruction methods which started a proper dose reduction race between the vendors of commercial CT systems. The interdisciplinary and innovative research community developed many novel aspects concerning hardware components, tube geometry and image processing concepts including new image reconstruction approaches (see Sec. 2.3.3). But there was never a conceptual change of the interpretation of the physical interaction process which is used for image formation.

Conventional X-ray imaging is based on the reduction of the number of photons depending on the tissue type, resulting in an attenuation image. But X-rays are electromagnetic waves and cannot only be seen as particles but also as waves with a certain intensity and phase. Similar to visible light, the phase of an X-ray wave is changed by different materials and therefore contains potential for another contrast modality. However, the direct measurement of the phase is not possible with X-ray detectors. Within the last few decades, numerous concepts for the indirect detection of the X-ray phase have been proposed and demonstrated. While most of these methods require beam properties which are only provided at large scale synchrotron facilities and are often restricted to biomedical in-vitro or ex-vivo applications, a specific method has been proposed in 2006 which allows the simultaneous extraction of the attenuation contrast, the differential phase-contrast and an additional small-angle scattering signal at compact high-powered X-ray tube sources as used in clinical imaging. This method uses a so called Talbot-Lau interferometer which consists of three high pitch grating structures. In the following years it has been demonstrated that numerous clinical questions could profit from the simultaneous availability of the three image signals.

In this work, a comprehensive overview of the most promising candidates for clinical applications will be given (Chapter 3) after a short introduction into the basic principles of the interferometric imaging method (Chapter 2). The method is now at a stage, where we can witness the introduction of first clinical prototypes in the field of lung imaging, mammography and joint imaging.

An actual implementation of grating-based X-ray imaging into clinical imaging is only realistic if large groups of patients can profit from its application. Therefore, the research focus must lie on pathologies with high incidence, morbidity or mortality to make the further technological development profitable and to gain interest within the industrial sector. At the same time, it is important to explore the full variety of potential applications to provide the benefit for as many patients as possible and to enable synergy effects.

Therefore, different possible clinical applications have been identified and experimentally evaluated within this work (Chapter 4). In the field of musculoskeletal imaging, improved foreign body detection in the extremities and radiographic gout crystal detection have been evaluated. The strong dark-field signal from the relevant materials and the simultaneously available conventional image have the potential to improve and simplify diagnostic routines. To address the important field of cardiovascular imaging, novel dark-field contrast agents have been investigated. The use of well-tolerated microbubbles, which cause a strong dark-field signal, could provide an alternative to iodine-containing contrast agents. In recent years, novel quantitative image representations have been made available by dual-energy or spectral

imaging. Here, we have developed a material decomposition algorithm that makes the same image information available with grating-based imaging within a single CT acquisition.

Thus, several novel application areas of X-ray dark-field and phase-contrast imaging are explored and presented in the following. The applications vary in terms of the technical requirements and the necessary technological developments but could be made available to large patient groups if successfully implemented. With a broad range of potential applications and some key applications as technological drivers, physicians as well as industrial developers should be convinced of the potential of grating-based X-ray imaging.

Chapter 2

Theoretical background of X-ray imaging

X-rays are electromagnetic waves and can be described by photons within the wave-particle duality. The behavior and interaction of photons with their environment is strongly depending on their energy. The electromagnetic spectrum is continuous, but per definition, radiation in the energy range between approximately 100 eV to 200 keV is called X-rays. These photons have the ability to partially traverse matter causing a material dependent transmission signal. This effect, as well as the associated potential for medical imaging was discovered by Wilhelm Conrad Röntgen in 1895 [Als-Nielsen and Des McMorrow, 2011]. Since then, different diagnostic and therapeutic applications have been continuously developed and modern imaging cannot be imagined without radiography or computed tomography (CT). The energy range used for diagnostic imaging ranges from about 20 keV for mammography up to 140 keV for CT examinations. Compared to visible light, to which the human body is adapted evolutionally, higher energy photons are associated with an elevated probability for cell damage. The damage concerns mainly breaks in the DNA strands and the effects range from cell death to cancerogen mutation. Thus, the potential diagnostic benefit must be balanced with the associated risk for every X-ray examination [Russo, 2017].

In the following, the interaction of X-rays with matter will be described briefly to convey the basics of the underlying physical principles. Those interaction processes provide the essential image information but are simultaneously associated with the deposited X-ray dose. The optimization of all imaging components to achieve the highest possible contrast at a minimum X-ray dose is therefore the driving force for technological developments in medical X-ray imaging.

In principle, the properties of electromagnetic fields are described by the Maxwell equations. From this set of equations, the well known wave equation can be de-

rived from which in turn the speed of light in vacuum or the decreased speed of light in a medium can be derived. Various approximations and assumptions allow the derivation of comprehensible equations in the respective range of validity. In order to achieve a high interdisciplinary readability, detailed mathematical derivations are not included within the main part of this thesis. In order to nevertheless present the relationships in a reasonable manner, the relevant terms for a mathematical description are introduced and reference is made at appropriate points to the appendix or to relevant literature.

2.1 X-ray interaction with matter

In principle, X-rays can be absorbed or scattered when interacting with matter. While coherent scattering changes only the direction of the wave vector \vec{k} , incoherent processes change its value, $|\vec{k}| = 2\pi/\lambda$, as well. The introduction of the refractive index

$$n = 1 - \delta + i\beta, \quad (2.1)$$

as a complex number provides a simple formalism to describe the effect of those interactions on the propagation of a plane wave. This can be included into the simplified description of a plane monochromatic wave

$$\vec{E}(\vec{r}) = \vec{E}_0 e^{in\vec{k}\vec{r}} = \vec{E}_0 e^{i\vec{k}\vec{r}} e^{-i\vec{k}\vec{r}\delta} e^{-\vec{k}\vec{r}\beta}, \quad (2.2)$$

propagating in a medium with refractive index n . \vec{E}_0 describes the direction of the electric field and its squared absolute value describes the initial amplitude of the electric field. The first exponential term on the right side of Eq. 2.2 describes the propagation of the incoming wave in the absence of matter (i.e. $n = 1$) [Paganin, 2006]. In the following, we will see that the exponential term with the imaginary part of the refractive index $e^{-\vec{k}\vec{r}\beta}$ describes the influence of attenuation to the propagating wave, while the term $e^{-i\vec{k}\vec{r}\delta}$ describes the phase shift (see Fig. 2.1).

2.1.1 Attenuation contrast

By empirical observation, it can be seen that the intensity I of electromagnetic waves decreases exponentially when traversing matter depending on the material thickness d_z and with a material specific decay constant. This behaviour can be described by the Beer-Lambert law with the material and energy dependent linear attenuation coefficient μ

$$I(d_z) = I_0 e^{-\mu d_z}. \quad (2.3)$$

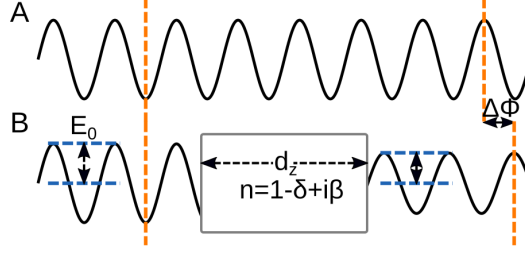


Figure 2.1: Phase-shift and attenuation of an electromagnetic wave. An electromagnetic wave propagates through (A) vacuum or (B) through a medium with refractive index n and thickness d_z . The amplitude of the wave will be reduced due to attenuation in the medium as indicated by the dashed blue lines. Compared to the undisturbed wave, the phase will be changed by the medium as indicated by the dashed orange lines.

Without loss of generality we are assuming that the wave propagates into the z direction. Within the wave-particle dualism, the intensity of an electromagnetic wave is related to the number of photons. The intensity of the wave described by Eq. 2.2 is proportional to its squared amplitude

$$|\vec{E}(d_z)|^2 \propto I(d_z) = I_0 e^{-2k\beta d_z}, \quad (2.4)$$

with $|\vec{E}_0|^2 \propto I_0$ the undisturbed entrance intensity. By relating the imaginary part of the refractive index with the linear attenuation coefficient $\mu = 2k\beta$, the empirical observation of exponential intensity decrease with the thickness of a specific material can directly be described with the refractive index. In general, the intensity of a propagating wave is decreased by all materials along its path according to their respective thickness and the X-ray energy E

$$I(z) = I_0 e^{-\int \mu(z,E) dz}. \quad (2.5)$$

The total attenuation coefficient describes all effects, contributing to the total attenuation. Within the diagnostic energy regime this are absorption by the Photo effect, incoherent Compton scattering and coherent scattering

$$\mu_{\text{tot}} = \mu_{\text{abs}} + \mu_{\text{incoh}} + \mu_{\text{coh}}. \quad (2.6)$$

The contribution of the individual effects depends on the X-ray energy and the properties of the material, for example, the atomic number, the electron density and the mass density. In principle, it is possible to separate the contribution of the individual effects by multiple measurements, for example at different X-ray energies, known as dual-energy or spectral imaging. In Sec. 4.5.2, it will be discussed, how this decomposition can be achieved with a single grating-based phase-contrast CT

(gbpc-CT) measurement.

2.1.2 Phase contrast

As can be seen from Eq. 2.2, the phase shift induced to a plane wave propagating into the z direction after traversing a homogeneous object of thickness d_z is

$$\Delta\Phi = \delta k d_z, \quad (2.7)$$

where the deviation of the real part of the refractive index from 1 is called the refractive index decrement δ . With the real part of the atomic scattering factor in forward direction $f(0)$ ¹, the refractive index decrement can be expressed as

$$\delta = \frac{r_0 h^2 c^2}{2\pi E^2} N f(0), \quad (2.8)$$

with the classical electron radius r_0 , Planck's constant h , the speed of light c , the energy of the incoming wave E and the atomic density N [James, 1954, Willner et al., 2013a]. While the attenuation coefficient can directly be extracted from the measured intensity as described above, it is not possible to measure the phase of an electromagnetic wave, directly. However, there are several methods to transform a relative phase shift into a measurable intensity change. The phase information can for example be encoded within the lateral displacement of the wave front due to refraction.

Fig. 2.2 visualizes the refraction of a wavefront caused by a wedge shaped object. For simplicity, let's assume that this object changes solely the phase of the waves without any attenuation. As the thickness of the object increases in x -direction, the incoming plane wave will experience an increasing phase shift in this direction. Geometrically, the differential phase shift $\partial\Phi(x, y)/\partial x$ can be related to the refraction angle α such that

$$\alpha \approx \frac{\lambda}{2\pi} \frac{\partial\Phi(x, y)}{\partial x}. \quad (2.9)$$

Please find a derivation of relation 2.9 in appendix (B). Fig. 2.2 demonstrates how the refraction translates to an increasing lateral displacement of the wavefront with increasing propagation distance d . The transverse shift Δx of the wave front is

$$\Delta x = d \tan\alpha \approx d\alpha, \quad (2.10)$$

where the right side of the approximation is true in the case of small angles. For

¹The atomic scattering factor f is a measure for the scattered amplitude of an incoming electromagnetic wave by an atom. It is defined for different forms of incoming radiation and involves the Fourier transform of the spatial density distribution of the scatterers, in our case the electrons.

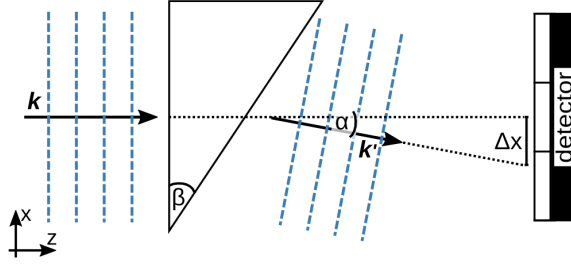


Figure 2.2: Refraction by a wedge. A plane electromagnetic wave propagates through a solely phase-shifting wedge. The dashed blue lines perpendicular to the wave vector \vec{k} mark positions of equal phase of the incident electromagnetic wave. With increasing thickness of the wedge, the induced phase shift increases. Thereby, the wavefront is refracted by an angle α . This angular deflection causes a lateral displacement Δx of the wavefront. This displacement increases with increasing propagation distance.

X-rays, typical refraction angles are in the order of nano- to micro-radians. By increasing the propagation distance d , the lateral displacement Δx can be increased (see Eq. 2.10). However, for medical applications, the distance between patient and detector can not be changed freely and the pixel resolution of medical detectors lies between $50 - 70 \mu\text{m}$ for mammography and $0.5 - 2 \text{mm}$ for computed tomography so that the direct detection of refraction angles is not possible. The implementation of a Talbot interferometer overcomes these limitations and allows the measurement of the phase-shift with clinical X-ray detectors. The implementation of an additional Lau-grating even enables phase-contrast imaging with diagnostic X-ray sources. The basic principles of Talbot-Lau interferometry will be described in the next section (Sec. 2.2.)

2.1.3 Dark-field contrast

Conventional X-ray tubes emit, similar to conventional light bulbs, a broad spectrum of X-ray energies. Additional to this so-called temporal incoherence, the source spots of those X-ray tubes are extended and cause spatial incoherence. Coherence is a property of waves that is defined by spatially and temporally consistent oscillation properties except for a constant phase shift. This is the crucial condition for interference effects to occur within the Talbot-Lau interferometer. The visibility of an interference pattern is defined as the ratio of intensity maxima and minima of the pattern

$$V = \frac{I_{max} - I_{min}}{I_{max} + I_{min}}, \quad (2.11)$$

and can be used to quantify the degree of coherence within an interferometer. Materials with rough surfaces or with strong electron density fluctuations cause a local reduction of the beam coherence due to small-angle scattering.

Thus, the decrease of coherence by a sample can as well be used as image contrast. As stated above, conventional X-ray tubes do not provide the necessary beam coherence to visualize this coherence decrease. We will see later that the Talbot-Lau approach of phase extraction allows the visualization of the coherence decrease as a side effect. At this point we anticipate that the method thereby provides access to a further image channel which is related to strong subresolution refractive index fluctuations and is called dark-field contrast in analogy to optical microscopy.

2.2 Grating-based phase-contrast imaging

Conventional medical X-ray imaging is solely based on the decrease of X-ray intensity by different body tissues in comparison to the primary intensity. In this case, the relevant effects can be described with the particle character of X-rays. Here, we will shortly derive how the additional consideration of the wave character of X-rays and related adaptations of the imaging setup can be used to simultaneously extract three different imaging signals - the conventional attenuation, the phase-contrast and the dark-field signal. The basic idea is to imprint a detectable intensity modulation onto the wavefront which can be used as a reference. The measured sample will then cause characteristic alterations to the detected intensity pattern from which three images can be calculated.

Grating-based phase-contrast imaging is based on the Talbot effect, which describes the phenomenon that a periodic attenuating or phase shifting structure can cause a periodic intensity oscillation at specific distances downstream of the structure. This intensity pattern is then used to visualize the lateral displacement caused by an object's phase-shift as described in Sec. 2.1.2. As the lateral displacement is too small for direct detection with clinical imaging components, another grating is used within the so called stepping approach. By subdividing the large source spot into a series of thin line sources by a third, highly attenuating source grating, interferometry becomes possible at spatially incoherent high-power X-ray tube sources. The arising image signal allows the simultaneous extraction of the phase-contrast and dark-field signals as well as the conventional attenuation image. The mathematical description can be derived from the theory of wave propagation. In the following, the relevant phenomena for Talbot-Lau interferometry will be described while a short mathematical description is given in Appendix A.

2.2.1 Talbot effect

Many phenomena of electromagnetic waves can be described by geometrical optics. The wave character is then neglected and only the paths of light rays which are defined by the normal on the plane of constant phase are tracked. While this simplified interpretation allows the description of many optical phenomena, it can not describe diffraction effects. Such a situation is given for the Talbot effect which is used for the here described grating interferometry approach. The effect was first observed for visible light, where a periodic attenuating object caused a periodic intensity pattern at certain distances [Talbot, 1836]. As those intensity patterns have the same shape as the attenuating object, the effect is often referred to as self-imaging effect. In Appendix A it is derived with Fresnel propagation that the

distances d_T where the self image appears are defined by the wavelength λ and the period p of the attenuating object (from here on called a grating) such that

$$d_T = \frac{2p^2}{\lambda}. \quad (2.12)$$

By that, the region behind an illuminated periodic structure is covered with periodic intensity modulations, denoted as Talbot carpet. Compared to the original Talbot interferometer, the setup can be adapted for medical imaging with X-rays in the following ways: 1) By using a phase-grating (G1) instead of an attenuation grating. This provides similar intensity modulations at certain distances depending on the respective phase shift induced by the grating material. These distances are fractions of the Talbot distances and are therefore called fractional Talbot distances. By using materials with very little attenuation, most of the primary X-ray flux is available for imaging other than with the original attenuation gratings. 2) The cone beam geometry of a conventional X-ray tube source causes a geometric magnification M which must be considered. By that the period of the interference pattern is stretched within the image plane by this factor. But also the periodicity in propagation direction is scaled with the geometric magnification ($d_T^{\text{Cone}} = Md_T$).

2.2.2 Detection of the refraction angle

The intensity modulation created by the Talbot effect can be used as a reference for the quantification of the refraction angle. Fig. 2.3 illustrates how a phase-gradient causes a lateral displacement of the Talbot self image. By combining Eq. 2.7, 2.9 and 2.10 it can be seen that this lateral displacement after a propagation distance d encodes the first derivative of the refractive index decrement in the x-direction

$$\Delta x = d \frac{\partial}{\partial x} \int \delta(x, y, z) dz. \quad (2.13)$$

Here, we have included the three-dimensional position dependency of the refractive index decrement and proceeded from the discrete phase change to a differential one. However, for diagnostic X-ray energies, the refractive index decrement is in the order of $10^{-8} - 10^{-6}$ such that long propagation distances would be necessary in order to directly resolve the shift which is not feasible with clinical imaging components for dose relevant imaging. Instead, an additional grating with highly absorbing bars can be used within the so called phase-stepping approach. This analyzer grating (G2) must be placed at the position where the self image of the phase grating appears (one of the fractional Talbot distances). If the grating period of this grating matches the period of the intensity pattern, movement of this grating

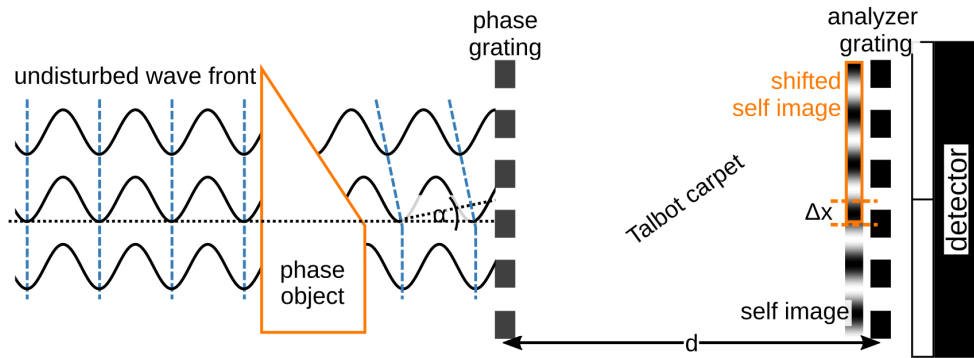


Figure 2.3: Detection of the refraction angle with a Talbot interferometer.

A plane incoming wavefront is refracted by the wedge shaped part of a purely phase shifting object. At the fractional Talbot distances, intensity modulations appear and form the Talbot carpet (not displayed here for the sake of clarity). The deflection of the wavefront causes a lateral displacement Δx of the self image at the respective position in the G2 plane. The analyzer grating is placed at the position of the self image and its period is chosen to match the period of the self image.

over one period in discrete steps will cause a measurable intensity modulation (see Fig. 2.5A). If the position of the grating bars matches the position of high intensity, all intensity will be blocked and the detector signal is at a minimum. If the grating position matches the intensity profile of the pattern, all intensity can pass and the detector signal will be at a maximum.

2.2.3 Interferometry with clinical X-ray sources

Interferometric effects rely on a consistent phase position of the involved X-rays as otherwise spatially stationary superposition as seen at the Talbot distances would not be possible. This property of an X-ray beam is described by its coherence. One can differentiate the longitudinal or temporal coherence which is decreased with increasing spectral width and the spatial coherence which is decreased with increasing source width [Als-Nielsen and Des McMorrow, 2011]. In comparison to synchrotron sources with small spectral bandwidth and high transverse coherence at the position of the experimental setups, conventional diagnostic X-ray sources come with a large source size and a broad spectrum. Fig. 2.4A visualizes how such an extended source blurs the interference pattern and causes its rapid disappearance with increasing source size [Patorski, 1989]. For the Talbot effect with X-rays, a transverse coherence length in the order of the period of the phase grating is necessary in stepping direction to avoid that the interference pattern vanishes due to excessive source blurring [Pfeiffer et al., 2006b, Engelhardt et al., 2008, Weitkamp et al., 2005]. By considering the distance of two points in the extended source which cause destructive interference at the analyzer plane, Bech [Bech, 2009] gave

an estimation for the upper limit of the source size as $s = lp_2/2d$ with l being the distance between source and phase grating. Thus, the source size must be in the order of a few micrometers, which is not the case for high power clinical X-ray tubes.

To decrease the source size without decreasing the source power, Pfeiffer et al. [Pfeiffer et al., 2006b] suggested to place a further attenuating grating with period p_0 close to the X-ray tube anode to create an array of individual slits, each with a sufficient transverse coherence. While these slits provide individually enough coherence, they are still mutually incoherent and can in principle mutually decrease the visibility of the interference pattern. By designing the interferometer such that

$$p_0 = p_2 \frac{l}{d}, \quad (2.14)$$

the size of each individual slit is projected onto the analyzer plane such that they contribute constructively to the image formation process (see Fig. 2.4B). By that, the necessary transverse coherence for Talbot imaging can be provided along the periodic grating structure in combination with high powered X-ray tubes as used for medical imaging. The three grating configuration is called Talbot-Lau interferometer in reference to the experiments of Ernst Lau who found interference effects with incoherent illumination of a double grating arrangement [Lau, 1948]. His work has been repeated and extended in different studies leading to the above definition of the coherence condition [Jahns and Lohmann, 1979, Sudol and Thompson, 1981, Paturski, 1989]. For the temporal coherence, which is limited by the spectral width it was found by numerical simulation that the lateral fringe visibility stays high also for conventional broad X-ray spectra while the polychromatic effects smear out the intensity fluctuations in propagation direction [Engelhardt et al., 2008]. The latter effect actually softens the restriction to the exact fractional Talbot distance. The contrast of the intensity modulation is a quality parameter of the respective interferometer and is described by its visibility (as defined in Eq. 2.11). By that, the Talbot-Lau interferometer allows the simultaneous extraction of three image signals with a conventional X-ray source: attenuation, differential phase shift and visibility decrease (or dark-field). The respective signal extraction via the phase-stepping approach will be described in the next subsection.

2.2.4 Stepping curve and signal extraction

The phase stepping approach allows the detection and quantification of the otherwise unresolvable lateral displacement of the Talbot interference pattern together with the conventional attenuation image and the novel dark-field image. A movement of the analyzer grating over one period of the intensity pattern in several

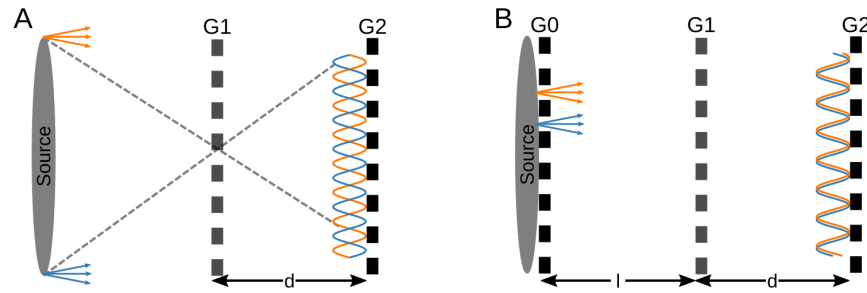


Figure 2.4: Effect of the source size on interferometric effects. (A) An extended source will cause a magnified image of a point in the detection plane as indicated by the dashed gray lines. Each point in the extended source contributes to the formation of the Talbot self image with a different lateral position. In total this leads to an effective blurring of the interference pattern as indicated by the blue and orange curves. (B) An additional highly absorbing source grating G_0 transforms the extended source to a series of thin line sources. These lines emit still mutually incoherent X-rays. By adapting the period of G_0 to the period of the self image at the position of G_2 , each individual slit will contribute constructively to the interference pattern as indicated by the blue and orange curves. Figure partly adapted from [Scherer, 2015]

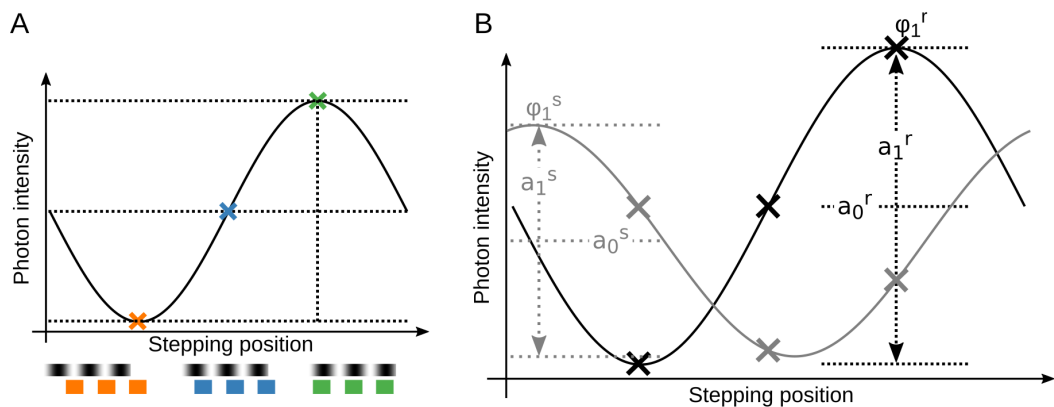


Figure 2.5: Signal extraction from a phase stepping curve. (A) Lateral movement of the analyzer grating over one period of the Talbot self image causes a sinusoidal signal which is a result of the convolution of the source profile, the intensity pattern and the attenuation profile of the analyzer grating. (B) Comparison of this stepping curve from a reference measurement without sample (r , black curve) and a measurement with sample (s , gray curve), allows the extraction of three image signals. The mean intensity a_0 represents the X-ray attenuation, the relative shift φ_1 of the curve is related to the differential phase-shift and the decrease of the amplitude a_1 represents the decrease of beam coherence used for the dark-field image.

discrete steps will cause a periodic intensity modulation in every detector pixel (Fig. 2.5A). The signal is hereby a convolution of the source shape (G0), the Talbot pattern and the attenuation profile of the analyzer grating G2. For a Talbot-Lau setup at a conventional polychromatic X-ray source, it has been found that the signal can be well approximated by the first two terms of a discrete series of cosine functions [Chabior, 2011]. The measurable intensity I_{p_x, p_y} within one detector pixel (p_x, p_y) is then

$$I_{p_x, p_y}(x_g) \approx a_0 + a_1 \cos\left(\frac{2\pi}{p} x_g - \varphi_1\right), \quad (2.15)$$

with x_g the respective grating position, p the period of the interference pattern and φ_1 the phase position of the stepping curve. From a full sampling of this so-called stepping curve, the three coefficients a_0 , a_1 and φ_1 can be extracted by Fourier analysis, for example by a fast Fourier transform algorithm (FFT). The measured intensity oscillation I_n within N phase-stepping positions can then be described by the Fourier coefficients with $k = 0$ and $k = 1$

$$c_k = \frac{1}{N} \sum_{n=0}^{N-1} I_n \exp\left(\frac{2\pi i}{N} nk\right). \quad (2.16)$$

Here, the offset of the stepping curve is provided by the zeroth coefficient $a_0 = c_0$. The amplitude a_1 is given by the first Fourier coefficient $a_1 = 2|c_1|$. And the phase of the stepping curve is given by the argument of the first Fourier coefficient $\varphi_1 = \arg(c_1)$ [Chabior, 2011]. From these coefficients, three different image contrasts can be generated by comparing a sample measurement with a reference scan without sample in the beam path (see Fig. 2.5B). In the following, the sample scan is marked by the superscript s and the reference scan is denoted by the superscript r .

Attenuation signal The conventional attenuation signal is related to the mean intensity value of the stepping curve. This is plausible in the way that it means to evaluate the intensity at the detector as if (on average) no gratings were in the beam ². As the cosine function varies periodically between -1 and 1, its influence cancels out by averaging. The signal transmitted by the sample relative to the signal in the reference scan is therefore

$$T_{p_x, p_y} = \frac{a_0^s}{a_0^r} = e^{-\int \mu(x, y) dz}. \quad (2.17)$$

And the related attenuation $A_{p_x, p_y} = 1 - T_{p_x, p_y}$.

²Of course, the gratings absorb a part of the primary intensity similar to a filter that shapes the spectrum. This must be considered for performance comparisons with conventional X-ray imaging.

Differential phase signal A differential phase-shift of the wave-front $\partial\Phi/\partial x$ causes a lateral shift of the stepping curve due to refraction which can be extracted from the relative phase-position of the stepping curve

$$\Delta\varphi = \varphi_1^r - \varphi_1^s \quad (2.18)$$

The phase shift of the stepping curve is thereby related to the first derivative of the refractive index decrement along the stepping direction

$$\Delta\varphi = \frac{2\pi}{p_2} d\alpha = \frac{2\pi}{p_2} d \frac{1}{k} \left| \frac{\partial\Phi}{\partial x} \right| = \frac{2\pi d}{p_2} \frac{\partial}{\partial x} \int \delta(x) dz. \quad (2.19)$$

Due to the periodicity of the signal, the phase shift can only be measured in the interval from $-\pi$ to π . Larger values caused by larger refraction angles cause phase-wrapping artefacts. This effect can be avoided by either decreasing the interferometer sensitivity (and thereby decreasing the lateral shift) or by avoiding strong refractive index decrement gradients. For biological samples, phase wrapping at the surface of the sample can be avoided by immersing the sample into water during the measurement. For strong gradients inside the samples, phase wrapping must be corrected by image processing or by spectral corrections [Rodgers et al., 2018, Jerjen et al., 2011, Epple et al., 2013].

Dark-field signal Besides the mean value a_0 and the phase position φ_1 , a harmonic oscillation is described by its amplitude a_1 . The amplitude is related to the interferometer's visibility as its potential to separate intensity maxima and minima

$$V = \frac{I_{max} - I_{min}}{I_{max} + I_{min}} = \frac{a_1}{a_0}. \quad (2.20)$$

The dark field signal is defined as the visibility decrease by the sample

$$D = \frac{V^s}{V^r} = \frac{a_1^s a_0^r}{a_0^s a_1^r}. \quad (2.21)$$

The visibility decrease is related to the decrease of the beam coherence due to small angle scattering as caused by materials with strong fluctuations of the refractive index at a length scale far below the detector resolution.

Fig. 2.6 demonstrates the threefold image contrast using the example of two different fruits in grating-based radiography. The attenuation images show strong contrast between the water containing parts of the fruit and the background. The dark-field images show additional details of the dry leaves of the physalis and the inner structure of the kiwi including the seeds. The differential phase-contrast signal is strong at the edges with the typical black and white appearance, indicating a

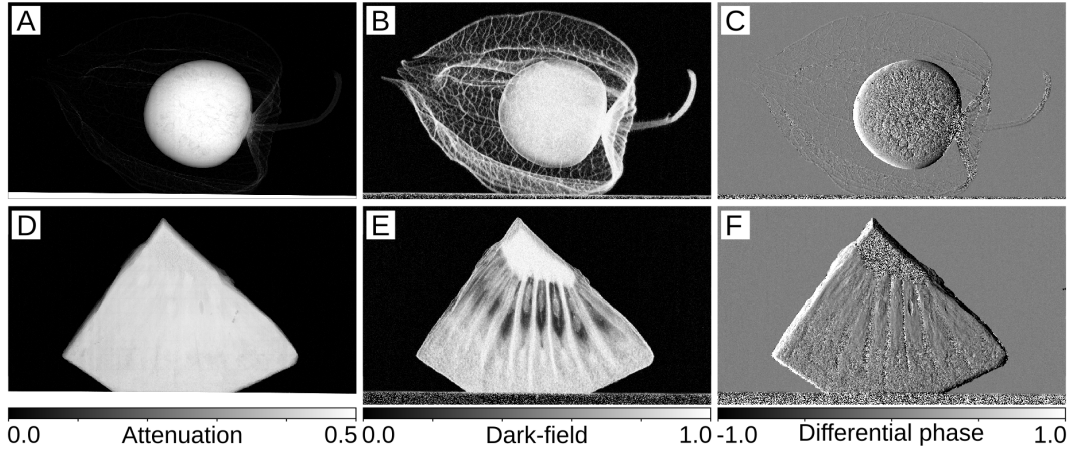


Figure 2.6: Grating-based radiography of a physalis and a kiwi (A, D) The attenuation images show good contrast between the water containing fruits and the background. The leaves and the stem of the physalis are slightly visible as well. (B) The dry leaves of the physalis cause a strong dark-field signal visualizing the leave veins. Also the fine hairs on the stem can clearly be seen. (E) The different parts of the kiwi cause a different dark-field signal allowing a clear visualization of its inner structure. (C, F) The differential phase signal is proportional to the electron density gradient and is therefore strong at material borders. Regions with particularly high noise correlate with regions close to signal saturation in the dark-field image. In these regions, the visibility is reduced so much that the phase signal can not be extracted correctly any more.

negative or positive phase gradient.

2.2.5 Signal sensitivity and image contrast

To evaluate the performance of grating-based X-ray imaging, it is necessary to quantify the ability to differentiate materials and structures. Grating-based CT imaging provides access to the attenuation coefficient, the electron density and to the linear diffusion coefficient. The attenuation signal is equivalent to the signal from conventional attenuation imaging without an interferometer (besides the beam attenuation and filtration due to the gratings). Especially the analyzer grating G2 influences the image result as it absorbs up to half of the photons directly before the detector plane. The other two gratings have a similar effect as a spectral beam filter if the sample is positioned behind the G1 grating. Besides that, the attenuation signal is not influenced by the interferometer parameters.

The phase-signal on the other hand is strongly dependent on the interferometer geometry. The differential phase shift is measured in form of the lateral displacement of the interference pattern, therefore the signal scales with the period of the analyzer grating and the propagation distance $\Delta\varphi \propto 2\pi d/p_2$. The geometric signal amplification is at a maximum if the sample is at the position of the G1 grating

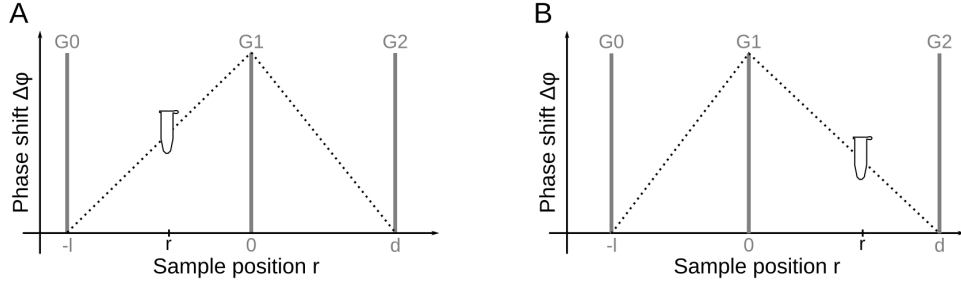


Figure 2.7: Position dependence of the phase-contrast signal. The measured phase shift of the stepping curve $\Delta\varphi$ decreases linearly with increasing sample to G1 distance. The signal drops to zero for a sample position within the G0 or G2 plane in the conventional ($l > d$) geometry (A) as well as in the inverse geometry ($l < d$) (B). The little reaction tube marks an exemplary sample position in sample-before-grating configuration (A) and in grating-before-sample configuration (B). Figure adapted from [Chabior, 2011]

and the measured signal decreases linearly when moving the sample away from the G1 grating in a realistic configuration (see Fig. 2.7). Thus, the phase sensitivity decreases linearly with increasing sample to G1 distance r , with decreasing propagation distance d and with increasing period p_2 [Chabior, 2011]. As in conventional attenuation imaging, the discrimination of two materials is possible if the signal difference is stronger than the noise level. The image noise in phase-contrast CT images is dominated by low spatial frequencies. Therefore sufficiently small pixel sizes are necessary in order to benefit from the improved soft-tissue contrast [Rau-pach and Flohr, 2011, 2012].

Also the dark-field signal decreases with increasing sample to G1 distance but in a non-linear way (sensitivity $S \propto 2\pi^2 d^2 / p_2^2$). Other than in the attenuation image, the noise level in the differential phase and dark-field images is dependent on the visibility of the reference image [Revol et al., 2010, Engel et al., 2011]. Thus, the image quality in grating-based imaging is not only dependent on the source spectrum and exposure time but also on the interferometer components and geometry and the image acquisition process [Chabior, 2011, Marschner et al., 2017, Weber et al., 2011].

2.3 Clinical X-ray imaging components

The great diagnostic value of X-ray imaging has driven extensive technological development which continues to progress actively. In the following, the basic principle of the most important technical components for X-ray and CT imaging are described together with a short review of the historical steps and the current state of the art. In the end of this section, an overview over the technical parameters and the dose restrictions for clinical image acquisition is given.

2.3.1 X-ray tubes

Principles of X-ray generation A diagnostic X-ray spectrum consists of two main parts: the continuous Bremsstrahlung and the characteristic peaks (Fig. 2.8). For the generation of X-rays, electrons are set free by thermionic emission from a heated filament similar to a light bulb. The electrons are then accelerated in a high-voltage field toward the X-ray target in the anode where the two parts of the spectrum are produced. Deceleration of the electrons in the field of the target material's atoms causes the emission of the continuous Bremsstrahlung. Due to energy conservation, the maximum photon energy is given by the acceleration voltage U_{acc} such that $E_{ph}^{max} = eU_{acc}$. Additionally, if the energy of the incoming electron exceeds the binding energy of an electron of the target material, the electron can leave the atomic union. Its position in terms of the atomic shell model will be filled by an electron from a higher energy state. The energy difference is then emitted as a photon, which contributes to the spectrum with its characteristic energy. The resulting energy peaks within the spectrum are characteristic for the respective target material [Als-Nielsen and Des McMorrow, 2011].

Historical developments While W.C. Roentgen used a gas discharge tube when he first observed X-rays in 1895, W.D. Coolidge developed a new tube which was based on the above described principle of an emission cathode and a high voltage acceleration of the electrons toward an anode. This method decoupled the filament current from the high voltage but could only be operated up to a power of 1 kW. The process of X-ray production is extremely inefficient: only about 1 % of the primary energy is converted to X-rays, the rest is converted to heat or lost due to back scattering. The ultimate limiting factor in X-ray tube power is therefore always the organization of heat dissipation. A huge step forward was the technical realization of a rotating anode plate to distribute the heat over a larger area. Optimization of X-ray tubes for diagnostic imaging involves numerous aspects which also depend on the respective application mode or organ system of interest. In any case, systematic

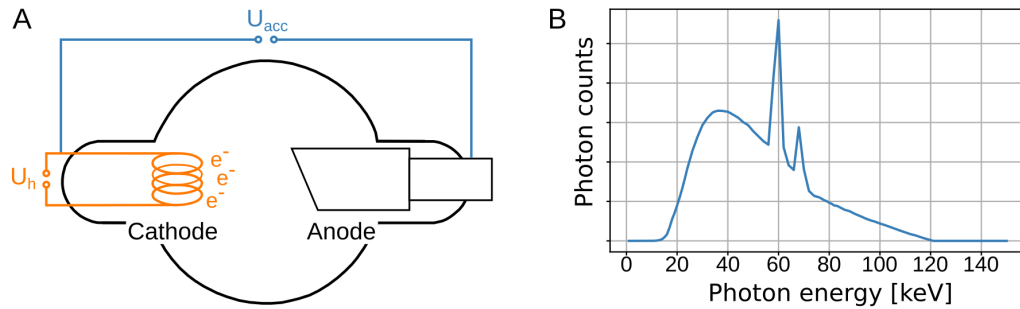


Figure 2.8: X-ray tube source. (A) An X-ray tube consists of an evacuated tube containing a heated cathode that emits electrons due to thermionic emission. The electrons are accelerated toward an anode within a high voltage field. The interaction of the electrons with the anode material produces X-rays. (B) The spectrum of a tungsten anode comprises a broad distribution of photons (Bremsstrahlung) and two strong characteristic peaks. The acceleration voltage (here 120 kV) defines the maximum photon energy.

beam collimation to the active detector area is mandatory to avoid unnecessary radiation exposure. As the Bremsstrahlung is emitted nearly isotropically into the hemisphere above the focal spot, this causes a further loss of 95% – 99% of the generated radiation due to shielding and collimation. Together with the need for short acquisition times this rises the demand for high-powered X-ray tubes [Als-Nielsen and Des McMorrow, 2011, Behling, 2015].

State of the art CT imaging By constant improvement of the technical components, modern diagnostic X-ray tubes are available with powers of up to 120 kW. The technical limit for the acquisition time is given by the limit on the maximum rotation speed due to centripetal forces on the whole system. Minimum scan times of 0.1 s allow to image the heart at a comparably steady point in its cycle [Pelc, 2014]. However, possible rotation speeds of up to 220 rotations per minute cause centrifugal accelerations of more than 30 g [Shefer et al., 2013]. Depending on the respective task, high voltage generators are operated between 100 W for dental and surgery imaging and more than 100 kW in CT systems [Behling and Grüner, 2018]. Also the source spot size, which limits the achievable image resolution, must be optimized for example between large source spot sizes (1 mm^2) for high flux applications like cardiac or vascular imaging and very small source spots ($150 - 500 \mu\text{m}$ width) for high resolution applications like mammography [Behling and Grüner, 2018].

2.3.2 X-ray detectors

Principles of X-ray detection With the introduction of computed tomography by Hounsfield in 1972, the benefits of digital X-ray imaging became obvious. Since then, a variety of different concepts for digital X-ray detection has been experimentally investigated [Yaffe and Rowlands, 1997, Hoheisel, 2006]. However, the most widely used detector type in diagnostic imaging is the flat-panel detector [Pelc, 2014]. It is based on the availability of large arrays of thin-film transistors. Those arrays are either connected to a combination of a scintillator and a light-sensitive photodiode or directly to an X-ray sensitive photoconductor which convert the incoming X-rays to electric charges in either way. The charge in every pixel is collected for a specific time span and then read out row by row. The charge is therefore proportional to the number of incident X-ray photons and the integration time. As the amount of charge produced by a photon is proportional to its energy, the detected signal is additionally weighted by the involved photon energies. The total readout for these systems is very fast such that they can in principle provide real-time imaging [Kotter and Langer, 2002].

State of the art flat-panel detectors Most of the current commercial CT systems are equipped with scintillator photodiode detectors. To avoid crosstalk between the pixels, the scintillators are individually cut and coated with a reflecting material. The pixel spacing ranges from pixel sizes of about 50 μm for mammography to pixel sizes in the order of 1 mm for computed tomography [Gennaro, 2017, Shefer et al., 2013, Pelc, 2014]. With a detector coverage of about 1 m within the transverse plane, imaging of larger patients is possible. Helical scanning modes and multi row detectors allow true 3D imaging. The number of imaged slices per rotation increased exponentially between 2000 and 2010 from less than 10 to more than 500 slices. Modern detector systems can have up to 320 detector rows which allows for wide coverage and is mostly used for polytrauma assessment in emergency departments or perfusion studies. Conventional CT reconstruction relies on the Beer-Lambert law, assuming that a photon is either absorbed or reaches the detector without interacting with the object. However, for the diagnostic energy range, Compton scattering can be the dominant interaction (causing cupping, streaks or quantitative shifts). Therefore, anti-scatter grids are placed directly in front of the detectors to transform the scattering into attenuation. By that, scattering effects can be reduced by up to a factor of 10 [Shefer et al., 2013].

Toward single photon-counting technology While flat-panel detectors provide many advantageous features like fast readout, high dynamic range and large

area coverage, the current technological developments aim toward the single-photon counting technique. Hereby, the X-ray photons are directly converted to electric charges in a semiconductor material. This sensor material is connected via micro-bumps to the readout electronics in a way that every sensitive element (pixel) has its own readout chain. This allows to process the signal pulse of each photon individually and also to assess its energy which is proportional to the processed pulse height. By that, low pulse height signals (as for example associated with thermal noise in the sensor or electronic fluctuations) can be eliminated by setting a lower threshold. The discrimination of two to eight energy bins, enables spectral X-ray imaging. The separation of single photon events requires fast readout and small pixel sizes [Ballabriga et al., 2016]. In the beginning, the application of the technique for diagnostic radiography or even CT was among others limited due to small spatial coverage or restriction to low X-ray flux. However, constant technical progress has led to first approved commercial radiography systems [Hemdal et al., 2005] and to prototype development research for CT imaging [Schlomka et al., 2008, Steadman et al., 2010, Taguchi and Iwanczyk, 2013, Si-Mohamed et al., 2017]. Apart from increased spatial resolution due to the smaller pixel size ³, the most promising potential lies in the possibility of spectral imaging and material decomposition. This provides access to higher contrast transported by low energy photons via energy weighting, reduction of beam hardening artefacts, calculation of maximum contrast images for iodine enhanced imaging, quantitative material discrimination, identification of fresh bleedings and many more.

2.3.3 CT reconstruction algorithms

While radiography is widely available, works at low X-ray dose and provides fast image acquisition it suffers from superposition along the beam path. This reduces the overall image contrast and can hinder clear diagnosis. The solution for these shortcomings is offered by computed tomography (CT) which is based on a series of angular projections over at least 180° and provides cross-sectional views of the imaged volume.

The fundamental task in CT is the reconstruction of the image slices from the projected attenuation profiles. The first technical realization was presented by G.N. Hounsfield in 1972 with a collimated pencil beam. In 1979, he jointly won the Nobel prize for medicine together with A.M. Cormack who contributed the first mathematical implementation for tomographic reconstruction. The very first reconstruction algorithms were based on iterative algebraic methods which were stressing the limits of available computational power. At that point, reconstruction of a single slice

³pixel sizes of $(0.1 - 0.5 \text{ mm})^2$ are considered for CT prototypes [Willemink et al., 2018]

took several days and was therefore not compatible with clinical work-flows [Buzug, 2011]. These first concepts were soon replaced by the analytical method of filtered back projection (FBP) (see Sec. 4.1.3 and Appendix C). FBP algorithms provide short reconstruction times and had been implemented in all commercial CT systems for four decades [Mileto et al., 2019]. Due to constant improvements of CT imaging components and image quality, the number of annual CT examinations increased steadily. However, this increase implies an increased radiation exposure to society, which is related to an increased risk for cancer attributable to CT. This situation gave rise to an upcoming race between the vendors to decrease the applied dose. Technical adaptations to reduce the X-ray dose include tube current modulations, organ-specific parameter adjustment, beam collimation and beam shaping among others. Image quality can further be optimized with respect to the specific diagnostic question by adapting tube current and voltage, voxel size and reconstruction filters. However, with FBP, a decrease of the photon number directly results in an increase of image noise which prevents further dose reduction [Bittencourt et al., 2011, Zhang and Xia, 2019].

In the mean time, computational capacities have rapidly increased especially with the possibility of parallelization on GPUs. Therefore, iterative reconstruction (IR) methods came back into play with a first introduction to clinical imaging in 2009 [Hara et al., 2009]. These algorithms iteratively optimize a model function according to predefined convergence criteria. Raw image data are projected into the cross-sectional image space and image space data are forward projected yielding artificial raw data. The forward projection step enables the physically correct modelling of the imaging system and the inclusion of prior knowledge. An additional regularization step allows the removal of image noise. Iterative forward and backward projection is performed until the difference between computed and raw data is minimized. It has been demonstrated that IR can reduce the average radiation dose for high contrast applications, like for example chest CT from 2.6 mSv with FBP down to 1.4 mSv [den Harder et al., 2015]. For applications with inherently low image contrast like the detection of liver metastasis, pancreatic malignancies or infarct detection, dose reduction can reduce image quality due to loss of spatial resolution. However, dose reduction in the order of 25 % is still possible [Willeminck and Noël, 2019].

Recent scientific efforts focus on the combination of novel CT imaging concepts with IR algorithms. While dual-energy CT has already made its way into clinical application, photon-counting CT, sparse sampling techniques and of course the usage of artificial intelligence are still subject of active preclinical research.

Especially for the implementation of a grating interferometer into a continuously rotating CT gantry, the incorporation of the interferometric image formation pro-

cesses into the forward model of the iterative reconstruction algorithm provides a possibility to avoid phase stepping and to drastically decrease acquisition times [Ritter et al., 2013, Brendel et al., 2016, von Teuffenbach et al., 2017]. By that, a crucial requirement for a future implementation of grating-based phase-contrast and dark-field imaging for clinical CT is provided.

2.3.4 Clinical protocols and standards

X-ray dose Since the invention of computed tomography, many technological adaptations have caused a dose decrease to levels that allow its widespread diagnostic application today. Especially beam collimation and filtration, adaptation of the X-ray tube current and voltage to the patient size during acquisition and constant improvement of detector technology have contributed to this development [Reiser et al., 2011, Kudo and Takei, 2016]. More recently, the implementation of iterative reconstruction algorithms has led to a further substantial decrease of the necessary dose [Winklehner et al., 2011] as described in the previous section. A typical dose value for a single head CT lies in the range of 1 – 3 mSv, whereas the annual radiation exposure due to natural sources lies in the same range with 2 – 3 mSv. A typical dose value for a thorax radiography lies with 0.1 mSv in the same range as a long distance flight from Germany to Japan which also accounts for up to 0.1 mSv due to cosmic radiation [Bundesamt für Strahlenschutz, 2007a]. The radiation exposure per examination is monitored by the Bfs (Bundesamt für Strahlenschutz) in Germany according to their published diagnostic reference levels, but the individual application of the X-ray dose is determined by the physician in accordance with the clinical indication.

Technical imaging parameters Tab. 2.1 and Tab. 2.2 give an overview over some acquisition parameters recommended for radiographic or CT imaging for different body parts by the Deutsche Bundesärztekammer [Brüggemann, 2007b,a]. While the recommended kVp values for CT are almost the same for the different applications, the range between mammography and skeletal radiography is quite big. For the image resolution, the technical requirements are defined via the size of the structures of interest rather than by a fixed value for the imaging system. In CT, the minimum slice thickness is limited by the axial extent of the detector rows. Uniform image quality for all patients is ensured by a defined image receptor dose, which results in different radiation exposure depending on the size of the patient. Especially for mammography, where the compression of the breast can be painful for the patient, the acquisition time must be minimized. The recommended upper limit for the full rotation time in CT can easily be met by state of the art CT

systems with full rotation times well below 1 s [Pelc, 2014, Shefer et al., 2013].

Comparison of X-ray imaging with other modalities There are three prevalent imaging modalities that are used specifically by clinical radiologists: Ultrasound, magnetic resonance imaging (MRI) and X-ray imaging (in the form of radiography or CT). Depending on the specific task, each of the methods has clear advantages and disadvantages, which maintains the coexistence of all three modalities.

Sonography is an affordable method with high diagnostic value which stands out because it is available everywhere with high flexibility. However, its reliability depends on the experience of the operator restricting the reproducibility. For the examination of adipose patients as well as for discrimination of different fluids, the method reaches its limits. Ultrasound is an invaluable tool for fast and direct examination by the physician but other cross-sectional imaging techniques are often necessary to clarify findings. To enhance the signal in ultrasound, contrast agents can be used which are based on gas-filled microbubbles.

MRI provides excellent three-dimensional soft-tissue contrast for example for examination of the brain or the spinal chord. In principle, it is possible to contrast different materials according to their water content by choosing individually adapted sequences. Some fast sequences allow the application with held breath. However, it is contraindicated for patients with pacemakers or cochlea implants and might be problematic for patients with fresh metallic clips, artificial heart valves and within early pregnancy. Sophisticated equipment and the described contraindications limit the use of MRI in acute diagnostics although the method works without ionising radiation. MRI contrast agents are based on media that change the relaxation time of a specific body tissue. In comparison to X-ray contrast agents, MRI contrast agents imply less risk for allergic reaction but can cause a lethal connective tissue disease [Hasebroock and Serkova, 2009].

Conventional radiography is an important tool for fast and precise assessment of high density structures like teeth, bones or calcifications. The possibility to get high resolution projection images at a reasonable low X-ray dose, high reproducibility and low cost made it the method of choice for mammography screening programs with the possibility to extend the two dimensional information by tomosynthesis. However, real 3D information as provided by CT imaging is necessary for many diagnostic questions. The availability of low-dose and high-resolution CT as well as very fast acquisition times justify its application for numerous diagnostic questions. Even though the soft-tissue contrast is limited due to the atomic number dependence of the interaction mechanism, the combination with contrast agents together with the above mentioned advantages can outperform MRI [Reiser et al., 2011].

The implementation of a Talbot-Lau interferometer into a clinical radiography or CT system would exploit their technical advantages of high accessibility and reproducibility while providing access to novel image information. The simultaneous availability of the conventional attenuation image hereby allows the implementation into established diagnostic routines. This potential has driven extensive research effort since the first presentation of a Talbot-Lau interferometer for conventional X-ray sources in 2006 [Pfeiffer et al., 2006a]. In the following chapter, the most promising candidates for clinical application and the respective chronological developments are reviewed.

Body part	Acceleration voltage [kV]	Visual resolution [Lp/mm]	Image receptor dose [μ Gy]	Exposure time [ms]
Abdomen	80 – 125	≥ 2.4	≤ 5	≤ 100
Angiography	65 – 85	≥ 2.4	≤ 5	≤ 150
Cranium	70 – 85	≥ 2.4	≤ 5	≤ 100
Mamma	20 – 35	≥ 12	≤ 5	≤ 2000
Teeth	≥ 60	≥ 2.4	≤ 200	-
Thorax	110 – 150	≥ 2.4	≤ 5	≤ 40

Table 2.1: Recommended acquisition parameters for diagnostic radiography by the Deutsche Bundesärztekammer. Acceleration voltages vary widely depending on the imaged organ system. The visual resolution is quantified via the resolvable number of line pairs. The assignment of a constant image receptor dose guarantees consistent image quality independent of the patient’s BMI. The upper dose application is however limited by a maximum exposure time.

Body part	Acceleration voltage [kV]	Layer thickness norm./HR*[mm]	Acquisition time [s]
Abdomen	110 – 130	3 – 8/0.5 – 2	$\leq 2/360^\circ$
Cranium	110 – 140	3 – 10/2	$\leq 2/360^\circ$
Pelvis	110 – 130	5 – 10/ -	$\leq 2/360^\circ$
Spine	110 – 130	1.5 – 3/ -	$\leq 2/360^\circ$
Thorax	110 – 130	5 – 8/1 – 2	$\leq 2/360^\circ$

Table 2.2: Recommended acquisition parameters for diagnostic CT by the Deutsche Bundesärztekammer. For CT imaging, recommendations for acceleration voltages for different body parts are almost the same. The layer thickness depends on the available detector system and the chosen reconstruction algorithm and is separately defined for *high resolution (HR) applications. The recommendations include statements on Hounsfield unit windowing for each organ system/diagnostic question. Furthermore, there are recommendations for reconstruction and image processing (convolutional kernels, smoothing/ edge enhancing, etc.).

Chapter 3

Review of potential clinical applications

Since the first realization of phase-contrast and dark-field imaging at a conventional X-ray source, many potential applications have been proposed. These applications range from non-destructive testing [Bachche et al., 2017, Prade et al., 2017, Ludwig et al., 2018], over airport luggage control [Miller et al., 2013] to food quality management [Einarsdóttir et al., 2016]. But the largest research field by far concerns biomedical applications. Many studies examined different biological tissues in grating-based phase-contrast CT with high sensitivity and high resolution. It has been demonstrated that the method is capable of quantitatively analyzing pathological tissues, of giving insights into basic research questions and of providing additional diagnostic information within so-called virtual histology [Sztrókay et al., 2013, Willner et al., 2015, Hetterich et al., 2016, Braunagel et al., 2017, Richter et al., 2017, Birnbacher et al., 2018b, Töpperwien et al., 2018]. Therefore, a compact Talbot-Lau micro-CT could be used for non-destructive histology or for the investigation of removed tissue in surgery control. While the investigation of small tissue samples can provide images with high soft-tissue contrast and very fine resolution without dose constraints, it has always been investigated how the novel combined image contrasts of a Talbot-Lau interferometer can be used for improved in-vivo X-ray imaging in the hospital.

Here, an overview of the previously evaluated potential clinical applications will be given, starting with the first experiments in the respective fields and ranging up to the recent first demonstrations of Talbot-Lau interferometers approved for clinical patient imaging.

3.1 Mammography

Breast cancer is still the leading cancer type in women (5 year prevalence: 30.1%, incidence: 24.2%) and also the leading cancer associated cause of death (15% of all death due to cancer worldwide) [GLOBOCAN, 2019] despite having a good healing perspective if detected in an early state. Therefore, mammography is not only used as a diagnostic tool but also as a screening modality which has been reported to reduce breast cancer mortality by approximately 25% in Europe [Broeders et al., 2012]. However, the combination of little contrast between glandular and tumor tissue, the need for high spatial resolution and the high radiation sensitivity of the breast tissue limit sensitivity and specificity of screening programs. Due to those challenging boundary conditions, breast imaging has been the first and most investigated application for various phase-contrast imaging techniques. The exterior position of the breast leads to a lower required X-ray energy as well as to relaxed geometrical requirements. Together with the already used small pixel sizes, the realization of phase-contrast mammography seemed to be both promising in terms of contrast improvement and realistic regarding the technical implementation. A first clinical in-vivo study with 47 patients was conducted at an Italian synchrotron source [Castelli et al., 2007, Dreossi et al., 2007, Castelli et al., 2011] based on phase-enhancement effects due to free space propagation. The improved image quality was reported to increase the true negative rate which could qualify propagation-based phase-contrast at synchrotron sources for second-level examinations following suspicious findings in screening mammography. Many other approaches like analyzer-based phase-contrast, various interferometric realizations and further propagation-based attempts have successfully demonstrated the potential diagnostic benefit for phase-contrast imaging [Keyriläinen et al., 2010, Bravin et al., 2012, Coan et al., 2013, Auweter et al., 2014]. While these methods are more or less restricted to synchrotron sources with high monochromaticity and spatial coherence, Talbot-Lau interferometry allows to work with conventional clinical X-ray sources and is therefore one of the most promising candidates for phase-contrast enhanced screening mammography. Already in 2011, a first study at a conventional X-ray tube source with freshly dissected mastectomy samples has demonstrated better visualization of mammographic signs [Stampanoni et al., 2011]. While the technical parameters such as field of view (5×5 cm), exposure time (72s) and mean glandular dose (26 mSv) were still far from the clinical requirements, already in 2015, grating-based mammography at conventional sources was demonstrated with parameters close to the clinical requirements (12s exposure time, 2.2 mGy mean glandular dose, field of view still stitched) [Scherer et al., 2015b]. Further it has been proposed, to overcome the anisotropic signal sensitivity by bi-directional

phase-contrast mammography. This has been demonstrated to allow the visualization of fine tumor strands in a freshly dissected cancerous mastectomy [Scherer et al., 2014]. Besides from the contrast enhancement in the phase-contrast image, the additional diagnostic value of the dark-field image has been identified very early. Anton et al. [Anton et al., 2013] and Michel et al. [Michel et al., 2013] discovered a correlation of tumor regions containing unresolvable small microcalcifications with an increased dark-field signal and verified the causality by wave-field simulations. The great significance of microcalcification for detection as well as classifications of breast tumors has motivated various further studies. It has been found that the micro-morphology, which can be related to different pathologies, can be determined by a normalized ratio of the dark-field to attenuation signal strength on a sub-resolution length scale [Scherer et al., 2016b]. On the other hand, a study suggesting the possibility to differentiate Type I and Type II microcalcifications [Wang et al., 2014] has been controversially discussed in the literature [Scherer et al., 2016a, Rauch et al., 2020, Wang et al., 2016]. A recent study has investigated 323 breast microcalcifications with a Talbot-Lau interferometer and found an increased prediction sensitivity (increase by 10%) for the malignancy of calcification associated tumors by a trained model [Rauch et al., 2020]. While early attempts in Japan to build a prototype for clinical Talbot-Lau mammography [Endo et al., 2014, Shibata et al., 2014] remained without publication of the ongoing progress until today, a cooperation of *Philips healthcare* and the Paul Scherer Institute in Switzerland have most recently presented a grating-based mammography system successfully commissioned for in-vivo measurements [Arboleda et al., 2020]. Their approach was to implement a grating interferometer into a commercial mammography system, namely the Philips MicroDose slit-scanning system and to optimize the interferometer parameters within the technical boundary conditions [Roessl et al., 2014, Koehler et al., 2015, Arboleda et al., 2017]. The combination of slit-collimation and photon-counting detector technology allows a low dose operation despite the losses due to the G2 grating at 1.6 mGy for a standardized setting. With a total scanning time of 13.4 s and a full field of view of $26 \times 21 \text{ cm}^2$, the system meets the requirements for clinical mammography. With that, grating-based mammography has now reached a state where its potential benefit can be evaluated in a first in-vivo study rather than by theoretical simulation.

Even if a rigorous estimation of the potential SNR benefit of diagnostic grating-based phase-contrast imaging predicted no benefit from most CT applications, it stated a realistic potential for breast imaging [Raupach and Flohr, 2012]. As this study focused on the comparison of attenuation imaging and phase-contrast imaging but neglected the additional diagnostic value of the dark-field image as well as the benefit from the simultaneous availability of all three signals, further results of

attempts towards the implementation of a grating interferometer into a dedicated breast CT setup can be awaited with great curiosity [GratXray, 2017]. Previous grating-based micro-CT studies demonstrated the potential of the three-fold image contrast for excised breast samples in a parameter setting that is in terms of radiation dose, field of view and exposure time most likely suited for pathological examinations [Grandl et al., 2014, 2015]. By that, the method could be further developed to serve as a source for digital virtual histology.

3.2 Lung imaging

While different studies at synchrotron sources focused on the enhanced phase contrast within the respiratory system [Kitchen et al., 2004, 2005, Hooper et al., 2007, Parsons et al., 2008], the grating-based approach revealed a strong dark-field signal arising from the microstructure of the lung. Here, it has been found that the signal arises at the air-tissue interfaces of the lung alveoli and scales with their total number in beam direction, their individual size and with structural changes. Thus, structural lung diseases that change these properties can in principle be visualized by X-ray dark-field radiography. The first experimental proof of this hypothesis has been performed with excised mice lungs at a compact synchrotron source [Schleede et al., 2012, Meinel et al., 2013a, Schwab et al., 2013]. Schleede et al. could hereby demonstrate that emphysematous and healthy lung tissue can be differentiated by analyzing the ratio of attenuation and dark-field signal. As emphysema is an accompanying effect of chronic obstructive pulmonary disease (COPD), which is a leading cause of morbidity and mortality worldwide [WHO, 2018], those promising proof of principle measurements gave rise to further developments of the method. Soon, the transfer to conventional X-ray sources with a Talbot-Lau interferometer [Weber et al., 2012] and even first in-vivo measurements of mice lungs were presented [Bech et al., 2013]. By that it could be demonstrated that the movements of the heart beat and the breathing cycle cause only minor artifacts and do not lead to a break-down of the phase and dark-field signal. Parallel to the technological progress, the diagnostic potential of the method was evaluated with numerous ex-vivo [Yaroshenko et al., 2013, Hellbach et al., 2016, Yaroshenko et al., 2016] and in-vivo [Meinel et al., 2014, Yaroshenko et al., 2015, Hellbach et al., 2015, 2017, 2018b] small animal studies which could identify pulmonary fibrosis, mechanical ventilation induced lung injury, pneumothoraxes and acute lung inflammation as further candidates for improved diagnostics with X-ray dark-field chest radiography. Furthermore, the detectability of lung nodules in dark-field radiography was investigated. Although first experiments were not able to demonstrate a great ben-

efit for tumor detection [Meinel et al., 2013b], a more recent study presents clear visual proof of the visibility of lung tumor nodules in the dark-field image [Scherer et al., 2017]. Despite this large number of potential applications for diagnostic lung imaging and the great results regarding in-vivo imaging of small animals, it was not clear at this time, if the transfer of the technique to human sized objects and the related higher energies would be possible. Therefore, the presentation of the first Talbot-Lau scanners feasible for ex-vivo and in-vivo dark-field chest radiography of pigs [Gromann et al., 2017b, Hauke et al., 2018] and human cadavers [Willer et al., 2018] can be regarded as a milestone. Further studies have evaluated that the optimal tube voltage for X-ray dark-field chest radiography is in the range of 60 – 70 keV for which the transmission image was shown to provide sufficient image quality at the same time [Sauter et al., 2019] (the recommended tube voltage for conventional chest radiography is 110 – 150 keV, Tab. 2.1). Apart from further technical optimizations [Ludwig et al., 2019, Seifert et al., 2018, 2019], the benefit of dark-field imaging for the diagnosis of emphysema, pneumothorax, pulmonary infiltrates and the ventilation dependent signal have been investigated with in-vivo pigs and human cadavers [Hellbach et al., 2018a, Willer et al., 2018, Fingerle et al., 2019, De Marco et al., 2019]. The technical realization of the first large field-of-view scanners is based on a fringe scanning approach with tiled gratings G1 and G2. While the single sub-tiles have only a size of $5.0 \times 2.5 \text{ cm}^2$, eight of them are arranged under the microscope for both gratings. Instead of phase-stepping, a relative movement between the gratings and the imaged object produces the images with different relative phase positions of the Moiré pattern. By that, an effective field-of-view of $32 \times 35 \text{ cm}^2$ in the patient plane can be achieved. With this approach, a total scan time of 30 – 40 s can be realized. The resulting radiation dose is approximately a factor of 3.6 higher than for a clinical thorax acquisition but provides the conventional attenuation image and the dark-field image at the same time [Gromann et al., 2017b, Willer et al., 2018, De Marco et al., 2019].

All together the promising potential of using the simultaneously produced attenuation and dark-field signal in single projection radiography for lung imaging has stimulated a fast technical development. Less than ten years lie between the first report on emphysema diagnosis with dark-field imaging of excised mouse lungs at a compact synchrotron source [Schleede et al., 2012] and the first demonstration of X-ray dark-field chest radiography with in-vivo pigs and human cadavers [Gromann et al., 2017b, Willer et al., 2018]. Most recently, first insights have been provided into an ongoing large-scale patient study with a dedicated dark-field radiography system [Willer, 2019]. In case of positive results, X-ray dark-field radiography could provide a cost- and dose-effective alternative to CT imaging, which is up to now the gold standard in COPD diagnosis. Especially, if X-ray dark-field radiography was

able to detect early stages of COPD, the patient's perspective could be improved by changing lifestyle habits and by providing early treatments. As there are no causal therapies available for the late stage of this degenerative disease, the possibility to recognize early stages could also motivate further pharmaceutical research.

3.3 Musculoskeletal imaging

Musculoskeletal X-ray imaging mostly focuses on visualization of bone structures and late signs of cartilage damage, as the contrast for the relevant soft-tissues like tendons, ligaments and healthy cartilage is negligible. Therefore, musculoskeletal applications were of particular interest to evaluate the clinical benefit from the improved soft-tissue contrast in X-ray phase retrieval methods [Coan et al., 2010, Donath et al., 2010, Pfeiffer et al., 2013]. Thanks to the the superior soft-tissue contrast in the phase image, it was possible to visualize the surface of healthy cartilage and tendons in cadaver hands as well as in healthy patients in projection [Tanaka et al., 2013] and with a first grating-based CT of an entire ex-vivo human hand [Thüring et al., 2013]. In a subsequent study, Momose et al. [Momose et al., 2014b] presented the first dedicated Talbot-Lau joint imaging setup for preclinical research on patients. With an effective field of view of $49 \times 49 \text{ mm}^2$, the scanner was designed for imaging of the joints of the hand but later results showed images of the knee as well [Nagashima et al., 2014]. In 2020, a first patient study with 70 patients suffering from rheumatoid arthritis (RA) and 55 healthy volunteers was presented [Yoshioka et al., 2020] by this group. They found a significantly reduced cartilage thickness of the metacarpophalangeal joint for the RA patients in the differential phase-contrast image and concluded that Talbot-Lau imaging could be suitable for the detection of early stages of RA. The grating interferometer of the clinical prototype scanner consists of three gratings with periods of 22.8, 4.3 and $5.3 \mu\text{m}$ with intergrating distances of 1.1 and 0.26 m operated with a mean X-ray energy of 28 keV in a fringe scanning approach.

Additionally to the improved contrast for soft tissues in the phase image, it has been reported that the dark-field image reveals information on the microstructure of bone without needing to resolve it directly. Furthermore, the directional dependency of the dark-field signal was found to provide similar information as tensor diffusion imaging in magnetic resonance imaging [Jensen et al., 2010a,b]. By measuring the angular dependence of the dark-field signal in multiple projections, information about the local orientation, the degree of anisotropy and the average size of microstructures have been determined and correlated with mechanical properties of human vertebral bones [Potdevin et al., 2012]. As the measured degree of anisotropy correlates with the state of the trabecular microstructure, the method

has been used to predict the vertebral failure load and to detect osteoporotic changes in the femoral bone [Schaff et al., 2014, Eggl et al., 2015a, Baum et al., 2015]. Besides bones, also the tubules structure of teeth has been visualized by directional dark-field imaging in a non-destructive ex-vivo measurement [Jud et al., 2016]. Further, it has been demonstrated that bone microfractures without dislocation can be identified in directional dark-field imaging [Jud et al., 2017, Jud, 2019].

With the availability of a first approved Talbot-Lau radiography setup for musculoskeletal imaging, clinical studies on further potential applications are possible.

3.4 Dark-field contrast agents

Novel imaging mechanisms offer new opportunities for contrast enhancement. The sensitivity for strong subresolutional refractive index fluctuations in X-ray dark-field imaging provides the potential for an entirely different concept of contrast enhancement. Instead of increasing the X-ray attenuation by injecting high atomic number media like iodine, Arfelli et al. proposed in 2002 to use scattering materials for contrast enhancement in diffraction-enhanced imaging [Arfelli et al., 2002, 2003]. With the identification of microbubble-based ultrasound contrast agents as potential candidates for a physiologically compatible scattering source, they laid the foundation for numerous further experiments. The research on this topic can hereby be subdivided into preclinical or small animal experiments, using physiological contrast media, and extensive theoretical simulation studies. Velroyen et al. first investigated X-ray dark-field contrast enhancement with microbubbles at a conventional polychromatic X-ray tube source. In a comparative study of different commercially available ultra-sound contrast agents they found that despite similar constitution, size distribution and concentration of the microspheres, only one of the three tested contrast agents gave a sufficient dark-field signal [Velroyen et al., 2013]. Later, they demonstrated successful contrast enhancement with microbubbles with an ex-vivo mouse at a conventional X-ray tube setup with a Talbot-Lau interferometer [Velroyen et al., 2015].

In the experimental part of this thesis, the research on potential candidates for X-ray dark-field contrast agents is continued (Sec. 4.2). There, a detailed overview is given on previous findings, on properties of commercially available ultrasound contrast agents and the physiological behaviour of these microbubbles is discussed. With an experimental study, the potential of three different commercially available ultrasound contrast agents for X-ray dark-field signal enhancement is evaluated. Additionally, PLGA spheres are evaluated for their potential for X-ray dark-field signal enhancement.

3.5 Further applications

In addition to the four big applications described above, a large number of smaller promising applications has been discovered and investigated. One of these applications is the differentiation of kidney stones in grating-based radiography. While different chemical types of stones require entirely different treatment, their exact identification is often difficult. However, it has been seen, that the ratio between attenuation and dark-field signal allows a clear differentiation of calcium oxalate and uric acid stones and even mixed types in single projection imaging [Scherer et al., 2015a]. While the dark-field signal is sensitive to the microscopic growth structure, the attenuation image relates the signal to the projected amount of material. Scherer et al. demonstrated the differentiation of kidney stones in X-ray dark-field radiography in a dose compatible setup within an excised fresh pig kidney. With the recent technical achievements towards X-ray dark-field imaging of human-sized objects and cadavers, the transfer of the method to in-situ imaging would be imaginable. Similar experiments have demonstrated the possibility to differentiate struvite and calcium oxalate stones in grating-based tomography [Hu et al., 2017].

In other studies, it was recognized that the simultaneous availability of the three image channels could also be helpful for foreign object detection in food [Nielsen et al., 2013]. An extensive study demonstrated the superior recognition results of various combinations of food and foreign body materials typically found in food processing industry [Einarsdóttir et al., 2016]. In a setup optimization study, it has been seen, that a retained wood splinter in a pig's trotter was clearly visible in dark-field radiography at 0.03 mGy air kerma while it was hardly visible in conventional attenuation [Rieger et al., 2017]. In the course of this thesis, an experimental study was conducted to evaluate the further potential of improved foreign body detection in the human body with grating-based radiography. The detection of foreign bodies in the human hand is evaluated experimentally and the detection limits are explored with a dedicated foreign body phantom (Sec. 4.2).

A further candidate for a clinical application of X-ray dark-field radiography is the diagnosis of gout. Within the experimental part of this thesis, it is investigated whether the dark-field signal from crystal structures within gout deposition can simplify its diagnosis (Sec. 4.3).

Besides from the direct exploitation of an enhanced phase or dark-field signal from specific body parts or pathologies, it is also possible to use the combined information of all channels to calculate further image representations. It will be demonstrated in Sec. 4.5, how the simultaneous acquisition of attenuation, phase and dark-field contrast can be used for three-material decomposition in grating-based CT. This

principle provides similar diagnostic information as lately introduced to the clinical routine by dual-energy imaging with the advantage of the additional dark-field image and direct access to the electron density.

In conclusion, constant research activity has worked out a number of promising clinical applications that would be beneficial for large patient groups. While the big applications like lung imaging and mammography are driving the technical development towards clinical feasibility, the diversity of potential applications as well as the compatibility with existing hardware can increase the clinical acceptance.

Chapter 4

Experimental studies

Within the experimental part of this thesis, grating-based X-ray imaging is applied to different pathologies and diagnostic questions to evaluate the potential benefit of the simultaneous availability of the attenuation, phase and dark-field image. Two groups of applications can be distinguished here, depending on the complexity of the technical realization for the clinical routine.

Foreign body detection and crystal detection for gout diagnosis are two applications with minor requirements regarding the technical components of the interferometer. Therefore, they are candidates for an early clinical implementation. Additionally, the potential for X-ray dark-field contrast agents and for a material decomposition algorithm for the use in high impact markets like vascular imaging and stroke imaging are evaluated. While these applications cover a large range of clinical questions, they require further technological developments before they can be implemented for clinical imaging. By addressing both categories, the entire spectrum of possibilities related with grating-based X-ray imaging should be highlighted.

In the following, the clinical background of these four potential clinical applications is given, the experimental feasibility is evaluated and the expected benefit from the simultaneous availability of the different signals is discussed. The chapter starts with a short description of the experimental setups and methods.

4.1 Experimental setups and methods

For the experimental studies, different X-ray imaging setups were used. The technical components of the Compact Light Source setup and three different X-ray tube setups are described in the following. Subsequently, the different image processing techniques are shortly described. The specific imaging parameters and the applied image processing steps are given in the description of the relevant experimental study.

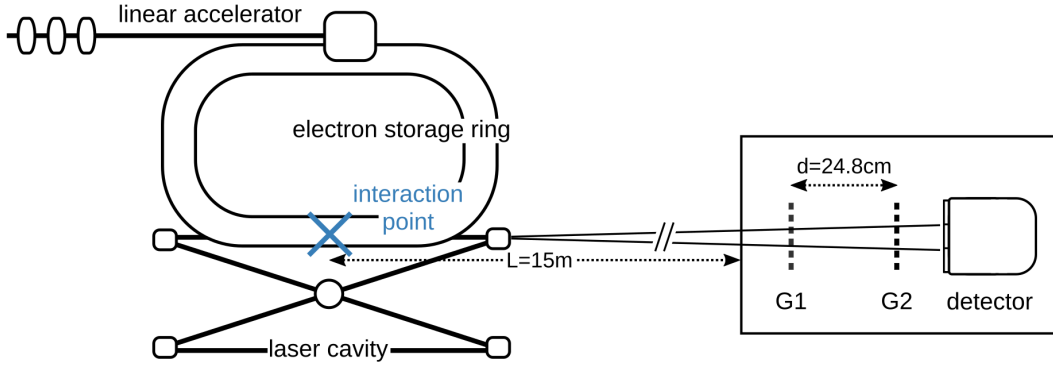


Figure 4.1: Schematic drawing of the Munich Compact Light Source. Electrons are accelerated in a linear accelerator and then injected into an electron storage ring. At the interaction point they collide with laser photons from the laser cavity. X-rays are produced during the collision by the inverse Compton effect. X-rays leave the machine through an exit window and propagate through a beam pipe to the experimental hutch in approximately 15 m distance from the interaction point. The interferometer consists of a phase grating G1 and an absorption grating G2.

4.1.1 Compact synchrotron source

MuCLS - setup A

Working principle: The Munich Compact Light Source (MuCLS) is a novel type of a brilliant laboratory X-ray source based on inverse Compton scattering. It has been developed and produced by *Lyncean Technologies Inc.* (Fremont, California) and is the first commercially sold compact synchrotron source. It is based on the combination of a small electron storage ring with about 4.6 m circumference and a resonantly driven high-finesse laser cavity ($\lambda_{\text{Laser}} = 1064 \text{ nm}$) (Fig. 4.1). Electrons are accelerated to relativistic energies of 29 – 45 MeV in a linear accelerator before injection into the storage ring [Huang and Ruth, 1998, Loewen, 2004].

X-ray photons are produced by inverse Compton-scattering at a defined collision point of laser photons and electrons with a repetition rate of about 65 MHz. By tuning the electron energy in the above given range, the X-ray energy can be selectively changed between 15 and 35 keV. The X-rays are confined to an opening angle of $\pm 2 \text{ mrad}$ before leaving the cavity. In an initial performance characterization, the average flux was determined to $\approx 10^{10}$ photons/s, the source size to $\approx 42 \mu\text{m}$ diameter and the energy bandwidth to $\approx 3\%$. A more detailed description of the working principle and the performance characteristics of the Munich Compact Light Source can be found in [Eggl et al., 2016], [Jud, 2019] and [Günther et al., 2020].

Detector: Images were acquired with a photon counting Pilatus 200K detector (*Dectris Ltd.*, Baden-Daettwil, Switzerland) with a 1 mm thick silicon sensor and a

pixel size of $(172 \times 172) \mu\text{m}^2$. The quantum efficiency at 25 keV for 1 mm silicon is 42.4%.

Interferometer: The grating interferometer used for the here presented experiments is situated at a distance of about 15 m from the X-ray source point. The elliptic field-of-view at this position is $(62 \times 74) \text{mm}^2$. The Talbot interferometer is realized with two gratings: a phase grating (G1) with a period of $4.92 \mu\text{m}$, duty cycle¹ of 0.5 and nickel filling height of $4.39 \mu\text{m}$ and an absorption grating (G2) with period, duty cycle and gold filling $5 \mu\text{m}$, 0.5 and $70 \mu\text{m}$. For the design energy of 25 keV, the phase grating provides a phase shift of $\pi/2$ and the inter-grating distance for the first fractional Talbot order is $d = 24.8 \text{cm}$. The maximum correlation length at the position of G1 is $\zeta_{\text{MuCLS}} = \lambda d/p_2 = 2.46 \mu\text{m}$.

The tunable quasi-monochromatic X-ray energy allows quantitative benchmark or verification measurements as well as low-dose applications or dual-energy measurements [Eggl et al., 2015b, Jud et al., 2017, Eggl et al., 2018, Günther et al., 2020].

4.1.2 X-ray tube setups

The experiments were performed at different laboratory setups in dependence on the relevant setup parameters like tube power, field of view, detector performance and setup availability. A sketch of a typical Talbot-Lau interferometer as used with X-ray tubes is given in Fig. 4.2.

Microfocus tube - setup B

Tube settings: This setup uses a tungsten target X-ray tube (*X-ray WorX SE 160*, Garbsen, Germany), operated at 60 kVp and a power of 150 W. The focal spot size at this power is approximately $100 \mu\text{m}$ in diameter.

Detector: The setup has been used with two different detectors: a Varian Paxscan 2520DX flatpanel detector with a CsI scintillator and a pixel size of $(127 \times 127) \mu\text{m}^2$ and a Varian PaxScan 4030D flatpanel detector (*VARIAN medical systems*, Palo Alto, USA) with a structured CsI scintillator screen and a pixel size of $(194 \times 194) \mu\text{m}^2$.

Interferometer: The interferometer is designed for a mean energy of 45 keV with grating periods of $10/5/10 \mu\text{m}$ for G0/G1/G2, respectively. The inter-grating distance at this energy is $d = l = 90.6 \text{cm}$ and the phase shift induced by the G1 grating is $\pi/2$. The gratings are on silicon wavers of thickness $500/200/150 \mu\text{m}$. The mean flat-field visibility is $27 - 28\%$. The maximum correlation length at the position of the phase grating is $\zeta_{\text{MF}} = \lambda d/p_2 = 2.55 \mu\text{m}$ [Prade et al., 2016, Prade,

¹The duty cycle is defined as the ratio of the slit width between two bars and the grating period.

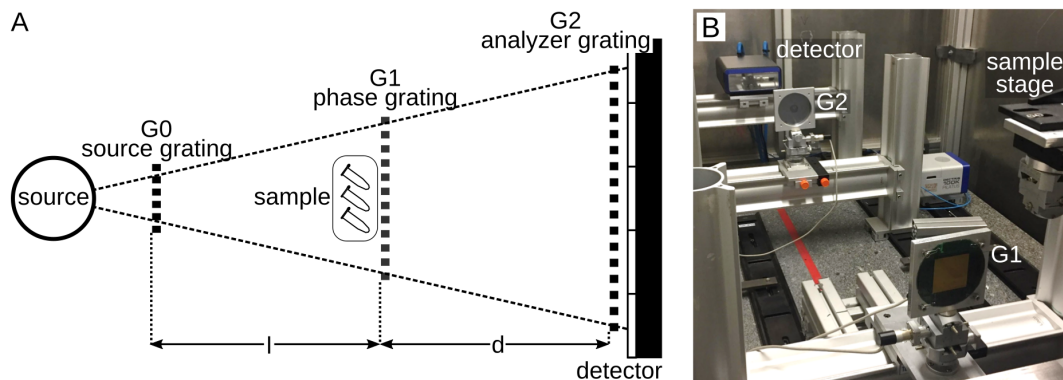


Figure 4.2: Talbot-Lau interferometer at a laboratory X-ray tube. (A) A Talbot-Lau interferometer at an X-ray tube setup consists of three gratings: the source grating (G0), the phase grating (G1) and the analyzer grating (G2). The cone-beam of the X-ray tube causes a geometric magnification which must be taken into account for the interferometer design. The inter-grating distances can be different (asymmetric configuration) or equal (symmetric configuration). The sample can be positioned before or behind the phase-grating. (B) Photograph of Setup C showing G1 and G2, the detector and the sample stage. G0 and the source are not shown on the image.

2017, Schaff, 2017].

The setup provides a comparatively large field of view and a high design energy. It can be used for ex-vivo dark-field and phase contrast studies to evaluate the potential clinical benefit at higher X-ray energies.

Rotating anode - setup C

Tube settings: Within the time frame of this work, the rotating anode tube has been replaced. The old tube was an Enraf Nonius FR-591 tube (*Bruker*, Delft, Netherlands) with a rotating molybdenum anode. It was operated at 40 kV acceleration voltage and 2.8 kW tube power with an effective source size of $(0.3 \times 0.5) \text{ mm}^2$. The new tube uses a rotating molybdenum anode, as well (*MicroMax HF007*, Rigaku Inc., USA). It is operated at 50 kV acceleration voltage with 1.2 kW tube power. The focal spot size at this power is approximately $(46 \times 97) \text{ }\mu\text{m}^2$.

Detector: This setup has been used with three different photon-counting detectors. The first experiments with the contrast agents were performed with the old X-ray tube and a Pilatus 100k detector (*Dectris Ltd.*, Baden-Daettwil, Switzerland) with a pixel size of $(172 \times 172) \text{ }\mu\text{m}^2$ and a 1000 μm thick silicon sensor. All other experiments at this setup were performed with the new X-ray tube. The further contrast agent measurements and the MSU crystal detection experiments were performed with an Eiger 500k detector (*Dectris Ltd.*) with a pixel size of $(75 \times 75) \text{ }\mu\text{m}^2$ and a 450 μm thick silicon sensor. The material decomposition experiments were per-

formed with a Santis CdTe photon counting detector (*Dectris Ltd.*) with a $750\ \mu\text{m}$ thick cadmium telluride sensor and a pixel size of $(75 \times 75)\ \mu\text{m}^2$.

Interferometer: The grating interferometer consists of a symmetric three-grating setup with periods of $5.4\ \mu\text{m}$, gold filling heights of $70/5.2/65\ \mu\text{m}$ and duty cycles of 0.6, 0.55 and 0.65, respectively. The inter-grating distance is $85.6\ \text{cm}$ at a design energy of $27\ \text{keV}$ where G1 provides a phase shift of π . G0 is on a $1\ \text{mm}$ Kapton substrate, G1 and G2 are on a 200 and $500\ \mu\text{m}$ silicon substrate. The mean flat-field visibility is in the range of $27 - 29\%$. The maximum correlation length at the position of the phase grating is $\zeta_{\text{RA}} = \lambda d/p_2 = 7.28\ \mu\text{m}$ [Birnbacher, 2018, Scholz et al., 2020].

The high tube power, small effective pixel size and small phase-grating period enable a high phase sensitivity at acceptable total acquisition times. Thus, this setup can be chosen for applications where a high soft-tissue contrast is required [Grandl et al., 2014, Birnbacher et al., 2016, Hetterich et al., 2016, Braunagel et al., 2017, Birnbacher et al., 2018a,b, Notohamiprodjo et al., 2018, Hellerhoff et al., 2019].

Linescanner - setup D

Tube settings: The actively cooled Philips MRC 0310 ROT GS tube (*Philips Medical Systems*, Hamburg, Germany) is operated at $60\ \text{kV}$ or $70\ \text{kV}$ acceleration voltage with $10.5 - 12\ \text{kW}$ tube power.

Detector: The setup is equipped with a Pixium RF 4343 flat-panel detector (*Trixell*, Moirans, France), with a $600\ \mu\text{m}$ thick CsI scintillator. The detector is operated in a 3×3 binning mode which results in a pixel size of $(444 \times 444)\ \mu\text{m}^2$.

Interferometer: This setup is designed to cover a large field of view of $(32 \times 35)\ \text{cm}^2$ and has a design energy of $45\ \text{keV}$. The grating configuration has been changed within the time frame of this thesis. In the first configuration, the large field of view in lateral direction has been realized by tiling several smaller gratings for G1 and G2. The other direction is covered by moving the interferometer over the detector area in a Moiré scanning approach. The grating periods of G0, G1 and G2 are $68.72\ \mu\text{m}$, $8.73\ \mu\text{m}$ and $10\ \mu\text{m}$, respectively. G0 has a structure height of $240\ \mu\text{m}$ gold on $1\ \text{mm}$ graphite substrate and a duty cycle of 0.7. G1 and G2 are on a 0.525 and $0.5\ \text{mm}$ silicon substrate and have a gold structure height of $> 150\ \mu\text{m}$ gold with a duty cycle of 0.5. The grating configuration is asymmetric with inter-grating distances of $l = 159.9\ \text{cm}$ and $d = 23.1\ \text{cm}$ [Gromann, 2017, Hellbach et al., 2018a]. For the second configuration, the G0 and G1 grating have been replaced. G0 has now a structure height of $215\ \mu\text{m}$ and a period of $10\ \mu\text{m}$. The G1 grating has been replaced by a single phase grating with an area of $225 \times 60\ \text{mm}^2$ with a period of $10\ \mu\text{m}$. The grating configuration is now symmetric with an inter-grating

distance $d = 89.1$ cm The gratings are vertically mounted on the scanning arm such that the samples are lying on a horizontal table [Andrejewski, 2017, Taphorn, 2018]. At this setup, CT imaging is not implemented. The maximum correlation length at the position of G1 is $\zeta_{LS,1} = \lambda/p_0 = 0.642 \mu\text{m}$ for the old configuration and $\zeta_{LS,2} = \lambda d/p_2 = 2.46 \mu\text{m}$ for the new configuration.

With the large field of view, the high design energy and the high tube power, the setup is designed for human chest imaging at clinical compatible acquisition times and dose levels [Gromann et al., 2017a, Willer et al., 2018, De Marco et al., 2019].

4.1.3 Image processing, reconstruction and analysis

Signal extraction

If not stated otherwise, images were acquired via phase stepping as described in Sec. 2.2 and subsequent extraction of the Fourier coefficients by FFT. The number of phase steps was adapted to the interferometer stability and the required photon statistics and is given in the description of each experiment.

A more advanced processing method has been applied for the brain sample measurement in Sec. 4.5.4. The method is based on the minimization of a cost function by variation of the parameters of a statistical model function. By that, the experimental data is fitted and experimental deviations of the stepping positions or the X-ray flux can be compensated [Marschner et al., 2016b, Wang and Han, 2004].

CT reconstruction

In contrast to projection imaging, computed tomography allows the quantitative reconstruction of material quantities in three dimensions. With grating-based CT this are the linear attenuation coefficient, the refractive index decrement and in principle the linear diffusion coefficient.

CT data-sets were acquired by rotating the sample over 360° . The individual signals were processed as described above and subsequently the three image channels were reconstructed independently by filtered backprojection (FBP) with a Hamming filter for the attenuation and dark-field data and a Hilbert filter for the phase data [Pfeiffer et al., 2007]. The attenuation coefficient distribution can directly be reconstructed from the measured transmission signal T as defined in Eq. 2.17

$$p_{\theta,\mu}(t) = -\ln T_\theta(t) = \int \mu(s, t) ds, \quad (4.1)$$

with (t, s) the coordinate system that is rotated by an angle θ compared to the original (x, y) coordinate system such that t describes the detector lines and s the

straight ray path (see Fig. 5.2). The natural logarithm of the transmission signal can be interpreted as the line integral of the attenuation coefficient distribution and can be used as input for the FBP algorithm. More information on the basic principles of tomographic reconstruction and on the used nomenclature can be found in Appendix C.

As the measured differential phase-contrast signal is the relative shift of the stepping curve $\Delta\varphi$, an additional factor must be considered to retrieve the refractive index decrement δ . By rearranging Eq. 2.19 we can see that the projection of the refractive index decrement gradient can be expressed as

$$p_{\theta,\delta}(t) = \frac{p_2}{2\pi d} \Delta\varphi = \frac{d}{dt} \int \delta(s, t) ds. \quad (4.2)$$

For reconstruction of the refractive index decrement, a Hilbert filter is used in the backprojection algorithm. It comprises an integration step such that the reconstructed data is not differential any more but proportional to the refractive index decrement. Eq. 4.9 relates the refractive index decrement with the electron density which is an energy independent material quantity.

Within the experiments described here, the reconstructed dark-field data sets have not been converted to quantitative values as it was not relevant for the diagnostic question in Sec. 4.5.4. Details on the reconstruction of the linear diffusion coefficient can for example be found in [Bech, 2009].

All tomographic measurements were conducted with the sample immersed into a plane parallel water-filled plastic container which is also in place for the reference measurement. By that, the spectral photon distribution in sample and reference scan are very similar and homogeneous such that spectral changes of the stepping curve and the related artifacts are minimized. Additionally, phase wrapping at the borders of the sample due to a strong refractive index decrement gradient can be avoided.

The measured attenuation coefficients at broad X-ray spectra are effective coefficients comprised of the contributions of all energies $\mu_{\text{eff}} = \int \mu(E) dE$. In clinical imaging, this effective attenuation image is transformed to the so called Hounsfield unit (HU) scale by the following relation

$$\frac{\mu - \mu_{\text{water}}}{\mu_{\text{water}} - \mu_{\text{air}}} \times 1000 \text{ HU}, \quad (4.3)$$

where μ_{water} and μ_{air} are the attenuation coefficients of water and air. By that, the HU value for air is -1000 and the HU value for water is 0 by definition and thereby provides a two-point calibration of the measured values which allows comparison of the HU values between similar CT systems. If the shape of the used X-ray

spectrum is very different from a conventional clinical CT spectrum the HU values can still vary significantly for all materials except water and air. However, within the range of clinical applications, the HU scale provides a basis for comparison of findings between different CT examinations and is even used to quantify pathological changes [Schreiber et al., 2011, Gücük and Üyetürk, 2014, Dubey et al., 2001]. Analogously, the definition of phase Hounsfield units (HUp) based on the refractive index decrement δ is possible, as proposed by Donath et al. [Donath et al., 2010]

$$\frac{\delta - \delta_{\text{water}}}{\delta_{\text{water}} - \delta_{\text{air}}} \times 1000 \text{ HUp}. \quad (4.4)$$

Signal strength analysis

Signal to noise ratios (SNR) were calculated for the mean signal \bar{s} in a region of interest (ROI) inside the object compared to the mean of a ROI in the background \bar{b} and the standard deviation of this background region σ_b according to

$$\text{SNR} = \frac{|\bar{s} - \bar{b}|}{\sigma_b}. \quad (4.5)$$

The contrast to noise (CNR) value can be similarly calculated between two regions a and b as

$$\text{CNR} = \frac{|\bar{a} - \bar{b}|}{\sqrt{\sigma_a^2 - \sigma_b^2}}, \quad (4.6)$$

by taking the standard deviation σ_a and σ_b of both regions into account.

An SNR or CNR value below 1 means that an object cannot be distinguished from the background.

4.2 Foreign body detection

The main results of this chapter are published in Braig et al., Simultaneous wood and metal particle detection on dark-field radiography, in European Radiology Experimental [Braig et al., 2018a].

4.2.1 Clinical background

Open wound care is one of the most frequent tasks in emergency care and it is often related to the search and removal of retained foreign materials [Ebrahimi et al., 2013, Davis et al., 2015]. For patients with characteristic signs of retained material, physical examination is typically followed by a routine radiography [Turkcuer et al., 2006]. The majority of foreign bodies consist either of metal, glass, or wood [Levine et al., 2008, Lewis et al., 2015]. Especially wood, the most frequent foreign body material in the extremities, is reported to be missed in 85 – 95% of the patients in the initial radiographic examination because of its low attenuation contrast [Becton and Christian, 1977, Anderson et al., 1982, Bray et al., 1995, Turkcuer et al., 2006, Dunn et al., 2009, Ebrahimi et al., 2013, Lewis et al., 2015]. While X-ray radiography is highly sensitive for the detection of materials with high atomic number such as metals, weakly absorbing foreign bodies are easily missed in plain radiography. Even in computed tomography (CT), wood often cannot be distinguished from other hypodense materials like fat or air [Anderson et al., 1982, Bray et al., 1995, Dunn et al., 2009, Jusué-Torres et al., 2016].

In contrast, magnetic resonance imaging (MRI) exhibits good soft tissue contrast due to its sensitivity to differences in water content. However, routine foreign body detection in MRI is not feasible in an emergency department workflow due to the poor accessibility, low cost effectiveness and particularly the high risk, associated with the strong magnetic field, for patients with metallic material in their body [Schlager et al., 1991, Kudo and Takei, 2016]. Ultrasonography (US) shows good success in detecting retained soft-tissue materials in cases with a sufficient change of material impedance but is still highly dependent on the operator’s expertise, has the need for a specific transducer frequency and is a time consuming examination [Gilbert et al., 1990, Turkcuer et al., 2006].

However, the porous substructure of wood has previously been found to cause an X-ray dark-field signal in the context of food control [Nielsen et al., 2013, Einarsdóttir et al., 2016] (see Sec. 3.5). Therefore, X-ray dark-field radiography could be a suitable modality for improved clinical foreign body detection, as well. In the following proof of principle study, the simultaneous detection of metallic and wooden foreign bodies in preclinical grating-based radiography will be evaluated experimentally.

With a dedicated test phantom, the sensitivity of the method for wood and metal splinters of different sizes is systematically analysed and the attenuation and the dark-field signals are compared quantitatively. Additionally, the clinical scenario of retained foreign bodies in a human hand was experimentally simulated to assess the feasibility of the method in a realistic setting.

4.2.2 Experimental evaluation

This study is designed to evaluate the potential of X-ray dark-field radiography for improved foreign body detection. The study is divided into two main parts. First, the signal strength in dependence of the particle size is analyzed with a specifically designed test phantom with different configurations of tissue-like and bone-like absorbers as well as small metallic and wooden test particles. In the second part, the feasibility of simultaneous metal and wood particle detection in a human hand is evaluated in an ex-vivo experiment.

Materials and methods

Experimental settings The study has been performed at setup B (Sec. 4.1.2) with an acceleration voltage of 60 kVp at a tube power of 150 W. The sample was positioned behind the phase grating G1 which resulted in an effective pixel size of 110 μm due to the cone-beam magnification.

To achieve the necessary full field of view for the radiography of the hand, 3×3 single images were stitched together. The radiation exposure for the hand was 87.5 mAs distributed over 7 grating steps with 5 seconds of exposure per step. The test phantom fits into the field of view of a single projection. The exposure time for the test phantom was varied between 1, 2 and 5 seconds.

The incident air kerma was measured with a PTW NOMEX dosimeter (*PTW Freiburg GmbH*, Germany) at the position of the sample. Considering all gratings and the setup geometry, a measured air kerma of 0.22 mGy corresponds to an estimated image receptor dose of about 25 μGy for 1 second exposure time (please note, that the absorption of the G2 grating decreases this value compared to the actual dose applied to the sample).

Sample design and preparation The sensitivity and resolution of X-ray dark-field radiography foreign body detection is evaluated for very small particles with a specifically designed test phantom. It consists of a polymethyl-methacrylate (PMMA) plate (thickness 18 mm) and pairwise test objects of aluminum and wood with diameters of 0.5, 0.7, 0.9 and 1.1 mm fixed onto the plate with tape (configuration C1, see Fig. 4.3). The test objects are oriented in pairs horizontally and

vertically relative to the grating orientation. The PMMA plate is used to mimic the attenuation characteristics of soft tissue. In the second configuration, the above described test phantom is extended by an aluminum-oxide plate of 10 mm thickness (configuration C2), which mimics the additional attenuation of bone [Lehmann et al., 1981, Alvarez, 2011, Ehn et al., 2017a]. Images were acquired in both phantom configurations to assess the signal when detecting foreign bodies in soft tissue as well as directly behind a bone. Configuration C1 has been imaged with exposure times of 1 and 5 seconds per step. Configuration C2 has been imaged with 2 seconds per step.

For signal assessment within the human body, foreign body test objects were placed in the detached human hand of a deceased body donor. The study was approved by the local institutional review board. The donor of the hand had dedicated his body for educational and research purposes and provided written informed consent prior to death, in compliance with local institutional and legislative requirements. The hand was preserved with formaldehyde solution prior to the experiments. Three typical wooden and metallic foreign objects were inserted to the human hand to simulate the scenario of retained foreign bodies (Fig. 4.5B). The human hand was imaged with an exposure time of 5 seconds per step in a planar plastic container. The formalin filling level was reduced so that the beam path was free of fluid (Fig. 4.3).

Quantitative and qualitative signal analysis All radiographic images were acquired with the same technical parameters without specific image post-processing. The analysis of the images was divided into two parts. First, two trained radiologists (with both more than 10 years of experience) separately evaluated the images for the visual appearance of foreign bodies. Second, the signal strength was quantified by calculation of the SNR ratios.

For signal evaluation, the test features of the foreign body phantom are numbered consecutively from 1 – 4 from the smallest to the largest feature. The horizontal/vertical features are referred to as v/h, respectively.

Results

Visual evaluation of the foreign body phantom The conventional attenuation images are displayed in Fig. 4.4 above the corresponding dark-field image for the phantom configurations C1 and C2 and with different exposure times per phase-step. In the attenuation-based images, there is no systematic difference in signal strength between vertical and horizontal particles visible. In configuration C1 at 5 seconds exposure time per step (Fig. 4.4A), all wooden and aluminum test

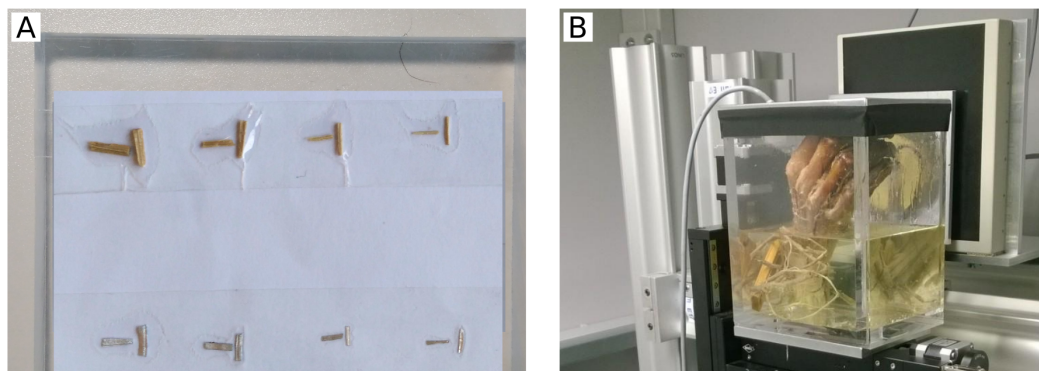


Figure 4.3: Test objects for evaluation of foreign body detection in X-ray dark-field radiography. (A) Pairwise test structures of aluminum and wood with diameters of 0.5, 0.7, 0.9 and 1.1 mm were fixed on a PMMA plate (thickness 18 mm) with tape in horizontal and vertical orientation in respect to the grating orientation (configuration C1). In configuration C2, an additional aluminum-oxide plate of 10 mm thickness was attached behind the PMMA plate to mimic not only soft tissue but also bone in the beam path. A piece of paper was added to increase the contrast in this photo and was removed for the experiments. (B) The detached human hand of a deceased body donor was placed into a planar plastic container to assess the feasibility of X-ray dark-field foreign body detection in-situ. The level of the formalin fixation solution was reduced such that the beam path was free of fluid. One metallic and two wooden foreign bodies were attached to the palmar region of the hand as test objects.

objects can be detected on the flat background in attenuation. At 1 second exposure time per step (Fig. 4.4B), only the larger wooden particles 3h/3v and 4h/4v and all aluminum features except feature 2v are detectable in attenuation. Behind the bone-like absorber (Fig. 4.4C) only the largest wood and aluminum particles 4h/v are slightly visible in attenuation.

Due to the directional sensitivity perpendicular to the orientation of the grating bars, there is a superior visibility of the vertical wood particles in the dark-field images. At 5 seconds exposure time all vertical wooden objects are clearly detectable in the dark-field image. The horizontal features 2h, 3h, 4h are slightly visible. At 1 second exposure time, all vertical wooden particles and the largest horizontal particle (4h) can still be identified. Behind the bone-like absorber, i.e. in configuration C2, all vertical wooden objects can be identified in the dark-field images. The metallic test object are not visible in the dark-field images in any configuration. Both radiologists provided the same results for visual inspection for all particles while the assessment was done independently. Thereby they confirmed the here described visual analysis of the author.

Quantitative signal evaluation in the foreign body phantom Results of the SNR analysis for all test objects are displayed in Tab. 4.1. The SNR values

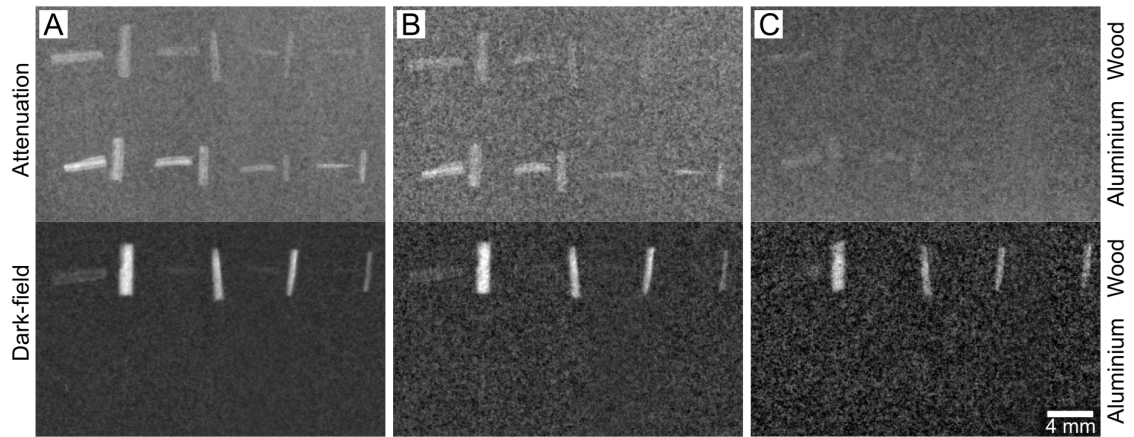


Figure 4.4: Phantom study for foreign body detection with X-ray dark-field radiography In all images the wooden test particles are in the upper row and the aluminum structures are in the bottom row. The conventional attenuation image is always displayed above the respective dark-field image. (A) In configuration C1 (test objects attached to 18 mm PMMA) with 5 seconds exposure time per step, all particles can be seen in the conventional attenuation image. In the respective dark-field images, all vertical wood splinters are clearly visible, the horizontal splinters are slightly visible, except for the smallest one (1h). (B) In configuration C1 with 1 second exposure time per step the metallic test particles are all visible in attenuation, except feature 2v. Also, the larger wood features 3h/3v and 4h/4v are visible. In the corresponding dark-field image, all vertical wood splinters and the largest horizontal wood splinter (4h) are visible. (C) In configuration C2 (i.e. with an additional aluminum plate) at 2 seconds exposure time per step only the largest wood and aluminum particles 4h/4v are visible in the attenuation image. In the dark-field image, all vertical wood features are clearly visible. The aluminum splinters are not visible in the dark-field radiographies in any configuration.

were calculated from the image data shown in Fig. 4.4. In the attenuation based image with 5 seconds exposure time per step, the SNR values range from 1.7 to 4.9. for the wooden particles and from 1.9 to 8.4 for the metallic particles. At 1s exposure time, the SNR ranges from <1 to 2.2 for the wooden particles and from <1 to 3.9 for the aluminum particles. The additional bone-like absorber in phantom configuration C2 decreases the SNR to <1 for all wooden particles. The larger aluminum particles 3h/3v and 4h/4v exhibit an SNR value between one and two (1.4 - 1.9).

In the dark-field images, the horizontal and vertical features exhibit a systematically different signal strength in accordance with the directional sensitivity of the interferometric method. In phantom configuration C1 at 5 seconds exposure time, the vertical wooden features show SNR values from 7.5 to 25.2, the horizontal ones range from 1.6 to 3.3. At 1 second exposure time, the SNR values range between 3.1 and 11.4 for the vertical wooden objects and only the largest horizontal wood particle, 4h, had an SNR above 1 (1.6). The aluminum particles exhibit SNR val-

ues smaller than one in the dark-field images for all configurations. In phantom configuration C2, the SNR values for the vertical wooden particles are in the range of 3.4 - 5.4. The SNR of the horizontal wooden particles are below one.

Direct comparison of the SNR values of the vertical wood splinters in dark-field radiography and conventional radiography showed an average signal increase of a factor of 6 in phantom configuration C1 and an increase from no signal to an average SNR of 4.1 for the features behind the bone-like absorber in configuration C2.

Attenuation		Wood			Aluminum		
Exposure (Config.)		5s (C1)	1s (C1)	2s (C2)	5s (C1)	1s (C1)	2s (C2)
horizontal	1h	1.7	1.1	<1.	4.9	2.7	<1.
	2h	2.6	<1.	<1.	3.2	1.5	<1.
	3h	2.5	1.6	<1.	6.5	3.1	1.4
	4h	4.9	2.0	<1.	8.2	3.7	1.4
vertical	1v	1.7	<1.	<1.	4.3	2.1	<1.
	2v	2.5	1.3	<1.	1.9	<1.	<1.
	3v	3.1	1.0	<1.	4.6	2.4	1.4
	4v	4.6	2.2	<1.	8.4	3.9	1.9
Dark-field		Wood			Aluminum		
Exposure (Config.)		5s (C1)	1s (C1)	2s (C2)	5s (C1)	1s (C1)	2s (C2)
horizontal	1h	1.6	<1.	<1.	<1.	<1.	<1.
	2h	1.9	<1.	<1.	<1.	<1.	<1.
	3h	1.6	<1.	<1.	<1.	<1.	<1.
	4h	3.3	1.6	<1.	<1.	<1.	<1.
vertical	1v	7.5	3.1	3.7	<1.	<1.	<1.
	2v	19.4	8.6	3.4	<1.	<1.	<1.
	3v	18.7	8.7	3.8	<1.	<1.	<1.
	4v	25.2	11.4	5.4	<1.	<1.	<1.

Table 4.1: SNR values for foreign body test objects in attenuation and dark-field radiography. The attenuation signal of the metallic particles is higher than that of the wooden splinters. Behind the bone like absorber (configuration C2), none of the wooden particles and only the larger metallic particles 3h/3v, 4h/4v can be differentiated from the background. There is no systematic difference between the signal strength of vertical and horizontal splinters. All vertical wood objects exhibit a strong dark-field signal in all configurations. The SNR values of the aluminum splinters in the dark-field images is below one for all particles in all configurations. The dark-field signal is generally higher for vertical objects due to the directional sensitivity of the grating interferometer.

Visual evaluation of foreign bodies in the human hand Fig. 4.5 shows the attenuation and dark-field radiographies of the human hand. In the conventional attenuation image (Fig. 4.5A), an elongated hyperdense object is apparent lateral of the diaphysis of the IVth metacarpal bone. This signal can be assigned to the

metallic saw blade that was placed at this position. The wooden particles cause no visible signal in the attenuation image. In dark-field radiography (Fig. 4.5B), the metallic object appears with a bright signal, as well. Additionally, an elongated bright region on the Vth metacarpal bone and another rectangular bright region in the inter-metacarpal space IV/V are visible and can be assigned to the wooden particles. The dark-field signal of wood directly behind the bone is still strong enough for a clear visual detection.

Discussion

In this study we demonstrated that grating-based radiography allows the simultaneous detection of wooden and metallic splinters in a specific test phantom as well as in a human hand. Systematic evaluation of pairwise test particles revealed that the dark-field signal of wood is even higher than the attenuation signal of aluminum splinters of the same size. As the novel dark-field image always comes with a conventional attenuation image, this method can be implemented into existing clinical routines.

With a phantom study, the high sensitivity even for very small wooden structures in the size range of a few detector pixels has been demonstrated. It has been found that the smallest wood particles are still detectable in the dark-field with clear SNR values, when the signal for the metal particles of the same size already disappears. Especially behind a bone-like absorber, even the smallest wood particle could be detected. As the dark-field signal is related to a local coherence decrease, an overlying, solely absorbing object in the beam path has less influence on the dark-field signal strength than on the attenuation signal strength.

The strong directional dependency of the dark-field signal entails the risk of missing retained materials. It is assumed that from the accident circumstances or visual inspection of the entry wound, the expected orientation of a foreign material can be derived in some cases. In general, it should be considered to acquire two radiographies from two orthogonal directions as usual for example in mammography or chest radiography. By that, the directional signal sensitivity can even help to localize the precise position and orientation of a wooden splinter. This additional knowledge can be used to support the planning of surgical removal and to assess the risk for related anatomical structures.

The experimental simulation of a traumatic foreign body scenario with a human hand has proven the feasibility of the method in a more realistic setting. It has been found, that the wooden materials are only visible in the dark-field channel. The metallic foreign body object was visible in the attenuation and the dark-field channel. Although the saw blade has no micro-structure that produces a dark-



Figure 4.5: Simultaneous wood and metal detection in a human hand with X-ray dark-field radiography. The metacarpal and phalangeal bones of the right hand are displayed in anterior-posterior projection. The fingers of the hand are in a slightly bent position due to the formalin fixation. Three foreign bodies (one metallic and two wooden particles, as displayed in the inlay at the upper right corner) were inserted into the palmar region of the hand to simulate the clinical case of retained foreign bodies. (A) In the conventional attenuation image, an elongated hyperdense object can clearly be identified close to the diaphysis of the IVth metacarpal bone (see magnified region below, marked with black arrows). There are no signs of further retained materials. (B) The metal object is visible in the dark-field image, as well. Additionally, two hyperdense regions are visible on the Vth metacarpal bone and the inter-metacarpal space IV/V, respectively (see magnified region below, marked with white arrows). These signals correspond to the two wooden particles. Comparison of the two images allows the identification and differentiation of porous low density materials and high atomic number or dense materials.

field signal, the high amount of absorbing material causes a spectral change of the stepping curve and thereby a dark-field signal. Thus, a profound knowledge of the underlying signal formation processes is necessary for accurate diagnosis. Comparative diagnosis of both image channels can then give information about the type, material and extension of the retained object. Therefore, this technique has the potential to characterize the quality of a foreign body in a single examination, which is likely to simplify the removal and the planning of an optimal management [Lammers, 1988, Halaas, 2007]. Foreign body detection often concerns the extremities of the body which reduces the requirements for a dark-field scanner in terms of X-ray energy, grating specifications and exposure time thanks to the isolated distal position of hands and feet and their moderate radiosensitivity. The technical feasibility of a clinically approved Talbot-Lau radiography machine has already been proven by the development of a prototype dedicated to depict cartilage in human fingers with a skin dose below 10 mGy (cf. 3.3). Together with the previously described potential diagnostic benefits from directional dark-field radiography for the analysis of the trabecular bone structure and results on the phase-contrast signal of cartilage for joint assessment, the here described foreign body detection can further extend the range of potential applications in the field of musculoskeletal imaging.

The presented experiments have been conducted at an experimental Talbot-Lau setup which is not optimized for clinical applications. Therefore, this study is focused on demonstrating the proof of principle of foreign-body detection with X-ray dark-field radiography. Especially the comparably low photon flux at the static anode tube and the limited field of view result in a high acquisition time with the chosen stitching approach. Compared to the applicable guidelines for radiographic imaging of a hand, the image receptor dose exceeds the value recommended in Germany by a factor of 2.5 for one second exposure time per step [Bundesamt für Strahlenschutz, 2007b] even though this value is decreased due to the G2 attenuation. A larger pixel size and the use of a state of the art clinical radiography detector as well as the optimization of the X-ray spectrum are potential steps to reduce the X-ray dose. As the used setup was only available with the described components the phantom study was designed to demonstrate the strong dark-field signal of wood in direct comparison to the attenuation signal of aluminum as a standard of reference. At photon-statistics where the smallest aluminum particle in the conventional image is not differentiable from the background, the clear visibility of a wood splinter of the same size in the dark-field image proves the potential of the method.

4.2.3 Conclusion

In comparison to diagnostic applications of X-ray phase-contrast imaging that require high phase-sensitivity or technically challenging setup configurations, the feasibility of clinical in-vivo X-ray phase contrast imaging of the extremities has already been proven. The method has a particularly high potential to be included into clinical routine, promptly and thereby simplify the diagnostic workflow and increase the success of foreign body detection.

Considering the high incidence and the minor emergency character of foreign body detection in human hands and feet, the method has the potential to close a gap between insufficient visual inspection and elaborate three-dimensional imaging methods like CT and MRI.

4.3 Gout diagnosis

The main results of this chapter are published in Braig and Roiser et al., X-ray dark-field radiography: Potential for visualization of monosodium urate deposition, in Investigative Radiology [Braig et al., 2020b]. This study was realized as an interdisciplinary collaboration between medical doctors, veterinarians and physicists.

4.3.1 Clinical background

Gout is the most common form of inflammatory arthritis with studies suggesting a prevalence between 0.5 – 9.5% worldwide [Pascart and Lioté, 2018]. It is related to an elevated serum urate level above the solubility threshold (6.8mg/dl at a body pH of 7.4 and a temperature of 37°C) resulting in the painful deposition of monosodium urate (MSU) crystals within and around the joints [Loeb, 1972]. Besides the patient’s history and clinical presentation, the diagnosis is confirmed by the microscopic verification of MSU crystals in the synovial fluid [Neogi et al., 2015, Richette et al., 2020]. Although the pathologic mechanisms are well understood and good therapeutic options are available, gout is reported to be still frequently misdiagnosed, neglected or poorly managed [Doherty et al., 2012]. This discrepancy is often associated with the fact that joint fluid aspiration requires special expertise and is not available in all primary care units - where most patients with acute gout attacks are seen.

However, with an early identification of MSU crystals, urate lowering therapy and lifestyle modifications can prevent recurrent attacks and the related irreversible joint damage. While an experienced physician can verify the presence of MSU crystals by the so-called double contour sign in ultrasonography, sensitivity and reliability have been reported to depend strongly on the individual examiner [Christiansen et al., 2018]. Due to the low attenuation coefficient of MSU, conventional radiography can only visualize the irreversible joint damage of the chronic condition but not the crystals in an early curable state. Recently, dual-energy CT (DECT) has been added to the American College of Rheumatology (ACR)/European League Against Rheumatism (EULAR) 2015 gout classification criteria [Neogi et al., 2015]. While the method provides high sensitivity for gout with tophus formation and moderate sensitivity for non-tophaceous gout [Baer et al., 2016], it is not accessible for comprehensive routine diagnostics in primary care units.

Under the microscope, MSU crystals reveal a fine needle structure in the micron size range. As is now well known, such a structure can cause a dark-field signal. Thus, X-ray dark-field radiography could be a potential candidate to provide a non-invasive diagnostic option that is based on a single projection image. In

the following, the general feasibility for MSU crystal detection with grating-based radiography is evaluated with an in-vitro study and an ex-vivo gout model in mice.

4.3.2 Experimental evaluation

This study is designed as a first proof of principle for gout detection in X-ray dark-field radiography. Therefore it is divided into two main parts. First, the X-ray dark-field signal from pure MSU crystals in a buffer solution is quantified. In a second step, the signal strength and the diagnostic value of X-ray dark-field radiography is assessed with a reader study based on an ex-vivo mouse model. Thereby, the value of the combined availability of the conventional attenuation image together with the novel dark-field image is particularly investigated by successively presenting one or the other or both image channels to the readers in three separated rounds.

Materials and methods

Experimental settings and imaging parameters The measurements were conducted at setup C at an acceleration voltage of 50 kV and 1.2 W tube power. The Eiger 500k photon-counting detector was used in a 4×4 binning mode. Together with the geometric magnification this resulted in an effective pixel size of $(166 \times 166) \mu\text{m}^2$. For every image, 11 phase steps were conducted with an exposure time of 1 second per step.

In-vitro crystal study The signal from MSU crystals in X-ray dark-field radiography was evaluated with an in-vitro study. The crystals were manufactured in our labs according to previously published protocols [Perrin et al., 2011, Pouliot et al., 1998]. The process involves the dissolution of equimolar quantities of uric acid sodium salt and sodium hydroxide, subsequent filtering and incubation at 40°C during the crystal formation. MSU crystals grow in a needle shape with the length of single needles of approximately $50 \mu\text{m}$. After air drying, the crystals can be stored at room temperature. For a more detailed description of the method, please find the references at the begin of this paragraph.

10 mg MSU crystals were filled into a 1.5 ml reaction tube (Eppendorf, Germany) and resuspended in $100 \mu\text{l}$ 1x phosphate buffered saline (PBS) to avoid artificial signal from the unphysiological situation of dry crystals with surrounding air. The contrast to noise ratio (CNR) was measured in a region of interest (50×50 pixels) within the MSU crystal deposition in the obtained X-ray dark-field and attenuation image to quantify the signal strength stemming from the MSU crystals.

Ex-vivo animal study Seven hind legs of 13-14 week-old female mice (C57B6/N, Janvier Labs, Le Genest-Saint-Isle, France) were removed post mortem. The animals were euthanized with an injected anesthetic overdose of ketamine-xylazine. The study was approved by the government of Upper Bavaria, Germany and followed the 3Rs guiding principles. Legs were chosen based on similar size, muscular mass and the amount of skin left on the lateral thigh. The legs were fixated in 4% neutral-buffered formalin and stored at 4° C until usage.

The legs were attached on a rubber board for imaging in the horizontal beam path. MSU crystal deposition was simulated by injecting 20–80 mg MSU crystals in 50 μ l 1x PBS subcutaneously with a 22 G cannula (*Braun*, Germany) into three of the seven legs. The injection was carefully placed close to the knee joint above the musculus biceps femoris. All legs were imaged before crystal injection and three legs were additionally imaged after crystal injection such that three positive (with MSU crystal deposition) and four negative (without MSU crystal deposition) samples were available for a reader study.

Additional to qualitative evaluation of the imaging results, three trained radiologists (2, 3 and 6 years of experience) diagnosed the images in a blinded reader study. The readers had received a short introduction to X-ray dark-field imaging by demonstrating two test images which were not included into the image set of the reader study. The evaluation was divided into three individual reading sessions separated by a time delay and with randomized image order to avoid recall bias. First, the attenuation images, then the dark-field images and in the last round both images together were presented to the readers for diagnosis. By that, the sensitivity and specificity of each image channel and of the combined information of both images should be evaluated. The readers were asked about the occurrence of MSU crystals and to grade their diagnostic confidence on a four point scale (0 not confident, 1 moderately confident, 2 quite confident and 3 highly confident).

Results

In-vitro MSU crystal detection Fig. 4.6A shows the appearance of the manufactured MSU crystals under the microscope. The crystal structure, size and morphology is consistent with that of MSU crystals from joint fluid analysis of gout patients [Terkeltaub and Edwards, 2011] such that the manufactured MSU crystals are suitable to simulate crystal deposition in the mouse legs. In conventional attenuation radiography (Fig. 4.6B), the MSU crystals in PBS solution appear as a homogeneous solution with intermediate X-ray attenuation and a clear contrast to the surrounding air. In dark-field radiography (Fig. 4.6C), the crystal sediment at the bottom of the reaction tube provides a strong signal and can be clearly dif-

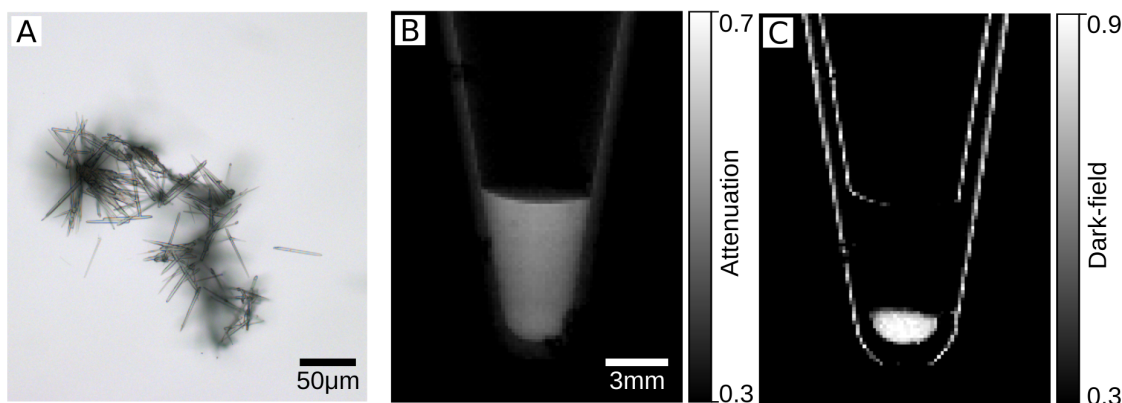


Figure 4.6: MSU crystals in microscopy and grating-based radiography. (A) The MSU crystals reveal a needle-like structure under the microscope. Individual needles have a length of approximately $50\ \mu\text{m}$. (B) Conventional attenuation radiography of $10\ \text{mg}$ MSU crystals in a physiological buffer solution (PBS) shows no visible contrast between the two components. (C) In dark-field radiography, the sedimented MSU crystals can clearly be separated from the PBS solution. The fluid-air interface can slightly be seen as a subtle line without further contrast between fluid and air.

ferentiated from the supernatant fluid. The dark-field signal arises also at sharp edges like the fluid-air interface and the margins of the reaction tube. The contrast between the crystal sediment and the fluid are $\text{CNR}_{\text{atc}} = 0.8$ in attenuation and $\text{CNR}_{\text{dfc}} = 19.3$ in the dark-field image. This corresponds to a relative contrast increase by a factor of 24.

Ex-vivo MSU crystal detection in mice Fig. 4.7 shows the radiographic images of the crystal injection experiment. Images acquired before crystal injection are displayed above the images after injection. Comparison of the attenuation radiographies before and after injection doesn't exhibit any systematic change. The visible roundish dark spots can be assigned to static grating imperfections that could not be eliminated, supposedly due to the spectral change between the flat-field and the sample image.

Comparison of the dark-field radiographies before and after injection, reveals a diffuse region of signal enhancement in all images after the MSU injection (marked by the blue circles). Case A: The signal enhancement is strongest within the cavity of the knee joint extending into the soft-tissue of the popliteal cavity. Case B: The enhanced signal overlays the entire knee joint with elongated fringed extensions towards the popliteal region and the lower leg. Case C: An oval signal enhancement stands out in the regio genus posterior with a blurred extended margin.

Direct comparison of the regions with dark-field signal enhancement with the respective regions in the attenuation images does not reveal any correlating signal in

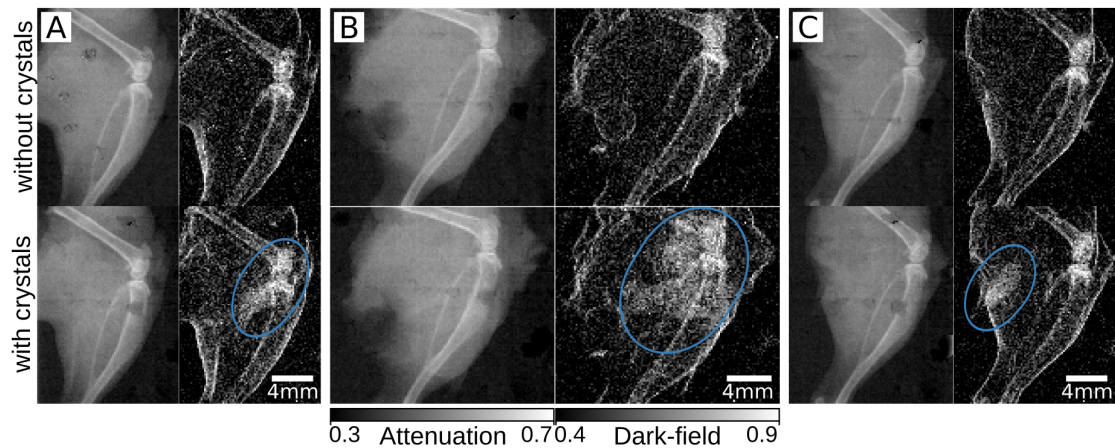


Figure 4.7: Ex-vivo MSU crystal detection with dark-field radiography. X-ray attenuation (left column) and dark-field images (right column) of 3 mouse legs before (top row) and after MSU crystal injection (bottom row). Crystals were injected into the popliteal region close to the knee joint (blue circles) to reflect the pathophysiological situation of gout deposition.

the conventional image. Due to the systematic occurrence of the signal only after crystal injection and together with the prior knowledge about the signal from the in-vitro experiment, this can unambiguously be identified as the signal caused by the MSU crystals.

Fig. 4.8 shows the confidence ratings within the reader study. Based on the attenuation images, the readers correctly identified the presence of MSU crystals with a sensitivity of 11%. The absence of MSU crystals was correctly diagnosed with a specificity of 92%. The readers stated that they are not confident about their diagnosis in 81% of the cases.

In the reading sessions with the dark-field images, all readers correctly identified all cases with MSU crystal deposition, resulting in a sensitivity of 100%. The specificity remained at 92%. The overall diagnostic confidence level increased to quite confident in 24% of the cases and highly confident in 71% of the cases.

The combined availability of attenuation images and dark-field images together in the last reading session resulted in correct diagnosis for all images with sensitivity and specificity of 100%. In this situation, all readers were confident about all diagnoses (19% graded as quite confident, 81% graded as highly confident).

Discussion

With the described experiments, the possibility of MSU crystal detection in X-ray dark-field radiography has been evaluated. The evaluation was subdivided into two main parts. First, an in-vitro experiment with MSU crystals demonstrated a quan-

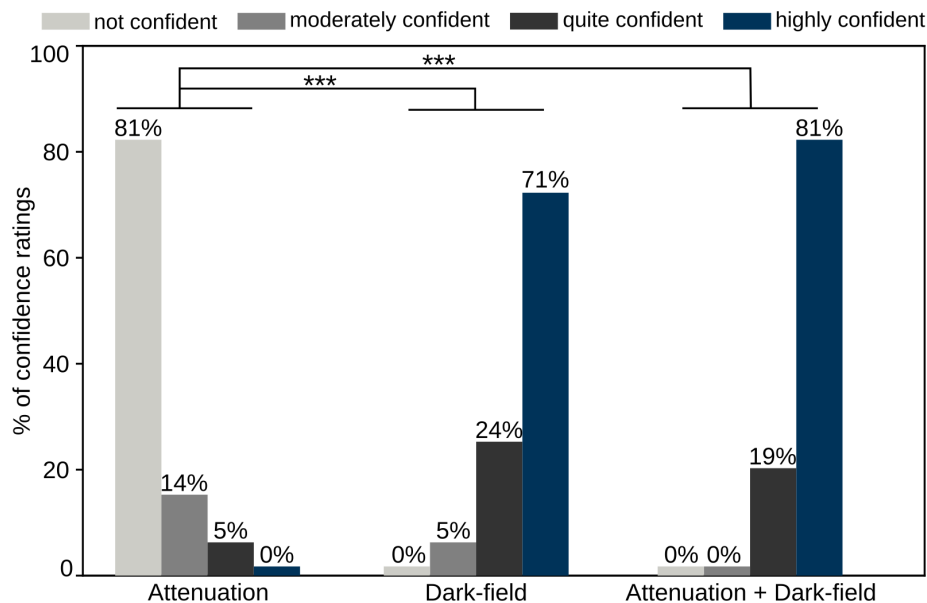


Figure 4.8: Confidence ratings for the three viewing sessions of the reader study. The attenuation images, the dark-field images, and both images together have been examined by three experienced radiologists in three reading rounds which were separated by a time delay. Every image was examined for the occurrence of crystal deposition and every diagnosis was assigned with a confidence level by the reader. Distribution of confidence ratings between the three viewing sessions are displayed in bar charts. Significance (***) $P \leq 0.001$.

titative signal increase from no signal in conventional attenuation to a strong signal in dark-field radiography. A subsequent ex-vivo mouse study demonstrated the possibility to detect MSU crystals in mouse legs. With a reader study, the quantitative and qualitative improvement of diagnostic accuracy and reliability have been assessed. While the conventional attenuation images alone provided insufficient information for MSU crystal detection, the dark-field images allowed for the identification of all cases with crystal deposition. The comparative diagnosis of both image channels at the same time, revealed the best diagnostic success and a high confidence rating.

Within the last years, the ability of X-ray dark-field imaging for the detection or differentiation of microcalcifications and crystals has been investigated for different pathologies. In particular, the ratio between attenuation and dark-field signal strength has been found to allow the differentiation of compact and granular breast microcalcifications [Scherer et al., 2017] or to differentiate several types of kidney stones [Scherer et al., 2015a].

In the context of gout diagnosis, it should be evaluated in future studies if the differentiation of mono sodium urate crystals and calcium pyrophosphate dihydrate crystals is possible with the same technique to ensure reliable differential diagnosis

regarding pseudo-gout. It can be expected that the comparison of the two signals allows the identification of calcium pyrophosphate dihydrate deposition which is - other than MSU deposition - often visible in attenuation radiography. Thus, the ratio of dark-field to attenuation signal is expected to be different for these two materials.

A remaining open question concerns the lower concentration limit for the crystal detection. Especially, the purpose of detecting early, curable states of the disease might profit from a high sensitivity for low crystal concentrations. As the literature is not clear about the quantitative threshold of MSU crystals within primary gout attacks, the lower detectable limit in X-ray dark-field radiography should be evaluated in a follow-up study and the sensitivity to different states of gout should be evaluated with an in-situ study.

4.3.3 Conclusion

While many potential applications of X-ray phase-contrast and dark-field imaging for simplified or improved diagnostics have been demonstrated in the lab in the last decade, some of them require technical improvements in terms of grating fabrication, interferometer geometry or algorithmic signal extraction. Compared to other applications like phase-contrast mammography with very strong dose requirements or phase-contrast CT which is both challenging in terms of technical realization and concerning the physical limitations of the sensitivity towards higher energies and shorter propagation distances, X-ray dark-field radiography of the hands and feet relaxes the technical as well as the dose requirements. In fact, the technical realization of a clinical X-ray phase-contrast scanner approved for imaging human joints in the hand, the feet and the knee has been demonstrated a few years ago [Momose et al., 2014a, Yoshioka et al., 2020] as already mentioned in the last section (Sec. 4.2). By that, the early detection of gout crystal deposition is another promising candidate to extend the range of applications of grating-based musculoskeletal imaging.

X-ray dark-field radiography is a non-invasive method that relies on a single X-ray projection. This prevents the risk of infection from sometimes painful joint fluid aspiration, potentially increases the comparability between different investigators compared to ultrasound and might be more accessible than CT, DECT or MRI. Therefore, this method is particularly promising for identifying the first occurrence of MSU deposition in a primary care unit and for monitoring the progress of the disease in regular check-ups. The results of this first proof of concept engage the further investigation of the method and its advancement for clinical application to make the benefits accessible for the concerned patients.

4.4 Dark-field contrast agents

The availability of novel X-ray imaging modalities brings the possibility of the introduction of novel contrast agents. For X-ray dark-field imaging, microbubbles have been proposed as a contrast agent shortly after the introduction of the technique. Iodine based contrast agents are an inevitable tool in clinical imaging but are related to adverse effects, especially for patients with renal dysfunctions. The development of microbubble-based dark-field contrast agents would therefore open up a huge market for grating-based imaging. However, the concept has not yet reached a state that would allow preclinical testing. Here, the current state is evaluated and a broad overview over the clinical background and previous projects is given. Additionally, commercially available microbubble-based ultra sound contrast agents and PLGA spheres are evaluated experimentally for their X-ray dark-field signal strength.

4.4.1 Clinical background

Among all potential clinical applications of grating-based X-ray imaging, the successful demonstration of a novel contrast agent might have the biggest impact. According to the world health organization, cardiovascular diseases (CVD) are the number one cause of death worldwide. CVD summarize a group of disorders concerning the heart and blood vessels, including stroke, heart attack, peripheral artery disease and deep vein thrombosis as well as pulmonary embolism [WHO CVD, 2020]. The low soft tissue contrast of the involved body parts often requires the use of iodinated contrast media. Iodinated contrast media are among the most frequently administered intravascular pharmaceuticals with almost 75 million doses worldwide per year [Pasternak and Williamson, 2012] and about 1.7 million contrast enhanced CT investigations in Germany in 2009 [Grobe et al., 2011]. The combination of the broad accessibility, fast image acquisition and the high detail contrast in iodine enhanced CT makes it an indispensable tool in emergency care, diagnostic and interventional imaging as well as in aftercare. However, iodine based contrast agents can cause severe allergic reactions that require subsequent emergency care involving airway, breathing and circulation management. The incidence of adverse reactions like nausea, rush or pain on injection is with 3 – 15 % quite frequent while severe reactions can occur in 0.04 – 0.2 % of the cases. Iodine contrast agents are excreted via the kidney and are additionally related to a risk for contrast agent induced nephropathy or even renal failure. The risk is below 5 % for patients with normal renal function but can be up to 50 % for patients with preexisting renal dysfunctions [Pasternak and Williamson, 2012, Paefgen et al., 2015]. Especially these patients

could profit from the development of a novel type of contrast agent that eliminates the need for high atomic number contrast media.

Arfelli et al. first reported on the scattering signal enhancement by the use of ultrasound contrast agents [Arfelli et al., 2010]. Ultrasound contrast agents are based on gas-filled microspheres that change the acoustic properties in the respective tissue. These contrast agents are cleared via the lungs and the reticuloendothelial system [Hutter et al., 1999, Yanagisawa et al., 2007] and don't carry a risk for renal failure. Therefore, the concept of X-ray dark-field contrast enhancement by different kinds of microspheres has frequently been examined within the scientific community. However, the quantitative description of the dark-field signal is a complex task and the experimental handling of microspheres contains some difficulties.

In this section, the topic of X-ray dark-field contrast agents will be discussed in detail by reviewing previous studies, by an estimation of the required characteristics of the microbubbles for clinical applications and by presenting experimental results on currently available ultrasound contrast agents.

Ultrasound contrast agents Ultrasound contrast agents are based on gas filled microspheres that change the acoustic properties in the respective tissue. While first experiments with agitated saline solutions for ultrasound contrast enhancement date back to the late 1960s, the first FDA approved ultrasound contrast agent Albunex (*Molecular Biosystems Inc.*, San Diego, California), consisting of air filled albumin spheres, wasn't commercially available until 1990 [Paefgen et al., 2015]. Due to the high solubility of air in blood, the stability was poor and therefore the circulation time of the air filled bubbles was quite short. By replacing air with a gas with low blood solubility, the stability was increased to a lifetime of several minutes [Paefgen et al., 2015].

Depending on the realization of the shell, the spheres provide longer circulation time in-vivo, better resistance to higher ultrasound intensities or optimized oscillation properties. One can distinguish hard-shell microbubbles, which are mainly made of polymers, porous silica materials or denaturated proteins and soft-shell microbubbles, which are mostly made of phospholipids or surfactant molecules. While hard-shell microbubbles provide longer circulation times and burst at a specific transducer frequency, the soft-shell materials are held together by hydrophobic interactions and will therefore form smaller bubbles, when they are destroyed. This leads to non-linear oscillation properties which increases the ultrasonic detection sensitivity [Paefgen et al., 2015, Sirsi and Borden, 2009].

Tab. 4.2 shows an overview of the commercially available ultrasound contrast agents. First generation ultrasound contrast agents consisted of microspheres filled with air. Most of the new generation products are based on phospholipids as shell material,

Name	Concentration	Sphere diameter	Shell material	Gas	Producer	Market
Optison	$(5 - 8) \cdot 10^8/\text{ml}$	$2.5 - 4.5 \mu\text{m}$	Cross-linked serum albumin	Octafluoro propane	GE	US, Europe
Sono Vue/ Lumason	$(1.5 - 5.6) \cdot 10^8/\text{ml}$	$1.5 - 2.5 \mu\text{m}$	Phospho lipid	Sulphurhexa fluoride	Bracco diagnostics	US, Europe, China
Lumivity/ Definity	$6.4 \cdot 10^9/\text{ml}$	$1.1 - 2.5 \mu\text{m}$	Phospho lipid	Octafluoro propane	Lantheus medical imaging	North America, Europe
Sonazoid	$1.2 \cdot 10^9/\text{ml}$	$2.4 - 3.5 \mu\text{m}$	Phospho lipid	Perfluoro butane	GE	Japan, South Korea
Imagent/ Imavist	$10^9/\text{ml}$	$5 - 6 \mu\text{m}$	Phospho lipid	Perfluoro hexane nitrogen	Schering AG	US
Echovist	<i>unknown</i>	<i>unknown</i>	Galactose microparticles	Air	Schering AG	Germany, UK
Levovist	<i>unknown</i>	$2 - 3 \mu\text{m}$	Galactose microparticles, palmitic acid	Air	Schering AG	Canada, Europe, China, Japan
Albunex	<i>unknown</i>	<i>unknown</i>	Sonicated serum albumin	Air	Molecular Biosystems Inc.	Japan

Table 4.2: Commercial ultrasound contrast agents. Ultrasound contrast agents are based on suspensions of microspheres that increase the echo signal in the respective tissue. In newer generations, perfluorocarbon replaced air as a filling gas to increase the stability and the lifetime within the vessel system. Availability and product names vary for different regions. The gray font color indicates previous generations, that are not available on the market anymore.

one of them is based on human albumin, which is a blood protein involved into the maintenance of the oncotic pressure within the vessel system. For the product Vevo MicroMarker used in [Velroyen et al., 2013], no further information was found. It seems not to be available on the market anymore.

Contrast enhanced ultra sound is established in echocardiography [Cosgrove, 2006] and for abdominal imaging, especially for liver, spleen and kidneys [Quaia, 2007]. While the Doppler signal is only able to visualize bigger vessels, microbubble contrast agents allow the visualization of both micro- and macro vascularization. Additionally, these contrast agents are used within the urinary tract and the female reproductive organs [Cosgrove, 2006].

Pharmacokinetics of ultrasound contrast agents With a bubble size of $1 - 10 \mu\text{m}$, ultrasound contrast agents are limited to the intravascular system and

can not extravasate into surrounding tissue like iodine based contrast agents. Thus, accumulation in the interstitial space is inhibited and therefore unwanted background signal is prevented [Paefgen et al., 2015].

Perfluorocarbon gas is biologically inert and is completely exhaled within one day without any modification [Hutter et al., 1999]. The shell materials are cleared via the reticuloendothelial system by phagocytosis [Paefgen et al., 2015]. Renal clearance has not been reported for the clinically approved ultrasound contrast agents. Therefore, they are a true alternative for patients with renal insufficiency. Different clearance behaviour of shells made of similar materials are most likely due to slightly different surface structures which are triggering the complement system in a different way. By adding polyethylen glycol to the outer surface, the circulation time before reticuloendothelial clearance can be prolonged [Yanagisawa et al., 2007].

Review of previous studies on X-ray dark-field contrast agents Arfelli et al. proposed in 2002 the use of scattering material for contrast enhancement in diffraction enhanced imaging [Arfelli et al., 2002, 2003] and recognized that ultrasound contrast agents are based on such a scattering material. They found a strong scattering contrast enhancement by the ultrasound contrast agents Levovist (*Schering AG*, Berlin, Germany) and Optison (*GE*, Boston, Massachusetts) but recommended to do further experiments at conventional sources rather than at the synchrotron to enable a potential clinical implementation [Arfelli et al., 2010]. However, further studies investigated the potential of micro-spheres for different synchrotron based phase-contrast imaging techniques, mostly for biomedical small-animal or in-vitro applications [Tang et al., 2011, Tang and Yang, 2013, Xi et al., 2011]. Wu et al. demonstrated the potential of microbubbles as a contrast agent for high-energy in-line phase-contrast imaging [Wu et al., 2017].

With the first demonstration of X-ray dark-field contrast enhancement at a Talbot-Lau interferometer an important step towards potential clinical use was made [Velroyen et al., 2013]. Velroyen et al. used three different commercial ultrasound contrast agents and found that while Optison provides clear contrast enhancement, Sono Vue and Vevo MicroMarker (both *Bracco Imaging*, Milan, Italy) had the same low dark-field signal as water. As sphere size and bubble concentration of these different media are in the same magnitude, the origin of the different signal was not clear at this point. However, they could demonstrate, that the signal enhancement by Optison is increased when increasing the pixel size to clinical detector pixel sizes (about 1 mm) [Velroyen et al., 2013]. Further studies evaluated the quantitative description of the contrast agent concentration under physiological flow conditions by simulation and analyzer based synchrotron experiments [Millard et al., 2013, 2015].

Other simulations and experimental studies of monochromatic sources derived a quantitative description of the dark-field signal from micro-sphere suspensions in dependence on the interferometer geometry and the properties of the microspheres [Lynch et al., 2011, Malecki et al., 2012]. Gkoumas et al. extended the analytical and experimental quantitative interpretation of the dark-field contrast for micro-sphere suspensions with volume fractions above 40 % with measurements of SiO₂ microspheres at the synchrotron. Further, it has been demonstrated that the size and short-range order of scattering structures can be determined in a quantitative manner at conventional X-ray sources via the position dependent interferometer sensitivity [Prade et al., 2016]. Zhang et al. experimentally investigated the dependence of the dark-field signal on sphere properties like the diameter, shell thickness and shell coating as described below [Zhang et al., 2016].

Velroyen et al. further explored the potential of microspheres for X-ray dark-field contrast enhancement with Talbot-Lau interferometers for small animals [Velroyen et al., 2015]. They demonstrated an experimental X-ray dark-field angiography with an ex-vivo mouse and iron oxide coated polyvinyl alcohol (PVA) microspheres. The experiment proved the feasibility of microbubble based contrast enhancement in presence of scattering and attenuating mouse body structures like bone and fur within a dedicated small-animal dark-field scanner. In a subsequent study they found out that the iron oxide coating had no influence on the dark-field signal but caused a slight attenuation signal [Velroyen, 2015].

Dark-field signal from microspheres Various studies have investigated the quantitative description of the X-ray dark-field signal and its dependence on the structure size of microsphere suspensions. In the following, some of the main findings are summarized as a basis for future contrast-agent design. Tab. 4.3 gives an overview over some of the microspheres used in the experimental studies.

Yashiro et al. formulated the visibility reduction by the autocorrelation function of spatial fluctuations of the wavefront due to unresolved micro structures [Yashiro et al., 2010]. With this description they could successfully explain their experimental results for microspheres and a melamine sponge within synchrotron measurements.

Bech et al. demonstrated experimentally that the dark-field signal decays exponentially with the sample thickness similar to the Beer-Lambert law. They introduced a linear diffusion coefficient, which is an interferometer independent material quantity in analogy to the linear attenuation coefficient [Bech et al., 2010].

Lynch et al. extended the work of Yashiro et al. for grating-before-sample configuration where the plane wave assumption no longer holds [Lynch et al., 2011]. They

derived a quantitative expression for the linear diffusion coefficient μ_{df} for a suspension of microspheres and thereby explained the particle size selectivity of the signal. With the sample-detector distance L , the fringe period p and the X-ray wavelength λ , the autocorrelation distance is $\zeta = \lambda L/p$ and the linear diffusion coefficient is

$$\mu_{\text{df}} = \frac{3\pi^2}{\lambda^2} v_f |\Delta\chi|^2 \zeta \cdot f(d/\zeta). \quad (4.7)$$

Thus, the dark-field signal of a microsphere suspension is dependent on the sphere diameter d , the refractive index difference of the sphere material and surrounding fluid $\Delta\chi$, the volume fraction of the microspheres v_f and a function of the ratio of sphere diameter to correlation length $f(d/\zeta)$. f is sectionwise defined such that the dark-field extinction coefficient decreases linearly with decreasing sphere diameter if the sphere diameter is smaller than the autocorrelation length. If the sphere diameter exceeds the setup's autocorrelation length $d > \zeta$, f is a more complex function. Based on this function they could experimentally validate that the visibility reduction has a maximum if the sphere diameter equals approximately 1.8 times the interferometer's correlation length.

This is in agreement with further studies on the dark-field signal of microsphere suspensions. Malecki et al. investigated the signal strength as a function of the sphere diameter with wave optical simulations. They found a maximum signal for sphere diameters of $4.5 \mu\text{m}$ when keeping the total volume fraction occupied by the spheres constant, i.e. the number of bubbles increases with decreasing sphere diameter [Malecki et al., 2012]. From the given interferometer parameters the correlation length of the setup can be estimated as $\zeta_{\text{Malecki}} \geq 2.5 \mu\text{m}$. The reported maximum signal for sphere diameters of $4.5 \mu\text{m}$ is therefore in accordance with the findings of Lynch et al.

Within their study on the dark-field signal of ultrasound contrast agents Velroyen et al. [Velroyen et al., 2013] used the same simulation framework as Malecki et al. to find the optimum sphere size for the used Talbot-Lau interferometer. Accordingly, the maximum dark-field signal was expected for a sphere size between $2 - 3 \mu\text{m}$ which corresponds to 1.8 times the correlation length of the described setup ($\zeta_{\text{Velroyen}} = 1.29 \mu\text{m}$).

Zhang et al. [Zhang et al., 2016] experimentally investigated the quantitative relationship between the dark-field signal strength and different parameters of a microsphere suspension at a Talbot-Lau setup. They found that the dark-field signal increases linearly with the sphere concentration, that a moderately increased shell thickness might cause a stronger signal and that the attachment of gold nanoparticles enhanced the signal.

Publication by	Name	Sphere diameter	Type	Producer
Arfelli et al. [2002]	-	$\leq 100 \mu\text{m}$	hollow silica microsphere powder	-
Lynch et al. [2011]	-	$0.2 - 1.5 \mu\text{m}$	random suspension of silica microspheres	-
Lynch et al. [2011]	-	$0.1 - 0.2 \mu\text{m}$	iron oxide nanoparticle suspension (water-based acrylic black paint)	-
Millard et al. [2015]	Expancel	$8 \mu\text{m}$	polymer shell microbubbles	AkzoNobel
Velroyen et al. [2015]	DMM150	$5.5 \mu\text{m}$	magnetically coated PVA microbubbles	Surflay Nanotec GmbH
Prade et al. [2016]	-	$0.5 - 7.4 \mu\text{m}$	SiO ₂ microspheres	microParticles gmbh
Gkoumas et al. [2016]	-	$1.9 - 10 \mu\text{m}$	monodisperse SiO ₂ microspheres	Corpuscular Inc./ Sospheric LLC
Zhang et al. [2016]	-	$2.6 - 4.5 \mu\text{m}$	N ₂ gas encapsulated hollow polymer protein double layer microcapsule	self-made
Wu et al. [2017]	Expancel 461 DU 20	$6 - 9 \mu\text{m}$	copolymer shell microspheres	AkzoNobel

Table 4.3: Microspheres used for X-ray dark-field imaging. Different experimental studies investigated the signal strength from microspheres. For a few exemplary studies name, sphere diameter, type and producer are listed here as they were given in the respective publication.

4.4.2 Experimental evaluation

Three different ultrasound contrast agents were commercially available in Germany at the time of the measurements. These three contrast agents were tested at different Talbot-Lau setups to evaluate their general dark-field signal strength and the stability of the microspheres under in-vitro conditions.

Materials and methods

Experimental settings and image acquisition Setup C was used for the first signal assessment at high sensitivity. It was operated at 40 kV acceleration voltage and 2.8 kW tube power. Phase stepping was in general performed with 11 phase steps with 1 s exposure per step if not stated otherwise in the respective image description. Depending on the sample position in the cone-beam the effective pixel size was $p_{\text{eff}} = 83 - 98 \mu\text{m}$.

Setup D was used to estimate the performance at a preclinical full field setup. The tube was operated at 60 – 70 kV acceleration voltage with 10.5 – 12 kW tube power. The total exposure time for one full field scan was 0.55 s. The effective pixel size at the position of the sample was $p_{\text{eff}} = 375 - 404 \mu\text{m}$.

Optison Optison is an injection dispersion which is mainly used for ultrasonic contrast enhancement in echocardiography. It consists of heat-treated human albumin microspheres with diameters of 2.5 – 4.5 μm . The spheres are filled with octafluoropropane gas (perflutren) [Drugbank, 2020]. The recommended dose per patient is 0.5 – 3.0 ml and should not exceed 8.7 ml. With a declared mean concentration of $(5 - 8) \times 10^8$ microspheres per ml, this yields a maximum number of 7×10^9 microspheres per patient. The perflutren is eliminated via the lung with a half-life of approximately 1.3 min. Optison in the non-resuspended state consists of a separate layer of microspheres on top of the liquid phase. Before usage, the microspheres have to be resuspended by gently rolling the glass vial between the palms for three minutes or until full resuspension. If fully resuspended, the suspension appears as a homogeneous white opaque fluid. Pressure fluctuations can destroy the delicate spheres. Therefore, the vial must be ventilated before carefully withdrawing the fluid into a syringe via a needle not smaller than 20 G (Gauge: inverse measure for the diameter of injection cannulae, see EN ISO 6009 and EN ISO 9626) [EMA, 2008].

Luminity Luminity is an injection dispersion for ultrasonic contrast enhancement in echocardiography, consisting of perflutren filled phospholipid microspheres



Figure 4.9: Photograph of mixing device Vialmix for preparation of Luminity contrast agent. Before administration, Luminity contrast agent must be activated with the mechanical shaking device. The vial is clamped into the carrier and then agitated at high frequency for 45 s.

with 1.1 – 2.5 μm diameter. The recommended maximum total dose of 1.6 ml contains $\approx 1 \times 10^{10}$ microspheres (mean concentration: 6.4×10^9 microspheres per ml). The perflutren component of Luminity is rapidly cleared via the lungs with a half-life of approximately 1.3 min. In the non-resuspended state, Luminity is a colorless, uniformly clear liquid. Before administration, it must be activated with the mechanical shaking device Vialmix (*Lantheus Medical Imaging*, N. Billerica, Massachusetts) (see Fig. 4.9). After activation, the solution should be used within 12 h and can be reactivated within 48 h. If not used directly after activation, it must be resuspended by 10 s of hand agitation. To avoid pressure instabilities, the vial must be ventilated before withdrawing the fluid into a syringe via a needle no smaller than 20 G [EMA, 2009].

Sono Vue Sono Vue is a lyophilized powder in a sulphur hexafluoride atmosphere with 0.9% NaCl solvent for dispersion prior to injection. It is used to enhance the echogenicity of blood or fluids in the urinary tract. By adding the NaCl solution to the lyophilized powder and subsequent vigorous shaking, sulphur hexafluoride bubbles with a mean diameter of 1.5 – 2.5 μm are produced. The maximum recommended dose for intravenous use is 4.8 ml, containing up to 2.7×10^9 microbubbles (concentration: $(1.5 - 5.6) \times 10^8$ microbubbles per ml). Sono Vue should be administered immediately after preparation or must be resuspended by shaking it again within six hours. If resuspended, the liquid must be homogeneously white opaque without solid undissolved particles of the lyophilized powder [EMA, 2007].

PLGA spheres Polylactid-co-Glycolid (PLGA) spheres were produced in the lab according to the following procedure (similar as in [Raichur et al., 2014]). 52 mg PLGA is dissolved in 1 ml of ethyl acetate and 1 ml 5 % PVA solution is added drop by drop at 40° C. Then, 1 ml 5 % PVA solution is added drop by drop at 10° C and the solution is stirred for 5 minutes. The prepared solution is then added to 50 ml 0.05 % PVA solution. By stirring it with a magnetic stirrer at 200-600 rotations per minute for some hours the ethyl acetate is evaporated (Fig. 4.19A). The resulting microspheres can be washed and stored in the fridge. The size of the produced microspheres can be controlled via the stirring speed. In the end, the spheres were separated into three batches according to their diameter by changing the solvent density. Depending on the concentration of added sugar, the solvent density changes and a different sphere size group floats freely in the middle of the tube and can be withdrawn with a pipette. Heavier spheres settle at the bottom, lighter spheres swim at the top of the fluid level. The different batches were stored in separate plastic containers with 1 cm diameter.

Results

Light microscopy The three commercially available ultrasound contrast agents were investigated with an Axioskop 2 (*Zeiss*, Oberkochen, Germany) optical light microscope with hundredfold magnification. Fig. 4.10 shows the photographs through the ocular with an AxioCam MRc5 camera directly after placing a drop of the respective suspension on the microscope slide. Sono Vue shows the lowest number of microspheres within the field of view, the largest sphere diameters and the largest variation of sphere sizes. Optison and Luminity show more homogeneous sphere sizes and smaller sphere diameters. Luminity exhibits the smallest sphere sizes and the highest number of spheres in the field of view. Visual observation of the microspheres revealed an inferior stability of the Sono Vue spheres. Within several seconds, smaller bubbles merged to form bigger ones or burst. This behaviour can be observed for the other two contrast agents, as well, but much less frequently and in total on a larger time scale. As the dark-field signal scales with the concentration of microspheres, the instability and low concentration of the Sono Vue spheres are expected to cause an inferior dark-field signal.

Optison Fig. 4.11 illustrates the dependence of the signal strength on the contrast-agent concentration at setup C. From left to right the amount of contrast agent increases and the respective amount of NaCl decreases (Optison volume fraction: 0%, 10%, 20%, 60%, 80%, 100%). The plastic tubes were immersed into a plane

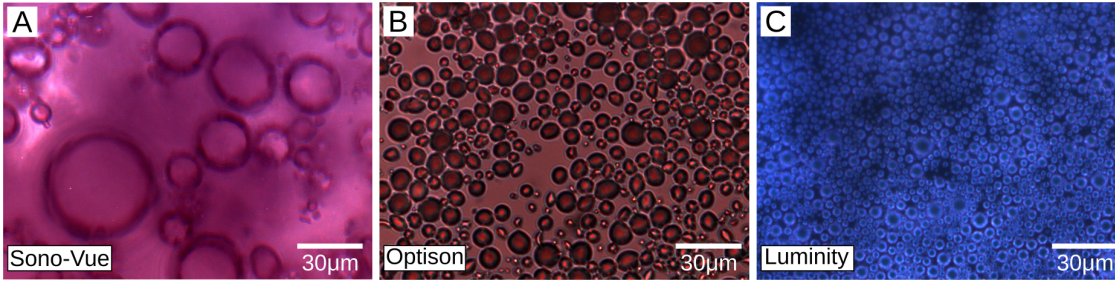


Figure 4.10: Light microscopy of three different ultrasound contrast agents. (A) Sono Vue microbubbles present with a broad size distribution and a small total number of spheres within the field of view. Visual observation showed that the Sono Vue bubbles merge or burst within several seconds, causing a fast decrease of the bubble concentration within the relevant size range. (B) Optison microspheres are smaller, the concentration is higher and the size distribution is narrower. (C) For Luminosity, the number of microspheres in the field of view is highest, the size distribution is narrow and the number of very small spheres is higher than for the other two contrast agents.

parallel water container of 0.5 cm diameter. In attenuation radiography, the contrast of the fluid filled plastic tubes to the surrounding water is very weak and the increasing concentrations of contrast agent can not be identified (contrast to pure NaCl: $CNR_{atc} = 1.0, 1.4, 1.6, 1.2, 0.4$). In dark-field radiography, the increasing concentration of Optison contrast agent correlates with an increasing signal strength. The contrast to pure NaCl increases with the contrast agent concentration ($CNR_{dfc} = 0.0, 2.7, 6.4, 9.9, 12.4$) as plotted in Fig. 4.11C.

Direct comparison of the contrast enhancement by iodine in attenuation radiography and Optison in dark-field radiography is demonstrated in Fig. 4.12. As a reference, an identical amount of NaCl was imaged together with the two contrast agents. 300 mg/ml iodine contrast agent cause a clear attenuation contrast compared to NaCl ($CNR_{atc} = 85.5$ in a region of 70×15 pixel). Optison presents with $CNR_{dfc} = 12.4$ compared to NaCl in dark-field radiography. The strong attenuation by iodine enhances the noise but also alters the stepping curve due to the spectral change. Thus, iodine presents with a dark-field signal with amplified noise. Within the NaCl filled syringe air bubbles of different size at the tube wall cause a slight dark-field signal.

In the large field-of-view scanner (setup D), the whole package content of Optison contrast agent was imaged simultaneously (Fig. 4.13) with grating configuration 1 (see Sec. 4.1.2). The images were acquired directly after resuspension within the original glass vial. The vial on the right of the field of view contains NaCl instead of contrast agent. In attenuation radiography as well as in dark-field radiography, a large bubble is visible at the highest point of each lying vial. While the NaCl solution presents with a homogeneous signal in attenuation, the contrast agent suspensions

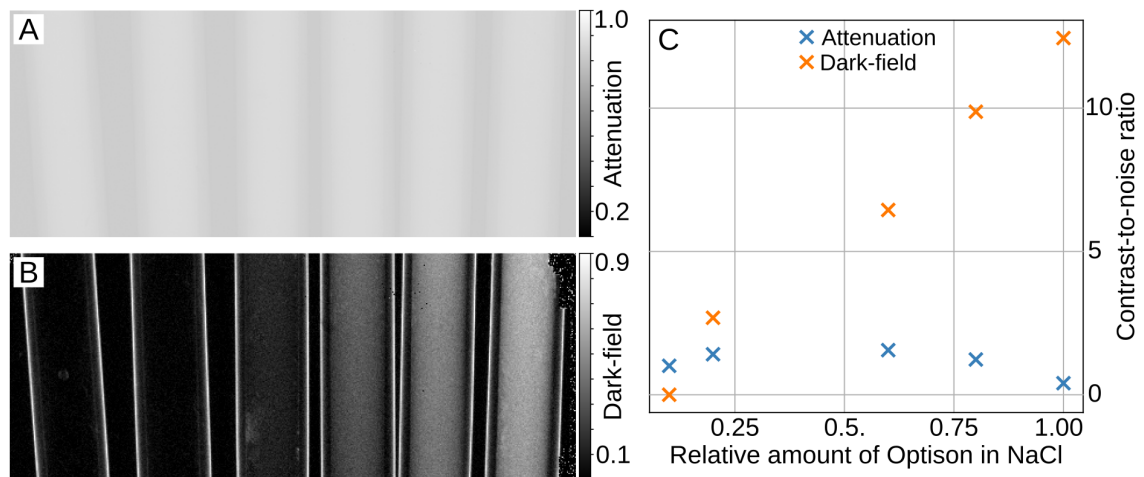


Figure 4.11: Signal strength of increasing Optison concentrations in dark-field radiography. Plastic tubes are filled with increasing concentrations of Optison ultrasound contrast agent and are immersed into a plane parallel water container. The tubes contain mixtures of NaCl and Optison with volume fractions of Optison of 0%, 10%, 20%, 60%, 80% and 100% from left to right. (A) In attenuation radiography the contrast of the tubes and their filling to the surrounding water is weak. The increasing contrast-agent concentrations can not be identified. (B) In dark-field radiography, the pure NaCl solution shows no contrast to the water in the background. With increasing Optison concentration, the dark-field signal increases. (C) CNR values of 70×15 pixel regions in the middle of the tubes between pure NaCl and the increasing Optison concentrations. The value fluctuates around a mean value of 1.12 in attenuation independent of the contrast agent concentration. In the dark-field image, the CNR value increases with the contrast-agent concentration.

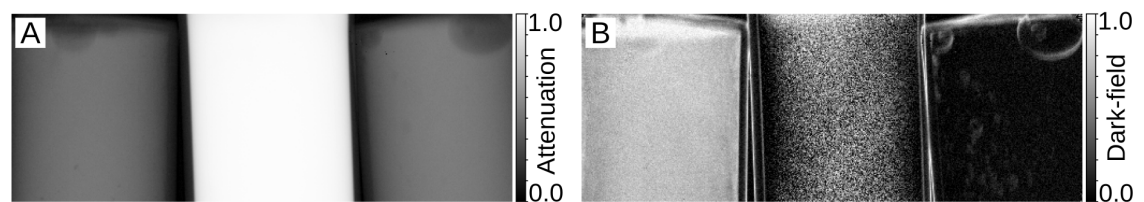


Figure 4.12: Comparison of dark-field and attenuation contrast enhancement. (A) Attenuation radiography of pure Optison contrast agent, iodine contrast agent (300mg/ml) and 0.9% NaCl in 5 ml syringes from left to right. Optison and NaCl present with similar gray values whereas the iodine contrast agent appears strongly hyperdense. Within 70×15 pixel regions in the middle of the syringes, the CNR between NaCl and iodine is $\text{CNR}_{\text{atc}} = 85.5$. (B) The dark-field contrast between Optison and NaCl is $\text{CNR}_{\text{dfc}} = 12.4$. Due to strong attenuation, iodine causes a noisy dark-field signal. The NaCl solution doesn't cause a dark-field signal but the air bubbles at the wall of the syringe produce a slight signal.

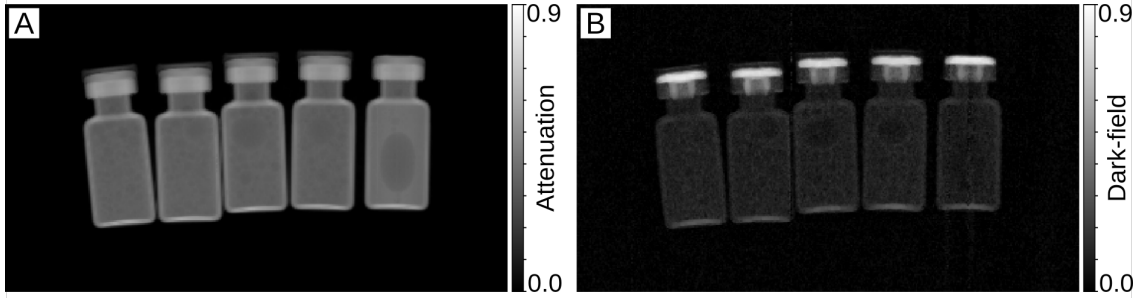


Figure 4.13: Radiography of Optison contrast agent in a large field of view dark-field scanner. The contrast agent has been imaged directly in the glass vial in a lying position. The vial on the left contains no contrast agent but 0.9%- NaCl solution as a reference. (A) Attenuation radiography shows a visual difference between the speckled contrast agent and the homogeneous NaCl solution ($\text{CNR}_{\text{atc}} = 5.0$ in a 20×15 pixel region). (B) Dark-field radiography shows no contrast between Optison and NaCl solution ($\text{CNR}_{\text{dfc}} = 0.7$).

appear slightly speckled causing a contrast of $\text{CNR}_{\text{atc}} = 5.0$. In the dark-field radiography, contrast agent and NaCl solution present with a nearly identical mean value resulting in a mean CNR_{dfc} of 0.7 in the dark-field image which confirms that there is no contrast enhancement by Optison at the geometry of setup D.

To evaluate the feasibility of X-ray dark-field angiography with Optison at setup C, contrast agent was injected into a coronary artery of a fresh porcine heart. Due to the instability of the microspheres on the timescale of a few minutes, the experiment was not successful and there was no measurable contrast enhancement in the images.

Luminity Luminity contrast agent causes a clear signal enhancement in dark-field radiography (Fig. 4.14B) at setup C. The contrast to noise ratio between Luminity and NaCl is $\text{CNR}_{\text{dfc}} = 8.2$. In attenuation radiography (Fig. 4.14A), Luminity and NaCl cause a very similar signal and can not be discriminated.

Direct comparison (Fig. 4.15) of their respective dark-field signal at setup C reveals a 1.5 times stronger dark-field signal for Luminity compared to Optison with $\text{CNR}_{\text{dfc}} = 8.2$ (Luminity) and $\text{CNR}_{\text{dfc}} = 5.5$ (Optison).

At setup D, Luminity contrast agent filled into a syringe shows a clear dark-field signal compared to a physiological NaCl solution filled into a petri dish (Fig. 4.16) in grating configuration 2 (see Sec. 4.1.2). While NaCl and Luminity show very similar attenuation values, the NaCl filled Petri dish is not visible at all in the dark-field. The respective CNR values between NaCl and Luminity are $\text{CNR}_{\text{dfc}} = 9.0$ in the dark-field image and $\text{CNR}_{\text{atc}} = 2.9$ in the attenuation image. Comparison of a representative line-plot in attenuation and dark-field reveals an overall higher noise level in the dark-field image but still a very clear signal from the contrast agent.

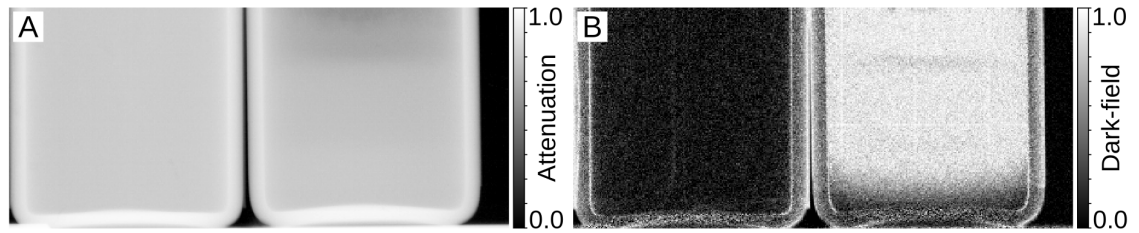


Figure 4.14: Signal strength of Luminity contrast agent in dark-field radiography. (A) In attenuation radiography, Luminity contrast agent (right) and the reference NaCl solution (left) appear very similar with a homogeneous signal. (B) In dark-field radiography, Luminity contrast agent can clearly be identified on the right side due to the enhanced signal. At the bottom of the glass vial, the dark-field signal is weaker, most likely due to the shorter radiographic path length through the rounded bottom. The CNR between physiological NaCl solution and Luminity in the dark-field image is $\text{CNR}_{\text{dfc}} = 8.2$

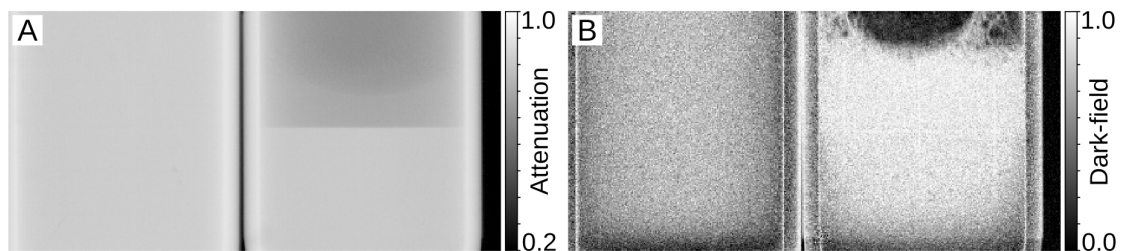


Figure 4.15: Comparison of signal strength between Optison and Luminity (A) Attenuation radiography of Optison (left) and Luminity (right). Both contrast agents present with very similar homogeneous gray values in attenuation radiography. The lower filling height of Luminity is visible. (B) Both contrast agents cause a homogeneous dark-field signal within the microsphere solution. The dark-field signal of the Luminity contrast agent is 1.5 times stronger than the signal of Optison.

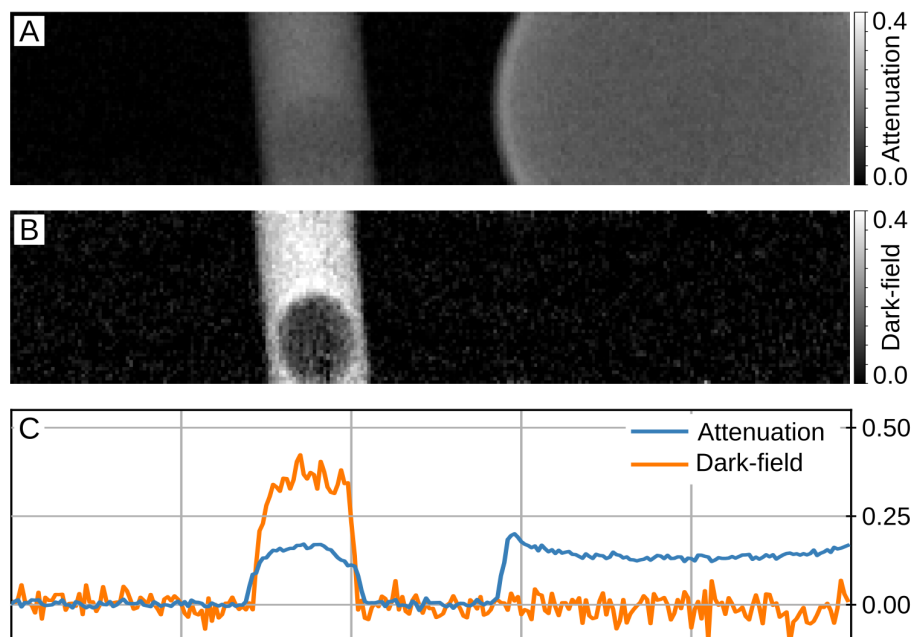


Figure 4.16: Radiography of Luminescence contrast agent at a large field-of-view dark-field scanner. (A) In attenuation radiography, the contrast-agent filled syringe and the Petri dish filled with NaCl show a very similar attenuation signal. (B) In dark-field radiography, the Petri dish and the NaCl solution are not visible. The Luminescence contrast agent causes a clear dark-field signal. (C) A representative line has been chosen for quantitative comparison of the signal strength. The blue line represents the attenuation signal, which has a similar level for the contrast agent and NaCl. The orange line represents the dark-field signal which shows an overall higher noise level but still a very clear signal from the Luminescence contrast agent and no signal from NaCl.

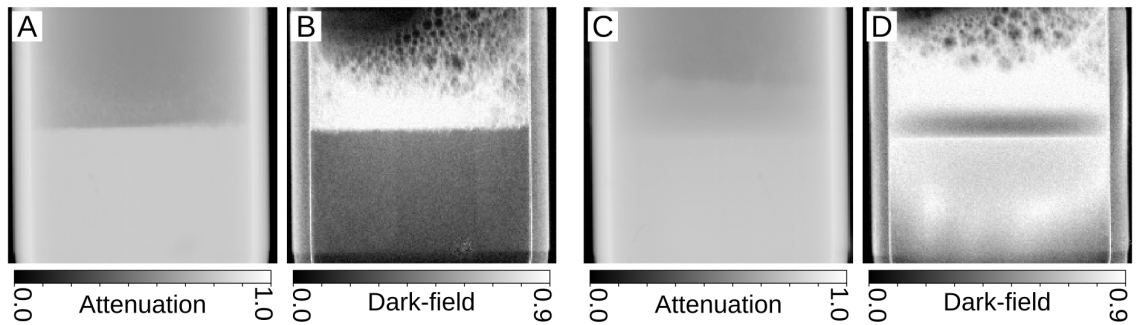


Figure 4.17: Visualization of microsphere instability. (A) Attenuation radiography of Luminity contrast agent without prior activation. The fluid causes a homogeneous hyperdense attenuation signal within the glass vial. (B) Without activation, only the foam above the fluid level cause a clear dark-field signal. (C) Attenuation radiography with activation and a long exposure time (11 phase steps with 10s exposure time). Due to the shaking process, the fluid level increased within the glass vial. (D) The activated Luminity contrast agent causes a clear dark-field signal. During the 110s of total exposure time, the microspheres start to burst, such that the fluid level decreases during exposure. This causes an artefact in the region of the fluid-gas interface.

A major experimental difficulty for the preclinical evaluation of microsphere based contrast agents for dark-field imaging is their in-vitro instability. Two of the main problems are visualized in Fig. 4.17. The maximum of the dark-field signal strength is achieved directly after resuspension or activation of the contrast agent, when the number of microspheres is at a maximum. From then on, the signal decreases until most of the microspheres are disaggregated as in Fig. 4.17B. This behaviour limits the possible acquisition time and therefore the achievable noise characteristics. If the acquisition time is longer than the time in which the microspheres are sufficiently stable, as in Fig. 4.17D, the image represents an average value of the decreasing dark-field signal and contains artefacts.

Sono Vue Sono Vue contrast agent causes a homogeneous signal in attenuation radiography (Fig. 4.18C) at setup C, very similar to that of NaCl in an identical glass vial (Fig. 4.18A) ($\text{CNR}_{\text{atc}} = 0.2$). The dark-field signal is weak (Fig. 4.18D) without contrast to water (Fig. 4.18B) ($\text{CNR}_{\text{dfc}} = 0.9$ in a 70×15 pixel region). To delay the rapid signal breakdown, the suspension has been activated with magnetic stirring during the measurement. The stirring bar is visible in both images (Fig. 4.18C,D) in the middle of the vial². Due to the weak signal from the pure solution, no further experiments were performed with Sono Vue contrast agent.

²Previously, the images were acquired without the stirring bar resulting in the same low dark-field signal. Thereby, it can be excluded that the weak signal is caused by the destruction of the spheres by the mechanical stirring process.

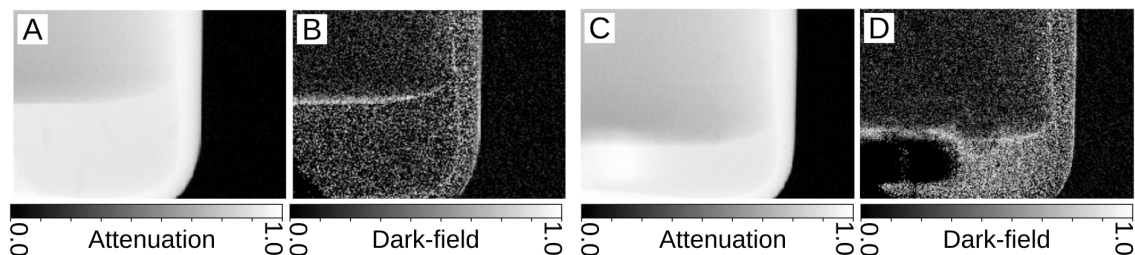


Figure 4.18: Signal strength of Sono Vue ultrasound contrast agent in dark-field radiography. (A) Attenuation and (B) dark-field radiography of physiological NaCl solution for comparison with Sono Vue contrast agent. (C) SonoVue fluid presents with a homogeneous attenuation signal similar to the NaCl solution. (D) The contrast agent shows almost no dark-field signal. The weak signal of the pure solution directly after resuspension disqualifies Sono Vue as a potential X-ray dark-field contrast agent.

PLGA spheres Self-made PLGA spheres were first investigated under a Stemi 2000-C (*Zeiss*, Oberkochen, Germany) light microscope (Fig. 4.19B). Due to the heat of the microscope illumination, the PLGA spheres collapsed rapidly on the microscope slide. Fig. 4.19C shows undamaged PLGA spheres in scanning electron microscopy (SEM) adapted from Li et al. [Li et al., 2014]. The microspheres under the optical microscope are from the large size batch and have therefore larger diameters than the microspheres in the SEM image.

The manufacturing process yields spheres with a broad size distribution. Three different size fractions were separated by adding sugar to the watery solution and thereby changing the solvent density. The radiographic signal strength at setup C can be seen in Fig. 4.20. While the attenuation signal is identical for all three groups and for the surrounding solvent, the microspheres can clearly be differentiated in dark-field radiography. The largest spheres show a strong signal at the interface between bubbles and solvent. The signal strength increases with decreasing sphere size. The smallest spheres present with the highest dark-field signal. The respective CNR values compared to water are from large (l) to small (s) $\text{CNR}_{\text{dfc}}^{\text{l,m,s}} = 2.8, 5.8, 7.1$ (in a representative pixel region of 70×15 pixel for the large and medium (m) sized spheres and 30×5 pixel for the small spheres).

Discussion

With the above described experiments, the commercially available ultrasound contrast agents were evaluated for their potential as X-ray dark-field contrast agents. Additionally, PLGA microspheres were manufactured in the lab and their dark-field signal strength was tested.

Microspheres in the Sono-Vue contrast agent had a very limited stability and pre-

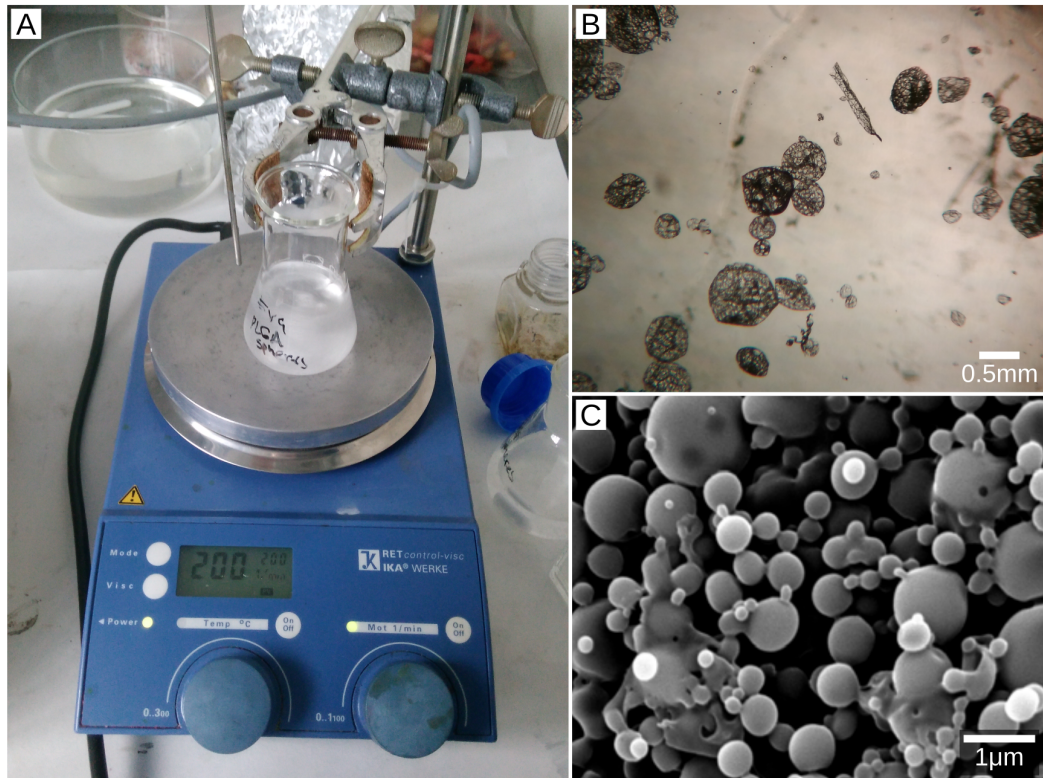


Figure 4.19: PLGA manufacturing in the laboratory. (A) Photo of the manufacturing process which includes heating and magnetic stirring of the PLGA-PVA solution on the depicted magnetic stirrer with an integrated heating plate. (B) Under optical light microscopy, the spheres collapsed during imaging due to the heat of the microscope illumination. The imaged spheres are from the large size batch. (C) Scanning electron microscopy adapted from Li et al. [Li et al., 2014] with undamaged PLGA spheres with an incorporated peptide.

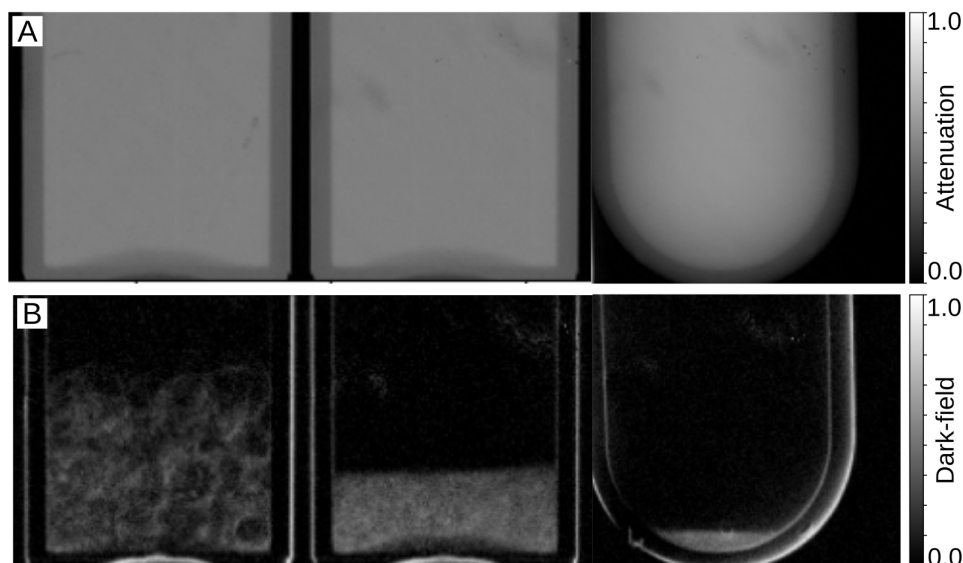


Figure 4.20: Signal strength of self-made PLGA spheres in dark-field radiography. (A) Attenuation radiography of PLGA spheres of different size. From left to right, the size of the spheres decreases. All batches show a similar attenuation signal which is homogeneous over the whole solution. (B) In dark-field radiography, the microspheres can be clearly distinguished from the water in the background. The signal strength is increasing with decreasing sphere size from left to right.

sented with a negligible dark-field signal strength. This is in accordance with the findings by Velroyen et al. [Velroyen et al., 2013]. Therefore, no further analysis and no further experiments were performed with this contrast agent. The manufacturer points out the vulnerability of the spheres, especially regarding pressure fluctuations. Thus, it can not be assessed to what extent the instability was caused by the experimental in-vitro settings. If the spheres are more stable within the physiological blood flow during an in-vivo application with a smaller size distribution and an overall higher sphere concentration, a sufficient dark-field signal could be possible.

Optison contrast agent showed a clear dark-field signal at setup C (correlation length $\leq 7.28\mu\text{m}$). Sphere stability was sufficient for clear results within the original vial as well as within a syringe. At the full-field scanner (setup D, correlation length $\leq 0.642\mu\text{m}$), the spheres could not be differentiated from water based on the dark-field signal. Instability of the spheres within a time scale of several minutes obstructed further experiments with a porcine heart. The injection of the microspheres into a coronary artery of the porcine heart to simulate dark-field angiography did not yield evaluable results as the spheres weren't stable enough within the needed time scale. Direct comparison revealed that the attenuation signal of diluted iodine based contrast agent is approximately seven times stronger than the dark-field signal of pure Optison at the chosen X-ray spectrum and interferometer

geometry. As the X-ray spectrum of the used setup provides a large proportion of photons around the K-edge of iodine, the presented values should be seen as a qualitative trend to classify the potential of dark-field contrast agents, rather than as a quantitative measure.

Luminess showed the best dark-field signal strength at both setups C and D (setup D was used in grating configuration 2, correlation length $\leq 2.46 \mu\text{m}$). The strong signal is in accordance with the microscopically observed high sphere concentration in the relevant size range and the comparably higher stability. However, stability was also not sufficient for the experimental simulation of X-ray dark-field angiography with a porcine heart, as described above for Optison.

The manufactured PLGA spheres showed a dark-field signal even for quite large sphere sizes. The signal increases with decreasing sphere size. The spheres were stable within the time frame of the experiments and could be used for longer measurements. A stronger signal could be realized by optimizing the manufacturing process and subsequent size separation. The experiments demonstrated that PLGA spheres are a potential candidate for systematic measurements with varying sphere diameters.

These experiments highlight the influence of the sphere stability on the dark-field signal strength in in-vitro experiments with ultrasound contrast agents. Even though the given properties like sphere diameter, size distribution and total concentration were quite similar for the three different contrast agents, their dark-field signal strength varied significantly. The appearance of the spheres under the microscope confirmed the correlation of dark-field signal strength and sphere concentration in the optimal size range around the setup's correlation length. From these findings, a few conclusions can be drawn regarding the design of a clinical X-ray dark-field contrast agent.

The concentration of spheres in the size range around the scanner's sensitive structure length must be maximized. This must be realized by mutually adapting the setup's sensitivity and the size distribution of the spheres. The upper size limit for the spheres is approximately the size of red blood cells to guarantee the ability to pass small blood vessels. The need for high concentrations limits the approach most likely to catheter examinations or bolus injections as previously concluded by Velroyen [Velroyen, 2015]. However, the restriction of a bubble-based contrast agent to the vascular system prevents the occurrence of a background signal due to extravasation as known from iodine contrast agents. For cardiac applications, the strong dark-field signal of the lung might overlay the signal of the contrast agent in projection radiography. Thus, it might be necessary to vary the structure sensitivity by changing the sample or patient position within the scanner and to choose spheres with a different size than the structure size of the lung. The possibility to vary the

scanner sensitivity to different structure sizes could be used to maximize the signal for the respective body part and for the contrast agent sphere size similar as in [Prade et al., 2016]. While the variation of the sample position is easily achievable within a laboratory table-top Talbot-Lau scanner, this might be more difficult for an approved patient scanner with a fringe scanning approach as in [Willer et al., 2018, Gromann et al., 2017a, Arboleda et al., 2020, Koehler et al., 2015].

For further laboratory experiments it would be beneficial to use microspheres with more controllable parameters and higher in-vitro stability regardless of the physiological compatibility. The experiments with self-made PLGA spheres indicated that the production of spheres with high stability and manageable properties is possible with simple methods. In principle, this type of spheres is also approved for in-vivo application. Such defined spheres could be used to further evaluate the optimum sphere size in the polychromatic case. Even though the prediction of the optimal dark-field signal by spheres with a diameter of 1.8 times the correlation length has been confirmed by different simulations of monochromatic setups, the polychromatic case has not been systematically evaluated. The energy dependence of the interferometer visibility modulates the signal at laboratory sources. While the signal strength decreases rapidly for sphere diameters below the mentioned optimum for monochromatic X-rays, this optimum might be broadened in the polychromatic case.

For conventional attenuation imaging, it is possible to produce a negative contrast by injection of CO₂ into the vessel system. Kariya et al. [Kariya et al., 2013] reported on the production of bubbles with diameters below 50 μm by cavitation and demonstrated the depiction of blood vessels with a phantom and an animal measurement with pigs. As those microbubbles provide strong refractive index fluctuations similar as the ultrasound contrast agents, their potential for dark-field contrast enhancement should be evaluated in the future.

4.4.3 Conclusion

At this point, the feasibility of X-ray dark-field contrast enhancement by off-label application of ultrasound contrast agents can neither be demonstrated nor discarded. Ultrasound contrast agents are very delicate and instable within ex-vivo or in-vitro applications. They are not suitable for quantitative in-vitro tests. However on a timescale of sufficient stability, dark-field contrast enhancement could be demonstrated at experimental Talbot-Lau setups. Further investigations on the optimization of the signal strength should be performed with stable spheres with controllable properties together with simulations of the experiments to develop a reliable simulation framework. Especially, PLGA based microspheres which can

easily be produced in the lab could be used for systematic investigations. Remaining open questions concern the lower concentration limit which can be detected in X-ray dark-field imaging with the anatomical background signal and the upper concentration limit that is physiologically acceptable. To achieve high sphere numbers in the relevant tissue it might be beneficial to use spheres with low diameters and to adapt the interferometer's sensitivity accordingly. High concentrations can be reached by catheter or bolus applications as also usual for specific iodine contrast agent examinations.

A breakthrough in this field could open up a very large market for X-ray dark-field imaging. This could drive the technological progress towards the completion of clinical Talbot-Lau X-ray machines and convince potential investors. Thus, dark-field contrast agents can be a cart horse for clinical grating-based imaging and the huge clinical potential of microspheres as a novel type of contrast agent should motivate further research effort.

4.5 Quantitative material decomposition

The main results of this chapter are published in Braig et al., Direct quantitative material decomposition employing grating-based X-ray phase-contrast CT, in Scientific Reports [Braig et al., 2018b] and Braig et al., Single spectrum three-material decomposition with grating-based X-ray phase-contrast CT, in Physics in Medicine and Biology [Braig et al., 2020a].

4.5.1 Clinical background

Thanks to its broad accessibility, fast image acquisition and continuous progress in dose reduction [Kane et al., 2008, Korn et al., 2012, Kim et al., 2015] computed tomography is an essential versatile tool in various diagnostic fields ranging from emergency care [Larson et al., 2011] to pediatrics [Miglioretti et al., 2013]. Specifically designed imaging protocols with optimized acceleration voltage, optional contrast agent application and organ specific gray value windowing allow the visualization of various healthy or pathological organ structures [Webb et al., 2019]. However, when it comes to materials that exhibit similar Hounsfield units (HU), a clear diagnosis is often not possible [Payabvash et al., 2014, McCollough et al., 2015b]. An example for the clinical relevance of material discrimination is depicted in Fig. 4.21 for two ischemic stroke patients who underwent interventional thrombectomy. The unenhanced control scan 12 hours after the intervention shows a hyperdensity in the subarachnoidal space for both patients. While follow-up magnetic resonance imaging (MRI) revealed a subarachnoidal bleeding for one patient, the hyperdensity was assigned to contrast agent extravasation via the damaged blood brain barrier for the other patient. An intracerebral hemorrhage is associated with high mortality and requires an entirely different therapy than the thrombolytic prevention of further ischemic events for the other patient [Gupta et al., 2010, Mokin et al., 2012]. Besides the discrimination of iodine contrast agent and blood, it can also be challenging to differentiate between these two materials and calcification as all three materials may present with almost identical attenuation values in conventional CT (see Fig. 4.21, black and white arrows).

Despite the similar attenuation, such materials have different chemical compositions with different atomic number, electron density and morphological substructure. These differences can be visualized by grating-based X-ray imaging with the availability of the conventional attenuation, phase-contrast and dark-field image. The simultaneous presentation of these three signals has been proven beneficial for various diagnostic questions, as described in this thesis (see Ch. 3, Sec. 4.2, Sec. 4.3 and Sec. 4.4). However, the availability of three complementary data-sets provides

the potential to extract even more quantitative information by material decomposition similar to DE-CT.

Within the last few years, dual-energy or spectral CT has provided a new level of quantitative accuracy for many diagnostic applications like stroke diagnosis, pulmonary perfusion imaging or bone mineral density determination [Thieme et al., 2008, Watanabe et al., 2009, Postma et al., 2012, McCollough et al., 2015a]. Depending on the technical realization, these machines use dual-source or dual-layer techniques, rapid kVp-switching [Sellerer et al., 2018] or spectral X-ray detectors to generate two complementary data-sets [Roessl and Proksa, 2007]. By interpreting the high and low energy images as two linearly independent basis components, algebraic basis transformation enables quantitative material separation. Thereby, it has been shown that DE-CT can help to reliably differentiate hemorrhage from iodine contrast agent extravasation without employing any additional radiation which helps to initiate the right therapy promptly [Phan et al., 2012, Gupta et al., 2010, Tijssen et al., 2014, Djurdjevic et al., 2017].

The precise determination of electron density and effective atomic number of different materials with gbpc-CT at synchrotron sources as well as at conventional lab-based X-ray tube sources has already been demonstrated [Herzen et al., 2009, Qi et al., 2010b, Willner et al., 2013b, Sarapata et al., 2015, Birnbacher et al., 2016, 2018b]. Here, we attempt to additionally exploit the complementary character of the signals to perform quantitative material decomposition. By that, the diagnostic advantages of gbpc-CT that have been reported within the last years are complemented by the extraction of various material specific image representations to catch up with the recent success of dual-energy imaging.

In a first study we evaluate the general feasibility and the quantitative accuracy of the approach with experiments at the quasi-monochromatic compact synchrotron source MuCLS and highlight the potential benefits of the method by the example of a chicken heart within an angiography scenario.

As a next step, the practicability of the method at different polychromatic X-ray tube sources is evaluated. Additionally, the potential diagnostic benefits are assessed within an experimental simulation of an unclear stroke situation. Most important, the approach is expanded from two-material decomposition based on the attenuation coefficient and the phase-contrast signal to three-material decomposition by taking the dark-field signal into consideration.

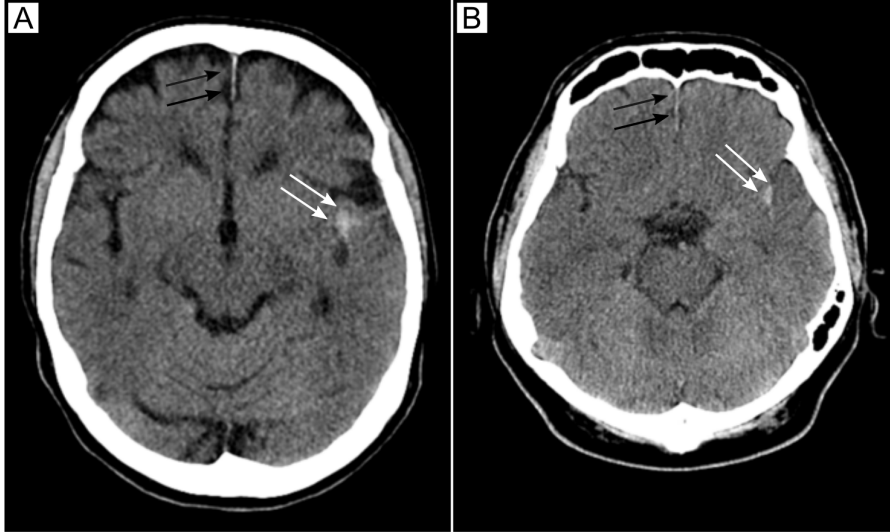


Figure 4.21: Unenhanced clinical control CT scans 12 hours after interventional thrombectomy. (A) 76 year old patient with a hyperdensity in the left insular region (white arrows, 57 HU) and partially calcified falx cerebri (black arrows, 58 HU). Follow-up MRI revealed a subarachnoidal bleeding. (B) 50 year old patient with a hyperdensity on the left insular region (white arrows, 55 HU) and a partial calcification of the falx cerebri (black arrows, 53 HU). Subsequent MRI showed no hemorrhage and the hyperdensity is consistent with iodine contrast agent extravasation after mechanical thrombectomy. Due to the similar attenuation, mechanically induced hemorrhage cannot be discriminated from extravasation of iodine-based contrast agent via the damaged blood brain barrier in conventional CT. Hemorrhage, contrast agent and calcifications present with nearly identical HU numbers for these patients. Retrospective analysis of patient’s image data was approved and conducted in accordance with the guidelines of the institutional review board.

4.5.2 Decomposition approach

With grating-based phase-contrast CT, three quantitative material parameters can directly and simultaneously be extracted from the examined object. These are the attenuation coefficient, the refractive index decrement and the linear diffusion coefficient which are energy- and material-dependent quantities (see also Sec. 4.1.3). Starting from these three images or data-sets, further quantitative information can be extracted.

Electron density The refractive index decrement of a compound of different elements with index i is related to the real part of the atomic scattering factor in forward direction $f_i^0(0)$

$$\delta(E) = \frac{r_0 h^2 c^2}{2\pi E^2} \sum N_i f_i^0(0), \quad (4.8)$$

with the classical electron radius r_0 , the Planck constant h , the speed of light c and the atomic density N_i of the element with index i . Far away from absorption edges the electrons of an atom can be considered to be quasi-free and the real part of the atomic scattering factor $f_i^0(0)$ can be replaced by the atomic number Z_i and thus $\sum N_i f_i^0(0) = \rho_e$ [Als-Nielsen and Des McMorrow, 2011]. In this case, the electron density is directly proportional to the measured refractive index decrement

$$\delta(E) = \frac{r_0 h^2 c^2}{2\pi E^2} \rho_e. \quad (4.9)$$

By that the energy dependence can be separated from the material dependence.

Effective atomic number The effective atomic number for compounds and mixtures can be interpreted as a weighted mean atomic number derived from the contributing materials

$$Z_{\text{eff}} = \sqrt[2.94]{\sum_i f_i \cdot Z_i^{2.94}}, \quad (4.10)$$

with f_i the fraction of the total number of electrons associated with each element and Z_i the atomic number of each element Qi et al. [2010b]³. Linear attenuation coefficient and electron density can be used to extract the effective atomic number from a grating-based CT measurement as a further energy independent material quantity.

The total attenuation coefficient can be expressed in terms of the interaction mechanisms, that contribute to X-ray attenuation. For the energy range, used for diagnostic imaging these are mainly the photoelectric absorption, incoherent Compton scattering and coherent scattering such that with the so called electronic interaction cross section $\sigma_i^e = \sigma_i/Z$ this can be written as

$$\mu_{\text{tot}}(E) = \rho_e \cdot (\sigma_{\text{ph}}^e(E, Z) + \sigma_{\text{incoh}}^e(E) + \sigma_{\text{coh}}^e(E, Z)), \quad (4.11)$$

[Jackson and Hawkes, 1981]. Material and energy dependence can be separated into two terms for the Compton effect

$$\mu_{\text{incoh}} = \rho_e \cdot \sigma_{\text{kn}}, \quad (4.12)$$

with the Klein-Nishina cross section σ_{kn} [Klein and Nishina, 1929]. For coherent scattering and the photo effect, the separation of the variables is not generally possible. For the diagnostic energy and material range, the following parametrization

³There exist different definitions for the effective atomic number in literature. A detailed comparison of these definitions can be found in [Singh et al., 2014].

of the photo-electric effect is widely used

$$\mu_{\text{ph}} = \rho_e C_P \frac{Z^{C_Z}}{E^{C_E}}. \quad (4.13)$$

Alvarez et al. suggested the following values for the empirical parameters in the relevant diagnostic regime $C_P = 9.8 \cdot 10^{-24}$, $C_Z = 3.8$ and $C_E = 3.2$ [Alvarez and Macovski, 1976]. If the contribution of the coherent scattering to the total attenuation is neglected, equations 4.12 and 4.13 can be used to extract the effective atomic number from the measured quantities μ_{tot} and ρ_e

$$Z_{\text{eff}} = \sqrt[3]{\left(\frac{\mu_{\text{tot}}}{\rho_e} - \sigma_{\text{kn}}\right) \cdot \frac{1}{C_P} \cdot E^{C_E}}. \quad (4.14)$$

As coherent scattering accounts for example for about 10% of the total attenuation coefficient of water at 25 keV another approach can be used to avoid neglecting the coherent scattering [Willner et al., 2013b, Birnbacher et al., 2018b]. From the measured total attenuation coefficient and electron density, the fraction of incoherent scattering in the total attenuation can be calculated such that

$$\frac{\mu_{\text{incoh}}}{\mu_{\text{tot}}} = \frac{\rho_e \sigma_{\text{kn}}}{\mu_{\text{tot}}} = \frac{\rho_e \sigma_{\text{kn}}}{\rho_e \sigma_{\text{tot}}^e} = \frac{\sigma_{\text{kn}}}{\sigma_{\text{tot}}/Z}. \quad (4.15)$$

This can be rearranged for the calculation of the effective atomic number

$$Z = \frac{\rho_e}{\mu_{\text{tot}}} \cdot \sigma_{\text{tot}}. \quad (4.16)$$

As the tabulated total interaction cross section $\sigma_{\text{tot}}(Z, E)$ is dependent on the atomic number and the energy, it must be interpolated along the effective atomic number axis, first.

Once the effective atomic number has been calculated, the simplified interaction parametrization can be used to calculate attenuation coefficient images of the investigated object at an arbitrary energy

$$\mu(E) = \rho_e \sigma_{\text{kn}}(E) + \rho_e C_P \frac{Z^{C_Z}}{E^{C_E}}. \quad (4.17)$$

This provides virtual monoenergetic images which are also extracted from DE-CT data in clinical imaging.

Basis transformation The measured quantities μ and δ are linearly independent and can therefore be seen as basis vectors that span a two-dimensional vector space. Therefore, algebraic basis transformation can be used to display the images in terms of specific materials as known from DE-CT. Here, the energy-independent material

vectors \vec{Z}_{eff} and $\vec{\rho}_e$ were derived from the measured quantities μ and δ as described above and were used as original basis vectors.

The dark-field signal is linearly independent from Z_{eff} and ρ_e , as well, and can therefore serve as a third basis vector. Basis transformation is obtained in two steps. First, the desired basis materials (here water (w), iodine (i) and hydroxyapatite calcification (c)) are expressed as vectors in the old basis system $B = (\vec{\rho}_e, \vec{Z}_{\text{eff}}, \vec{df})$ and written as columns of the matrix

$$\mathbf{B} = \begin{pmatrix} \rho_{e,w} & Z_{\text{eff},w} & df_w \\ \rho_{e,i} & Z_{\text{eff},i} & df_i \\ \rho_{e,c} & Z_{\text{eff},c} & df_c \end{pmatrix}. \quad (4.18)$$

Then, the transformation matrix \mathbf{T} must be found such that $\tilde{\mathbf{B}} = \mathbf{B}\mathbf{T}$. The new basis system $\tilde{B} = (\vec{w}, \vec{i}, \vec{c})$, which is spanned by the relative amount of the respective materials, is a standard basis (\mathbf{I}) and therefore $\mathbf{B}^{-1} \cdot \tilde{\mathbf{B}} = \mathbf{B}^{-1} \cdot \mathbf{I} = \mathbf{T}$. A more detailed description of the basis transformation procedure can be found in Appendix D.

4.5.3 Monochromatic proof of principle

The experimental feasibility of material decomposition with grating-based phase-contrast imaging was tested at the Munich Compact Light source (setup A). The quasi-monochromatic X-ray energy enables the evaluation of the quantitative accuracy of the approach with a test object consisting of several well-known materials. Additionally, the potential benefit of multiple image representations is demonstrated based on a gbpc-CT of a chicken heart.

Materials and methods

Experimental settings and imaging parameters The X-ray energy was tuned to 25 keV and the resulting spectrum at the position of the sample was measured with an energy-dispersive Amptek X-123 detector (*Amptek Inc.*, Bedford, Massachusetts) with a 500 μm Si sensor. The mean energy of the measured spectrum was $E_{\text{mean}} = 24.3 \text{ keV}$ and the intrinsic energy bandwidth was $\Delta E/E \approx 3\%$. The average photon flux during the tomographic measurements was $1.4 \cdot 10^{10}$ photons/s. To take the different energy dependency of the attenuation and the phase signal into account, individual effective mean interaction energies were assigned to the individual contrast channels. The energies were experimentally determined via a look-up table for the measured attenuation coefficient and refractive index decrement of a well-known PMMA rod. The density of the PMMA calibration rod was determined by measuring volume and weight and had a value of $\rho_{\text{PMMA}} = 1.189 \pm 0.005 \text{ g/cm}^3$. In total, 350 – 380 projections were taken over 360°. For every projection, seven

phase-steps with 3 s exposure time were acquired, resulting in a total measurement time of 4 - 6 h.

Sample preparation The monochromatic material decomposition was experimentally evaluated with two different samples. The first sample was designed to evaluate the method's quantitative accuracy and consisted of four different solid (s) and fluid (f) materials of known composition. The materials are ethanol (f), polymethylmethacrylat (PMMA) (s), polyoxymethylen (POM) (s), nylon (type 6) (s) and additionally a tube with coagulated blood (f) and a sodium iodide solution (f) (Fig. 4.22A). The sodium iodide (NaI) solution was prepared by mixing powdery NaI (*Sigma Aldrich*, Missouri, USA) with pure water to obtain a nominal concentration of $[\text{NaI}] = 5.9 \text{ mg/ml}$. This corresponds to an iodine (I) concentration of $[\text{I}] = 5.0 \text{ mg/ml}$ in water.

The second sample was a fresh chicken heart obtained at a local butchery (Fig. 4.26). Thus, no animals had to be sacrificed for this experiment. The sample was placed inside a conical plastic container which was then filled up with water. An intravenous injection line was filled with IMERON 300 (*Bracco Imaging Deutschland GmbH*, Konstanz, Germany) iodine contrast agent and was placed next to the heart. The contrast agent was diluted with water to get an approximate iodine concentration of $[\text{I}] = 40 \text{ mg/ml}$.

Image processing After tomographic reconstruction, a mean of 50 axial slices has been taken to improve the photon statistics for the cylindrical material phantom. For the chicken heart measurement, the raw images (attenuation image and phase-contrast image) have been post-processed with a dictionary-based denoising algorithm as proposed in [Mechlem et al., 2017, Elad and Aharon, 2010] to achieve a similar noise level as in the cylindrical phantom.

For the determination of the effective atomic number via Eq. 4.14 the empirical parameters C_P , C_Z and C_E from [Alvarez and Macovski, 1976] were adapted for the used X-ray energy in a prior parameter fit such that $C_P = 13.03 \cdot 10^{-24}$, $C_Z = 3.42$ and $C_E = 2.97$.

Starting from the effective atomic number and electron density images, two-material decomposition was performed as described above. Water and iodine were chosen as the two basis materials. The effective atomic number and electron density of 20 mg/ml NaI ($Z_{\text{eff,I}}, \rho_{\text{e,I}}$) and water ($Z_{\text{eff,W}}, \rho_{\text{e,W}}$) have been calculated from literature values [Schoonjans et al., 2011, Meyer, 1972] to define the two basis materials. By using a concentration of diluted iodine close to clinically relevant concentrations rather than elementary iodine mixed with water as a basis material, more precise

decomposition results can be achieved. [Mendonca et al., 2014].

Results

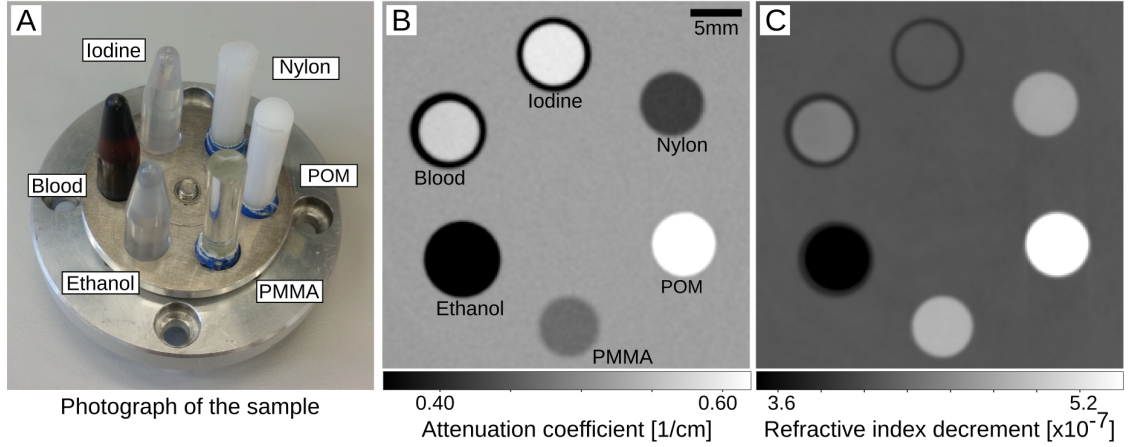


Figure 4.22: Grating-based phase-contrast CT of different materials. (A) Photograph of the sample consisting of 6 different materials. The attenuation coefficients (B) and refractive index decrements (C) are extracted via tomographic reconstruction from the processed stepping data. Comparison of the gray values and the gray value differences of the materials between the two image channels, reveals their complementarity which is the basic requirement for material decomposition.

Accuracy of attenuation coefficient and refractive index decrement measurement Tomographic reconstruction of the processed phase-stepping data yields quantitative maps of the attenuation coefficients and the refractive index decrements of the test phantom as displayed in Fig. 4.22. In the attenuation image, blood, iodine and POM appear hyperdense compared to the surrounding water; nylon, PMMA and ethanol appear hypodense (Fig. 4.22B). In the phase image, nylon, POM, PMMA, and blood appear brighter than the surrounding water; ethanol appears darker and iodine can not be differentiated from the background (Fig. 4.22C). This demonstrates the complementarity of the two data sets which is the basic requirement for material decomposition. The energy calibration yields an effective energy of $E_{\text{eff}}^{\mu} = 24.6 \pm 0.2 \text{ keV}$ for the attenuation image and $E_{\text{eff}}^{\delta} = 23.8 \pm 0.2 \text{ keV}$ for the phase-contrast image. These values are close to the measured mean energy of $E_{\text{mean}} = 24.3 \text{ keV}$ at the position of the sample. Due to the different energy dependence of the respective underlying photon interactions and the interferometric method, a difference of the two values is expected.

The quantitative values of the measured attenuation coefficients μ_m and refractive index decrements δ_m are extracted as the mean value of a region of interest of 20×20 pixel. They are given in Tab. 4.4 together with the reference values cal-

	μ_m [cm ⁻¹]	μ_l [cm ⁻¹]	$\delta_m \cdot [10^{-7}]$	$\delta_l \cdot [10^{-7}]$
NaI (5.9 mg/ml)	0.597 ± 0.006	0.609	4.08 ± 0.07	4.07
Blood	0.568 ± 0.006	0.574	4.31 ± 0.07	4.27
Ethanol	0.323 ± 0.006	0.325	3.25 ± 0.06	3.27
PMMA	0.470 ± 0.006	0.470	4.70 ± 0.06	4.70
POM	0.628 ± 0.006	0.628	5.55 ± 0.06	5.55
Nylon	0.423 ± 0.006	0.419	4.61 ± 0.06	4.58
Water	0.523 ± 0.006	0.523	4.07 ± 0.06	4.07

Table 4.4: Quantitative attenuation coefficients and refractive index decrements. Comparison of measured (m) linear attenuation coefficients μ_m , and refractive index decrements δ_m with literature (l) values (μ_l, δ_l) for the test phantom at an effective energy of $E_{\text{eff}}^\mu = 24.6$ keV for the conventional attenuation image and $E_{\text{eff}}^\delta = 23.8$ keV for the phase-contrast image. The literature values are calculated from tabulated values from the NIST database [Hubbell, 1995] for the four test materials, from [Boone and Chavez, 1996] for blood and from [Meyer, 1972] for the NaI solution. The given uncertainty includes the standard deviation of the image region and the systematic error.

culated for the respective energy from tabulated values from the NIST database [Hubbell, 1995] for the test materials and from [Boone and Chavez, 1996] for blood and from [Meyer, 1972] for the NaI solution. By that, the quantitative accuracy of the measured attenuation coefficients for the four well-defined materials is determined to less than 0.9% deviation from the reference value and for the refractive index decrements less than 0.6%. Systematic errors on μ_m and δ_m originating from inaccuracies of the interferometer geometry have been evaluated with Gaussian error analysis and were found to be smaller than the standard deviation of the respective measured values. The given error margins in Tab. 4.4 consist of the systematic error resulting from the inaccuracy of the effective energy determination and the statistical error in the respective image region. For blood and the NaI solution, the deviation from the reference value is larger than for the other materials. The literature values for blood refer to uncoagulated blood, but the measured blood sample was a blood coagulum. The partial separation of the watery blood plasma from the cellular components, can explain the trend towards the lower attenuation coefficient and the higher refractive index decrement. It is assumed, that the deviation of the NaI solution from the reference value indicates an inaccuracy in the preparation process. An in-depth analysis of the NaI-solution preparation accuracy revealed, that the measured concentrations are systematically 7 – 14% lower than the nominally prepared concentrations. Sodium iodide shows a strong hygroscopic behavior which can lead to an overestimation of the absolute NaI weight during preparation. The measured attenuation value at $E_{\text{eff}}^\mu = 24.6$ keV of the NaI solution corresponds to a concentration of $[\text{NaI}] \approx 5.1$ mg/ml corresponding to $[\text{I}] \approx 4.3$ mg/ml (nominally prepared value was $[\text{NaI}] = 5.9$ mg/ml).

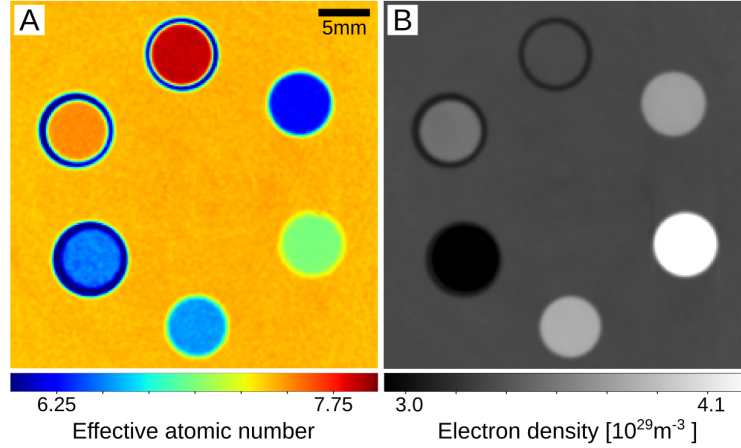


Figure 4.23: Effective atomic number and electron density. (A) The effective atomic number map is displayed in pseudo colors as in clinical dual-energy CT. The distribution of the values ranges from $Z_{\text{eff}} \approx 6.25$ for nylon to $Z_{\text{eff}} \approx 7.99$ for iodine. (B) The electron-density values can directly be derived from the measured refractive index decrements.

Accuracy of derived effective atomic number and electron density Fig. 4.23 shows the images of the effective atomic number and the electron density derived from the measured data sets. The atomic numbers are displayed in pseudo colors as usual in clinical DE-CT. The electron density is directly proportional to the refractive index decrement (Eq. 4.9) and therefore, the two images look the same. At the inner and outer edges of the tubes, the effective atomic number values show an overshooting artifact. This artifact can most likely be correlated with pixels affected by partial volume effects in the original reconstruction of μ and δ . I.e. pixels, where a strong contrast is present within the pixel or - due to imperfect alignment - several pixels. Thus, the measured μ and δ values are quantitatively not correct and the derivation of the effective number according to Eq. 4.14 doesn't yield correct values in the concerned pixels.

The quantitative values for the effective numbers and the electron densities in Tab. 4.5 were extracted from the same 20×20 pixel regions-of-interest as the values in Tab. 4.4. For compounds and mixtures, the effective atomic number is only an auxiliary quantity and there are slightly different definitions for its calculation. Thus, two reference values (Z_{eff,l_1,l_2}) are given for each material, if available. The subscript l_1 indicates reference values from Qi et al. [Qi et al., 2010b], the subscript l_2 indicates reference values from the XmuDat library [Hubbell, 1995, Boone and Chavez, 1996]. The measured values are systematically larger ($< 2\%$ deviation) than the values from both literature sources.

The deviation of the measured electron-density values from the literature values fluctuates between no deviation at all to $\approx 0.8\%$ relative deviation for nylon.

	$Z_{\text{eff},m}$	Z_{eff,l_1}	Z_{eff,l_2}	$\rho_{e,m} \cdot [10^{29} \text{m}^{-3}]$	$\rho_{e,l} \cdot [10^{29} \text{m}^{-3}]$
NaI (5.9 mg/ml)	7.97 ± 0.06	-	-	3.34 ± 0.07	-
Blood	7.60 ± 0.06	-	7.74	3.54 ± 0.08	-
Ethanol	6.52 ± 0.07	6.35	-	2.69 ± 0.07	2.68
PMMA	6.58 ± 0.03	6.47	6.56	3.86 ± 0.06	3.86
POM	7.05 ± 0.05	6.95	7.03	4.56 ± 0.06	4.56
Nylon	6.24 ± 0.06	6.12	6.21	3.79 ± 0.06	3.76
Water	7.51 ± 0.05	7.42	7.51	3.34 ± 0.06	3.34

Table 4.5: Quantitative effective atomic numbers and electron densities. Comparison of the effective atomic numbers Z_{eff} and the electron densities ρ_e derived from the measured data with different reference values (subscript $l_{1,2}$ for two different literature sources ([Qi et al., 2010b] or [Hubbell, 1995, Boone and Chavez, 1996])). The given uncertainty includes the standard deviation of the image region and the systematic error.

Material decomposition accuracy of the iodine concentration With the described basis transformation approach, the quantitative iodine and water content in every image voxel was derived from the electron density and effective atomic number data sets. Fig. 4.24A shows the quantitative iodine map with an iodine concentration of $[I] \approx 4.6 \text{ mg/ml}$ within the 20×20 voxel region inside the iodine filled tube and values $\leq 0 \text{ mg/ml}$ everywhere else. Compared to the concentration calculated from the measured attenuation coefficient, this value deviates by $\approx 0.3 \text{ mg/ml}$.

The accuracy of iodine quantification has been analyzed with a separate measurement of different iodine concentrations and the accuracy for four different concentrations between $1 - 5.3 \text{ mg/ml}$ NaI was better than 0.7 mg/ml for decomposition into water and sodium iodide.

From the quantitative iodine image, a binary iodine map was extracted and the pixels with a positive iodine concentration were replaced by the attenuation values of water in the conventional attenuation image. This leads to a very simple version of a so called virtual non-contrast (VNC) image (Fig. 4.24B) which is a specific feature of DE-CT scanners to provide a native image that simulates the situation before contrast agent injection [Johnson et al., 2007].

Virtual mono-energetic images The determined effective atomic numbers and electron densities are inserted to Eq. 4.17 to generate images at an arbitrary virtual energy. This has been done exemplary for virtual energies of $E_{1,2,3}^{\text{VMI}} = 25, 70, 120 \text{ keV}$ (Fig. 4.25). For 25 keV virtual energy, the image looks very similar to the original measurement with an effective energy $E_{\text{eff}}^{\mu} = 24.6 \text{ keV}$. The determined attenuation coefficients agree very well with the calculated theory values for 25 keV with an error smaller than 1.3% .

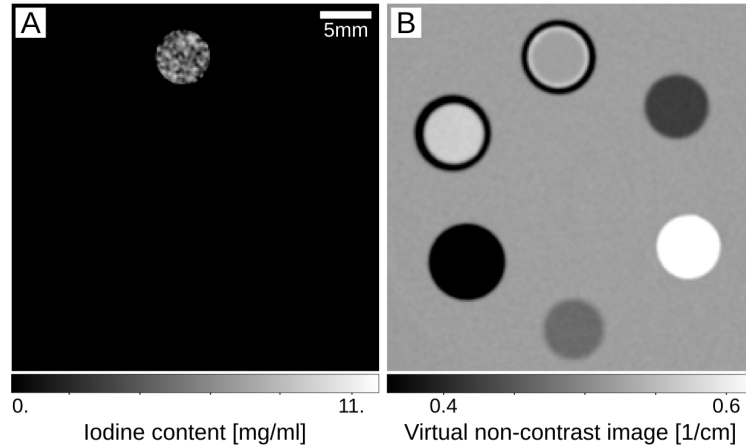


Figure 4.24: Iodine content and virtual non-contrast image. (A) The material decomposition approach transforms the measured μ and δ data sets into the new basis spanned by the relative water and iodine content. The quantitative iodine map shows a value of $[I] \approx 4.6$ mg/ml for the iodine solution and values ≤ 0 mg/ml for everything else. (B) From the quantitative iodine map a binary mask for positive iodine values can be derived. The virtual non-contrast image is then generated by replacing those iodine containing voxels in the conventional attenuation image with the attenuation value of water (or of the relevant surrounding material value in diagnostic imaging).

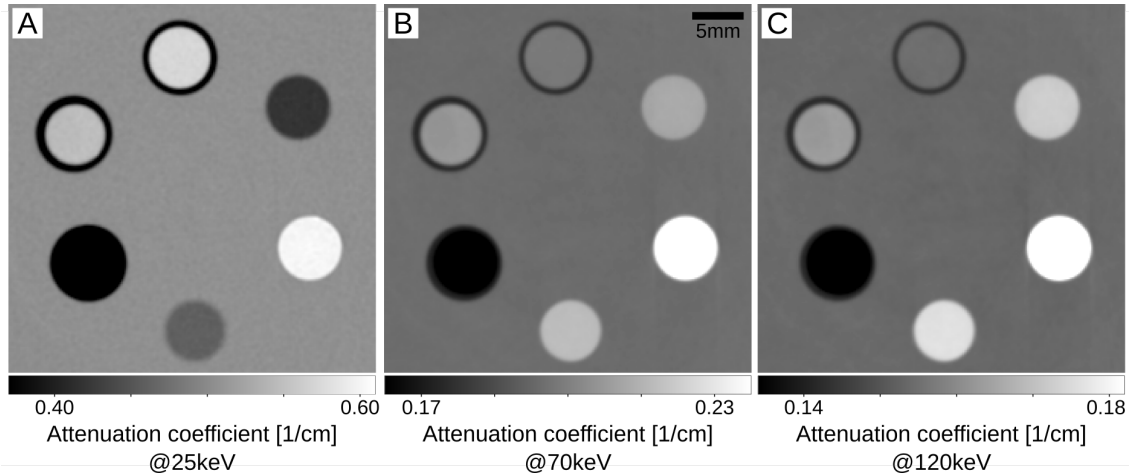


Figure 4.25: Virtual monochromatic images. (A) The virtual monoenergetic image at $E_1^{\text{VMI}} = 25$ keV looks very similar to the conventional attenuation image that was acquired at the quasi-monochromatic compact light source. (B) For higher energies, $E_2^{\text{VMI}} = 70$ keV, the contribution of the photo-electric effect decreases and the virtual monoenergetic images are dominated by the contribution of the Compton effect. (C) The VMI at $E_3^{\text{VMI}} = 120$ keV has a very similar appearance as the original electron density map.

Also for the virtual energy of 70 keV, deviations from the theoretical values are smaller than 0.8 %. The used interaction parametrization does not model K-edge discontinuities and thus no increase in iodine contrast can be expected in the virtual monoenergetic images above the K-edge of iodine.

At 120 keV the virtual monoenergetic data matches the literature values with an error of less than 0.6 %. The contribution of the photo effect is decreasing with increasing photon energy and the image is dominated by the Compton effect contribution which is proportional to the electron density. Therefore, the appearance of the 120 keV image is very similar to the electron density image.

Application to a biological sample The grating-based phase-contrast CT based material decomposition is demonstrated with a chicken heart in Fig. 4.26. In the conventional attenuation image (Fig. 4.26B), the soft-tissue structures of the heart can hardly be differentiated. Fat and the plastic tube appear hypodense against all other tissues which have similar gray values as water. On the upper right, the small contrast agent filled tube appears hyperdense. The refractive index image (Fig. 4.26C) reveals detailed contrast for different anatomical structures like muscle, fat and blood vessels (most likely the aorta and two vessels of the low pressure system) but no contrast between iodine and the surrounding water. The effective atomic number map (Fig. 4.26D) shows an increased value for the iodine contrast agent and similar effective atomic numbers for all other materials. In the quantitative iodine map (Fig. 4.26E) only the contrast agent shows up with a positive value of $[I] \approx 43$ mg/ml. The virtual non-contrast image (Fig. 4.26F) is just the conventional attenuation image with the iodine containing voxels replaced with the attenuation coefficients of water. Within the virtual monoenergetic images (Fig. 4.26G,H,I) it can be seen, that the Compton effect dominates the image formation already at the intermediate energy of $E_2^{\text{VMI}} = 70$ keV for the low atomic number materials of this sample, such that the image looks very similar to the phase image. At $E_3^{\text{VMI}} = 120$ keV, a difference between the monoenergetic image and the phase-contrast image is only visible for the iodine filled tube. The virtual monoenergetic image at $E_1^{\text{VMI}} = 25$ keV looks very similar to the conventional attenuation image as expected for the quasi monochromatic X-ray energy of $E_{\text{eff}}^{\text{H}} = 24.6$ keV.

Discussion

Grating-based phase-contrast CT at a quasi-monochromatic compact synchrotron source provides simultaneous access to accurate quantitative values for the linear attenuation coefficient and the refractive index decrement or the electron density with less than 1 % deviation from literature values. The different material and

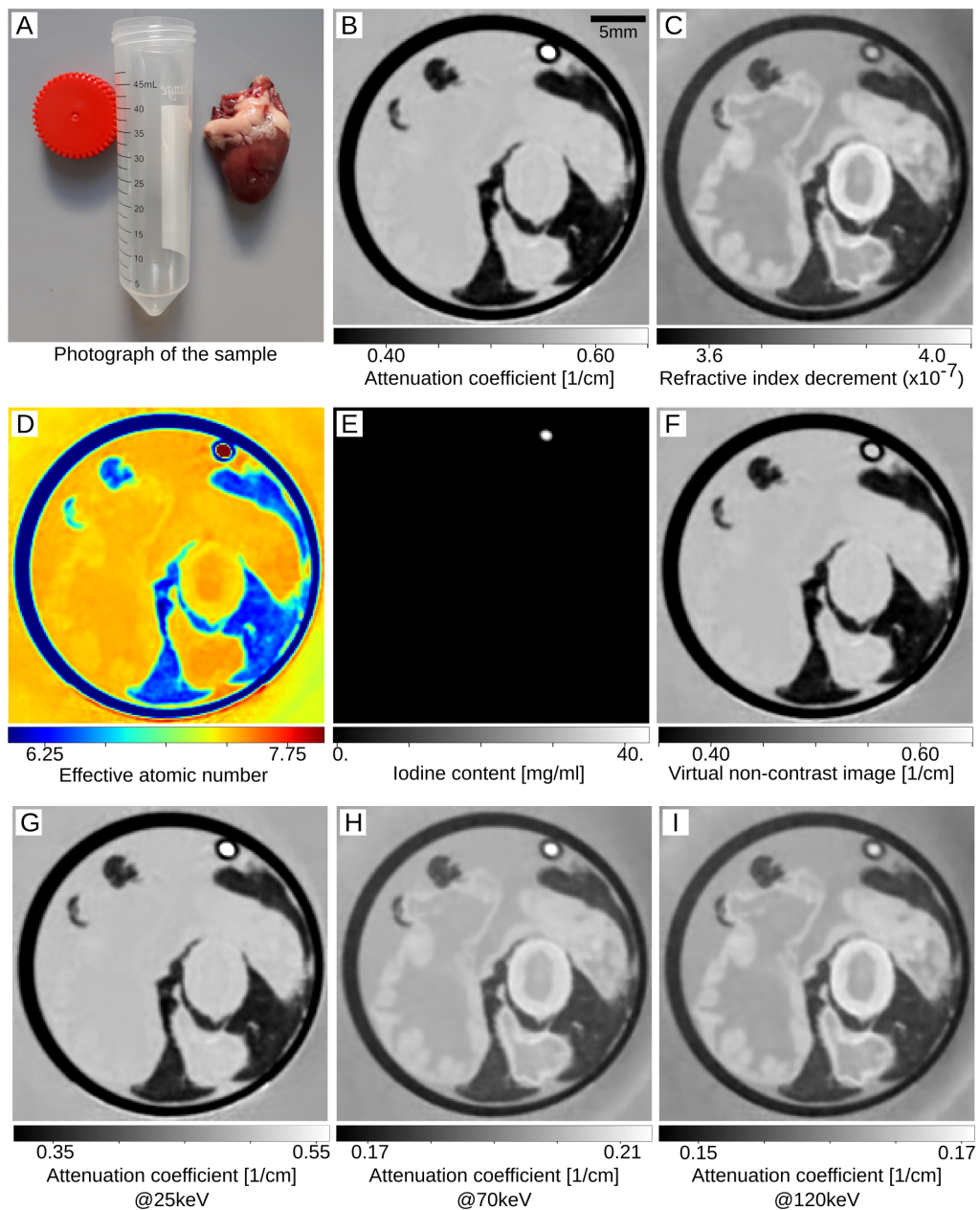


Figure 4.26: Material decomposition with a chicken heart. (A) Photograph of a fresh chicken heart next to the measurement container. (B) The conventional attenuation image shows very limited soft-tissue contrast. (C) The phase-contrast image reveals good contrast between soft-tissues but no contrast between iodine and the surrounding water. (D) The effective atomic number map shows slight variations between the different structures displayed in pseudo colors. (E) The quantitative iodine map yields an iodine concentration of $[I] \approx 43$ mg/ml within the contrast agent filled tube. (F) The virtual non-contrast image shows the native attenuation image without contrast agent. (G) The virtual monoenergetic image at $E_1^{\text{VM}} = 25$ keV looks very similar to the conventional attenuation image. For the higher energies (H, I) the Compton effect dominates the image formation and the images appear similar as the phase image.

energy dependencies of the underlying photon-matter interactions lead to complementary information in the two images. This is the basis for quantitative material decomposition. With simple algebraic basis transformation and an established model for the parametrization of the photon interactions [Alvarez and Macovski, 1976], multiple images were calculated from one tomographic acquisition. By that the originally measured attenuation coefficients and refractive index decrements have been used to create an effective atomic number map, a quantitative iodine map, a virtual native image and different virtual monoenergetic images. The quantification of the iodine concentration by material decomposition is with an uncertainty of ± 0.7 mg/ml slightly less accurate than reported for commercially available dual-energy scanners (0.2 mg/ml in [Ehn et al., 2017b], 0.5 mg/ml in [Faby et al., 2015]). This can most likely be assigned to the straight forward modeling of the photon interactions. The applied model has two major drawbacks. First, the assumption of the separability of material and energy dependencies in photo and Compton effect is an empiric approximation optimized for a range of specific materials and energies. Therefore, the combined dependency on both material and energy is not described correctly for X-ray attenuation. Additionally, the model neglects the contribution of the coherent scattering which accounts for example for about 10% of the total attenuation coefficient of water at 25 keV [Hubbell, 1995, Boone and Chavez, 1996]. Further, additional components of the experimental setup, like the energy dependent visibility of the interferometer or the spectral detector response have not been considered. The effective interaction energy determined from the PMMA rod is well suited for materials with similar attenuation properties but fails for materials with significantly deviating atomic composition and electron configuration. Especially for iodine which has a K-edge discontinuity at 33.17 keV, this deviation should be accounted for. Due to the quasi-monochromatic character of the MuCLS, spectral effects have only a minor influence within this study.

However, these limitations do not arise from the grating-based phase-contrast approach itself, but from the applied interaction model. On the contrary, the method brings specific advantages for image based material decomposition. The images are perfectly spatially registered due to the simultaneous acquisition, independent of the implemented detector type. In contrast to dual-energy imaging, grating-based phase-contrast imaging provides the total attenuation coefficient and the refractive index decrement within a single measurement. With the latter being proportional to the electron density, this material quantity can be directly extracted from the measurement without further image processing. In clinical X-ray imaging many questions are related to the differentiation of materials with different atomic numbers (e.g. contrast agents, calcifications, kidney stones) or tissues with different electron density (e.g. brain parenchyma, breast tissue, coagulated blood). Thus,

the simultaneous and direct access to the linear attenuation coefficient as well as the electron density in grating-based imaging can be a great benefit in a diagnostic context. The demonstration of the diagnostic potential of grating-based material decomposition in a clinically relevant sample will be the next step.

Altogether, the method provides improved soft-tissue contrast via the phase image, quantitative material concentrations, an effective atomic number map and virtual monochromatic images at any desired energy. With the additional availability of the conventional attenuation image this sums up to a significant gain of information density in a single CT acquisition.

With the presented results the general feasibility of quantitative material decomposition by grating-based phase-contrast CT has been demonstrated. The quasi monochromatic X-ray source with an X-ray energy below the absorption K-edge of iodine has been chosen to enable the quantitative analysis of the accuracy of the approach.

To make this technique available for clinical CT, the feasibility with clinical imaging components and parameters must be evaluated, especially the transfer to conventional X-ray tube setups with a broad energy spectrum and a high mean energy. The feasibility of the accurate determination of the effective atomic number and the electron density with polychromatic grating-based phase-contrast CT has previously been demonstrated [Qi et al., 2010a, Birnbacher et al., 2018b]. The crucial requirement for the decomposition approach is the complementarity of the original signals. This complementarity decreases towards high interaction energies where the attenuation image is dominated by the Compton effect and therefore represents mostly the distribution of electron densities instead of a combination with the effective atomic number. In the case of clinical material decomposition, materials like calcium or iodine are of interest. With their comparably higher atomic number, the crucial complementarity of the attenuation and phase-contrast information remains towards higher energies. Thus, the transfer of the described approach to conventional X-ray tube setups and its application to a simulated stroke setting will be evaluated within the next section.

4.5.4 Three-material decomposition at polychromatic X-ray tube sources

The feasibility of grating-based material decomposition at conventional polychromatic X-ray sources was evaluated at setup B, operated with more than 40 keV mean energy. Additionally, the approach was extended from two- to three-material decomposition by taking the dark-field signal into account. The potential clinical benefits through simultaneous differentiation of blood coagula, contrast agent and hydroxyapatite clusters in a simulated stroke setting were evaluated at setup C.

Materials and methods

Experimental settings and acquisition parameters Two different imaging setups have been used to demonstrate the performance of grating-based material decomposition with polychromatic broad X-ray spectra.

The quantitative accuracy of iodine decomposition has been evaluated at Setup B operated at 60 kV acceleration voltage and a power of 120 W. The mean effective energy has been derived from a simulated tungsten spectrum (simulated with an adapted version of Spektr [Siewerdsen et al., 2004]) under consideration of all absorbers in the beam path and the energy weighting introduced by the scintillator of the detector. This yields an effective mean energy of $E_{\mu} = 41.1$ keV which was assumed as the effective interaction energy for the attenuation contrast images. Phase and dark-field signal are additionally affected by the energy dependence of the interferometer's visibility

$$\nu(E) = \sin\left(\frac{\pi}{2} \cdot \frac{E_0}{E}\right)^2, \quad (4.19)$$

with the interferometer's design energy E_0 [Chabior, 2011]. The equation is valid for a π -shifting phase grating with a duty cycle of 0.5. Additional consideration of this dependency leads to a mean energy of $E_{\delta} = 43.0$ keV which was used as effective interaction energy for the phase-contrast images. Due to the geometric magnification of 1.7, the effective pixel size was $(115 \times 115) \mu\text{m}^2$. Phase-stepping was performed with 7 steps with 5 seconds exposure time and with 420 projections equidistantly distributed over 360° , resulting in a total acquisition time of ≈ 7 h.

For the demonstration of three-material decomposition in an experimentally simulated stroke scenario, setup C was used at an acceleration voltage of 50 kV and 1.2 kW tube power. The effective interaction energies have been determined to $E_{\mu} = 36.2$ keV and $E_{\delta} = 35.9$ keV from a measured tube spectrum. With a geometric magnification of 2.1, the effective pixel size was $p_{\text{eff}} = (144 \times 144) \mu\text{m}^2$.

Phase-stepping was performed with 11 steps and 4 seconds exposure time. With 1200 projections equidistantly distributed over 360° the total acquisition time was ≈ 33 h.

Sample preparation Iodine solutions were prepared by mixing powdery potassium iodide (KI) (*Sigma Aldrich, Missouri, USA*) with pure water. The nominal iodine concentrations were 1.0, 1.5, 2.0, 2.5 and 3.0 mg/ml. Prior to the actual material decomposition measurements, the concentrations were verified by a measurement at the Munich Compact Light Source (MuCLS, Setup A). Via the measured attenuation coefficients, the actual iodine concentrations have been determined to (1.1 ± 0.1) mg/ml, (1.7 ± 0.1) mg/ml, (2.2 ± 0.1) mg/ml, (3.1 ± 0.1) mg/ml and (3.6 ± 0.1) mg/ml with the statistical error derived from the standard deviation of the attenuation coefficient measurement. There was a time gap of seven weeks between the actual decomposition experiment and the verification measurement. During that time, an unknown amount of water could have evaporated from the plastic tubes resulting in different iodine concentrations at the time of the verification measurement. All iodine concentrations indicated from here on, refer to the concentrations determined at the MuCLS.

In accordance with local ethics committee decision No. 97/18S, a small amount of blood has been drawn from a volunteer person. The blood has slightly been stirred during the coagulation process and some of the separating plasma has been removed to get a homogeneous blood coagulum. The five different contrast agent solutions and the coagulated blood were poured into six small plastic tubes (0.54 cm diameter) and mounted on a cylindrical sample holder (see Fig. 4.27A) for tomography at setup B. A PMMA rod is mounted in the middle of the sample holder as a reference material.

To experimentally simulate an unclear stroke situation, a small part of the frontal lobe of a porcine brain was used. The sample was obtained from a local butchery such that no animals had to be sacrificed for this study. It was cut to fit into a conical plastic container with 2.9 cm outer diameter. The tissue was fixated in 4% formaldehyde solution. Additionally, a small plastic tube (0.54 cm outer diameter) filled with coagulated blood and two tubes filled with iodine contrast agent (2.7 mg/ml iodine in pure water) were placed next to the brain tissue. A small calcification was attached to the tube wall of one of the iodine filled tubes. The calcification was manufactured by mixing solid hydroxyapatite powder (*Sigma Aldrich, Missouri, USA*) with n-Butyl-2-Cyanoacrylat tissue glue (*Aesculap AG, Tuttlingen, Germany*). This mimicks the chemical composition of hydroxyapatite calcifications in a tissue matrix [Mechlem et al., 2018].

Image processing Attenuation, phase-contrast and dark-field datasets were obtained by tomographic reconstruction of the processed stepping data, as described in Sec. 4.1.3. The data sets of the cylindrical iodine concentration phantom were averaged along the cylinder axis for 30 slices. The data sets of the brain sample were averaged by a $4 \times 4 \times 4$ pixel binning.

The attenuation coefficient data sets were then converted to Hounsfield units (HU) as usual for clinical CT imaging. Analogously, the refractive index decrement images were converted to phase Hounsfield units (HUp) as described in 4.1.3. The effective atomic number was determined via Eq. 4.16, the electron density was determined via Eq. 4.9.

The entries of the original basis system matrix \mathbf{B} were determined for the three basis materials (water, 2 mg/ml potassium iodide and hydroxyapatite powder) in a previous measurement at the MuCLS (Setup A). The dark-field signal (df) was normalized to the maximum value measured for the hydroxyapatite powder within this calibration measurement.

Two-material decomposition has been performed as for the previous monochromatic measurements with the effective atomic number and electron density values for water and 2 mg/ml KI. For three-material decomposition, the dark-field signal was used additionally and the hydroxyapatite powder served as a third basis material. In contrast to the first verification measurement described in Sec. 4.5.3, these values were not taken from literature but from the previous measurement at the MuCLS.

Results

Quantitative blood iodine separation A scatter plot of attenuation coefficients and refractive index decrements demonstrates the potential of grating-based phase-contrast CT for the discrimination of hemorrhage and iodine contrast agent (Fig. 4.27B). While the measured attenuation coefficients of the blood sample and 1.1 mg/ml iodine solution are very similar, the refractive index decrement allows a clear differentiation. The difference of the mean refractive index of the blood sample ($\delta_{\text{blood}} = 1.25 \cdot 10^{-7}$) and of the lowest iodine concentration ($\delta_{\text{iod1}} = 1.29 \cdot 10^{-7}$) is more than 28 standard deviations ($\bar{\sigma} \leq 1.43 \cdot 10^{-10}$). The iodine concentration determined within the quasi-monochromatic measurement at the MuCLS is indicated above the respective data points as (1.1 ± 0.1) mg/ml, (1.7 ± 0.1) mg/ml, (2.2 ± 0.1) mg/ml, (3.1 ± 0.1) mg/ml and (3.6 ± 0.1) mg/ml iodine in water.

The conventional attenuation image of the test phantom is transformed to Hounsfield units and displayed in a window from 0 to 200 HU (indicated as [0; 200] HU) in Fig. 4.28A. The mean HU values in (15×15) pixel regions within the iodine solutions increase with the amount of iodine (62.0, 88.5, 118.5, 147.9, 176.4 HU).

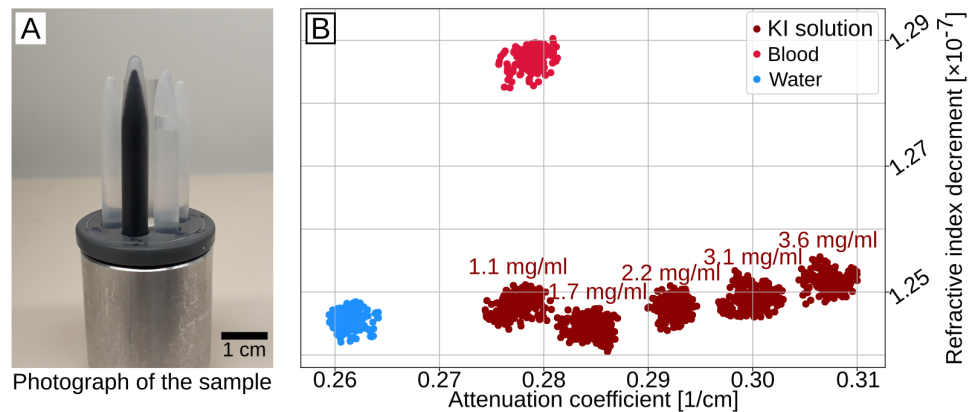


Figure 4.27: Attenuation coefficients and refractive index decrements of a test phantom. (A) The test sample consists of five increasing iodine concentrations and a blood coagulum mounted on a cylindrical sample holder. For the measurement, the sample was immersed into a plane parallel water container. (B) The attenuation coefficients increase with increasing iodine concentration. The iodine concentrations determined in a separate measurement at the MuCLS are indicated above the respective data. The attenuation values of blood and 1.1 mg/ml iodine solution overlap fully along the attenuation coefficient axis, while the refractive index decrements are separated by more than 28 standard deviations.

The blood sample shows a mean HU value of 66.6 and can therefore not be differentiated from the lowest iodine concentration ($\text{CNR}_{\text{blood/iodine}} = 0.7$).

The phase-contrast image is transformed to phase Hounsfield units and displayed in a window of $[-10; 80]$ HU_p in Fig. 4.28B. The iodine solutions (1.6, -1.1, 1.4, 2.4, 4.6 HU_p) show no clear visual contrast to the surrounding water (0.0 HU) but a very clear contrast to the blood sample (33.2 HU_p) with a CNR value of $\text{CNR}_{\text{blood/iodine}} = 19.0$.

The quantitative map of iodine concentrations as obtained from two-material decomposition is displayed in Fig. 4.28C. The mean iodine content in the marked regions (15×15 pixel) is (1.2 ± 0.1) mg/ml, (1.8 ± 0.1) mg/ml, (2.2 ± 0.1) mg/ml, (2.6 ± 0.1) mg/ml and (3.0 ± 0.1) mg/ml for the iodine filled tubes and (0.1 ± 0.1) mg/ml for the blood filled tube with the respective standard deviation given as a statistical error. The mean deviation from the values measured at the MuCLS is $|\overline{\Delta c}| = 0.3$ mg/ml.

Three material decomposition for stroke diagnose Fig. 4.29 demonstrates the potential of grating-based phase-contrast CT for advanced assessment of brain tissue. Subfigure A shows the conventional attenuation in a window of $[0; 200]$ HU. The mean HU values measured within the three plastic tubes are 151.7 HU, 152.2 HU and 130.5 HU from left to right. The CNR value between iodine and blood of $\text{CNR}_{\text{blood/iodine}} = 0.9$ confirms the visual impression that these materials can not be

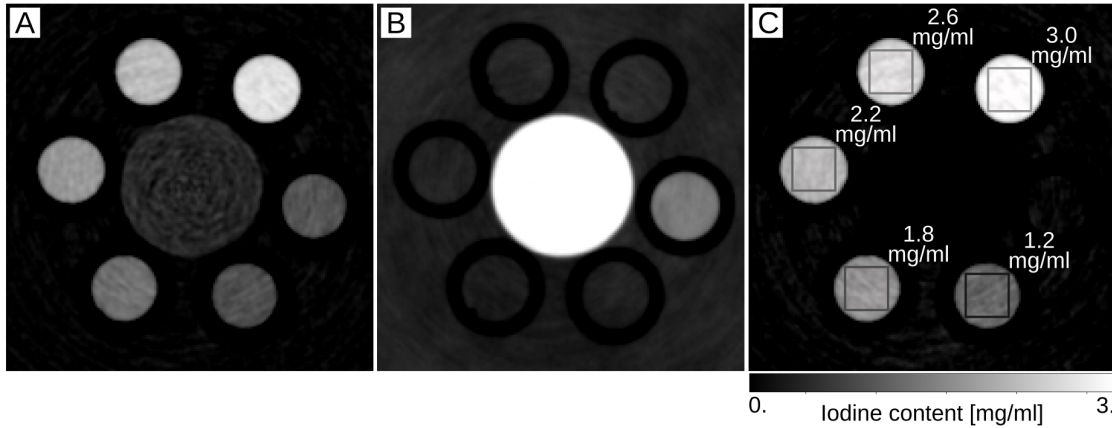


Figure 4.28: Polychromatic three-material decomposition. (A) Conventional attenuation displayed in Hounsfield units ($[0; 200]$ HU). Increasing amounts of contrast agent present with increasing HU values. The blood sample can not be differentiated from the lowest contrast agent concentration. (B) Refractive index decrement image displayed in phase Hounsfield units ($[-10; 80]$ HUp). The iodine concentrations present with similar Hounsfield units as the surrounding water and the signal is not dependent on the concentration. The blood sample exhibits a clearly higher HUp value and can unambiguously be differentiated from the iodine solutions. (C) Quantitative iodine image as obtained from two-material decomposition. The respective iodine concentration value is given next to each solution. The values deviate from the determined ground truth values with a mean deviation of $|\overline{\Delta c}| = 0.3$ mg/ml.

differentiated in the conventional HU image. The brain parenchyma shows slight contrast to the background in the way that the boundary line between the gyri and the surrounding formaldehyde solution can slightly be seen (see white arrows in the figure). The phase-contrast image is displayed in HUp values ($[-10; 95]$ HUp) in Fig. 4.29B. From left to right the HUp values in the plastic tubes are 4.2, 3.3, 157.8. The CNR between iodine and blood is $\text{CNR}_{\text{blood/iodine}} = 20.3$, they can be clearly differentiated due to the difference of their electron densities ($\rho_e(\text{blood}) = (3.86 \pm 0.02) \cdot 10^{29} \text{ m}^{-3}$, $\rho_e(\text{iodine}) = (3.35 \pm 0.01) \cdot 10^{29} \text{ m}^{-3}$). Also the brain parenchyma shows a significantly improved image contrast such that gray and white matter can be differentiated (see dark gray arrows in the figure). In the sulci on top and on the right of the displayed sectional plain of the sample, small regions with higher electron density are visible, which could be blood vessels with remaining blood residues.

The effective atomic number is displayed in pseudo colors (Fig. 4.29C) as in clinical dual-energy CT. The quantitative iodine content is displayed in Fig. 4.29D as obtained from three-material decomposition. Within the plastic tubes, the iodine concentrations are (2.1 ± 0.3) , mg/ml (2.2 ± 0.2) mg/ml, (0.0 ± 0.0) mg/ml from left to right.

The dark-field signal strength in terms of the third basis material (hydroxyapatite) is displayed in Fig. 4.29E as a heat map. The dark-field signal is typically enhanced at subresolutional electron-density fluctuations as can especially be seen at the borders of the blood filled tube. At the border of the tube in the middle, a clear signal enhancement is present. Comparison with the other image representations reveals a corresponding hyperdensity in the conventional attenuation image at the same position but with smaller extent and an increased electron density (increased HU_p value, respectively). However, in the iodine content image, there is an iodine-free vacancy at the corresponding position such that it can unambiguously be identified as the hydroxyapatite cluster. A further dark-field feature can be seen within the blood sample. It has no equivalent signal in the attenuation image but can be seen in the phase-contrast image in another gray-level windowing. As the tube contains only the coagulated blood, it is assumed, that the signal corresponds to a very dense agglomeration of blood cells originating from the coagulation process.

A direct comparison of two- and three-material decomposition from the same measurement is presented in Fig. 4.30. Decomposition of the original image into the water and iodine content based on the attenuation and phase signal alone leads to insufficient material separation. The hydroxyapatite cluster falsely appears in the iodine content image (Fig. 4.30A, white arrows). Additional consideration of the dark-field signal allows a clear identification and separation of the hydroxyapatite cluster which is not present in the iodine content image after three-material decomposition (Fig. 4.30B, white arrows). Both, two- and three-material decomposition allow the clear separation of iodine contrast agent and the blood coagulum. Three material decomposition yields a slightly lower iodine concentration value in the upper plastic tube. In total, grating-based phase contrast CT allows the separation of three materials with similar Hounsfield units with a single CT acquisition.

Discussion

The presented experiments demonstrate that quantitative material decomposition is possible at conventional polychromatic X-ray sources with Talbot-Lau interferometers and with higher X-ray energies compared to the previous experiments described in Sec. 4.5.3. It has been demonstrated how the additional information on the electron density and the microstructure of a material can be used for three-material discrimination in an experimentally simulated stroke sample.

At a polychromatic X-ray tube setup, the accuracy of iodine concentration determination in a calibration phantom has been evaluated. The accuracy of the determination of the absolute amount of iodine in this small sample is with a mean deviation of 0.3 mg/ml similar to commercially available dual-energy CT devices

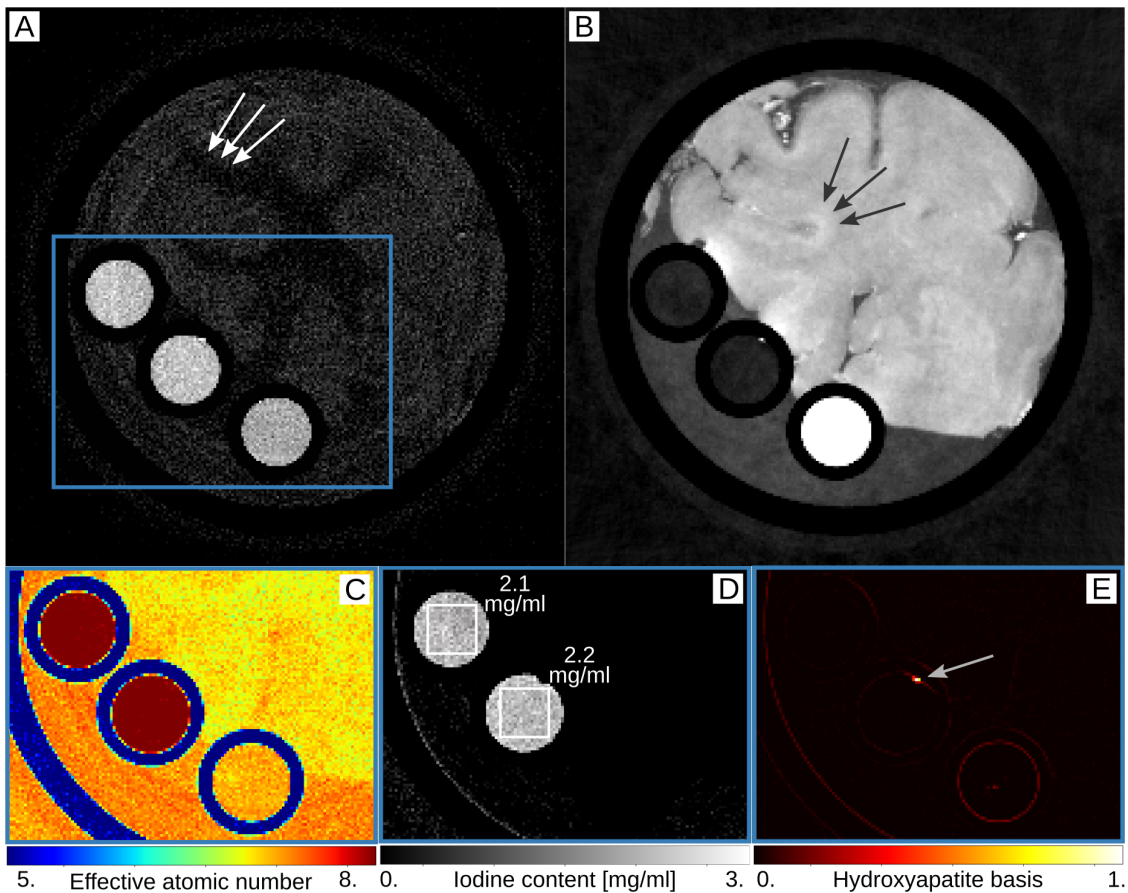


Figure 4.29: Advanced brain tissue assessment with a single grating-based CT acquisition. (A) Conventional attenuation displayed in Hounsfield units ($[0; 200]$ HU). Three hyperdense regions present with almost identical HU values. (B) Phase-contrast image displayed in phase Hounsfield units ($[-10; 95]$ HU). The clotted blood has a higher electron density than brain tissue and contrast agent and can clearly be identified. (C) Effective atomic number map is displayed in pseudo colors as usual in clinical dual-energy CT. (D) Quantitative iodine content image as obtained from three-material decomposition. The tube in the middle exhibits an iodine free vacancy at the tube border. (E) Dark-field image displayed in a heat map in terms of the normalized hydroxyapatite basis vector. The bright spot corresponds to the position of the iodine free vacancy in the iodine map which allows for an unambiguous identification of the calcification.

[Pelgrim et al., 2017, Koonce et al., 2014, Sellerer et al., 2018]. The relative deviation for the smallest concentrations is up to 17% compared to the ground truth values determined at the MuCLS. Comparison with the original nominal solutions reveals a smaller mean deviation of 0.2 mg/ml. The iodine solutions have been prepared directly before the measurement at setups B and C but the time to the full completion of all experiments was more than seven weeks. Thus, it can not be excluded that some concentrations have increased due to evaporation between the measurements. However, it has been seen in a previous study that the hygroscopic effect of iodine leads to a systematic overestimation of the nominal concentrations

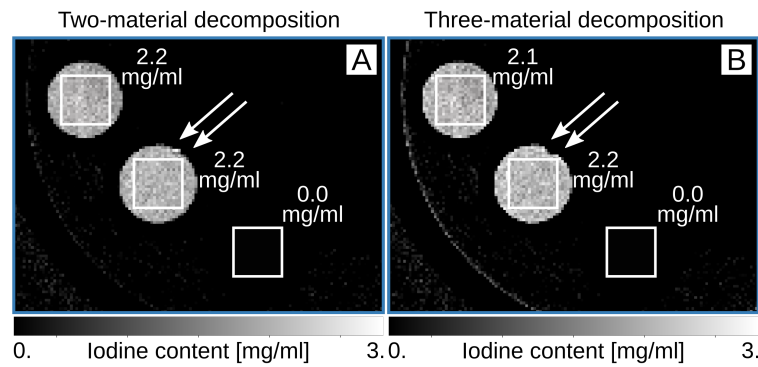


Figure 4.30: Comparison of material separation in two- and three-material decomposition. (A) The iodine content image reveals the quantitative amount of iodine in the two plastic tubes and allows a clear separation of contrast agent and the blood coagulum. The separation of contrast agent and the calcification is not possible by two-material decomposition, as the hydroxyapatite cluster is present in the iodine content image (marked by the white arrows). (B) Three material decomposition based on the attenuation, phase and dark-field signals, allows the clear separation of contrast agent, the blood coagulum and the hydroxyapatite cluster. The calcification (white arrows) and the blood coagulum (lowest white box) are correctly separated from the iodine content image. The outer blue box marks the respective enlarged region in Fig. 4.29A

[Braig et al., 2018b]. Therefore, the accuracy of the iodine quantification cannot be stated conclusively and should be analyzed with a well-defined iodine calibration phantom in the future.

With the experimental simulation of an unclear stroke scenario with a brain sample, a blood coagulum, contrast agent and a small hydroxyapatite calcification a potential clinical application has been demonstrated. While blood and contrast agent cannot be discriminated in the conventional attenuation image, the additional electron density based image allows the clear identification of the two materials. Further, the availability of the dark-field information allows the identification of calcifications. Quantitative three-material decomposition has been performed, such that the quantitative amount of iodine and the presence of hydroxyapatite clusters can be analyzed in separate basis images, which has the potential to simplify and clarify diagnosis. All these information can be extracted from a single CT acquisition without specific requirements for the X-ray source or the X-ray detector. This implies a potential concept for simplifying post-interventional stroke diagnosis which is up to now based on several follow-up investigations in clinical routine.

While the approach of grating-based material decomposition has successfully been transferred from a quasi-monochromatic X-ray source with a mean energy of ≈ 25 keV to polychromatic X-ray sources with mean energies of up to 43 keV, further steps are necessary to achieve clinical feasibility. In principle, the technical feasibility to mount the interferometer on a rotating CT gantry [Tapfer et al., 2012], the

decrease of the scanning time by the use of advanced acquisition schemes [Marschner et al., 2016a, von Teuffenbach et al., 2017], the reduction of the radiographic dose level to clinically approved values [Gromann et al., 2017b, Willer et al., 2018, Fingerle et al., 2019], in-vivo imaging for small animals as well as for pigs [Bech et al., 2013, Hellbach et al., 2015, Yaroshenko et al., 2015, Gromann et al., 2017b] and the increase of the X-ray energy and the field of view for applications suitable for the human chest [Gromann et al., 2017b, Willer et al., 2018, Fingerle et al., 2019, De Marco et al., 2019] have successfully been demonstrated within the last years. However, the combined fulfillment of all these requirements to enable clinical grating-based CT imaging remains an ambitious task. Apart from these technical challenges, the increase of the X-ray energy limits the complementarity of the attenuation and the phase-contrast image due to the decreasing contribution of photoelectric absorption to the X-ray attenuation. As the interaction cross section for photoelectric absorption scales with the atomic number of the material ($\sigma_{ph}(Z, E) \propto Z^k/E^l$, with $k \approx 4 - 5$ and $l \approx 3$ [White, 1977]), the material decomposition cannot be expected to work for soft-tissue materials like brain parenchyma at diagnostic X-ray energies for head CT. But the complementarity remains longer for higher atomic number materials like iodine contrast agent and calcifications. The high diagnostic relevance of these materials preserves the benefits of decomposition approaches at higher energies as exploited for clinical dual-energy CT.

On the other hand, the phase sensitivity that defines the smallest resolvable electron density difference will be substantially decreased for first interferometer designs suitable for humans [Chabior, 2011]. The phase sensitivity scales with a function of the period of the analyzer grating p_2 , the inter-grating distance d and the standard deviation of the photon statistics σ_ϕ such that the smallest resolvable refraction angle is $\alpha_{\min} = \sigma_\phi \cdot p_2 / 2\pi d$. In the brain sample measurement, the electron density difference between blood and contrast agent ($\Delta\rho_e > 0.335 \cdot 10^{29} \text{m}^{-3}$) was more than 22 times higher than the standard deviation in the electron density images $\sigma < 0.015 \cdot 10^{29} \text{m}^{-3}$ so that the discrimination would still be possible with moderately decreased phase sensitivity.

Unlike the attenuation coefficient and the electron density, the quantitative interpretation of the dark-field signal is still under discussion [Malecki et al., 2012, Strobl, 2014, Wolf et al., 2015]. It is possible to define a linear diffusion coefficient in analogy to the linear attenuation coefficient, which expresses the dark-field signal independent from the interferometer design [Bech et al., 2010]. However, the dark-field signal strength is dependent on the sub-micrometer structure of a material and is not an intrinsic chemical property in the same sense as the electron density or the atomic number. Therefore, the third basis vector is used for the extraction of the quantitative small-angle scattering power of a material as a novel type of

material specification. This can be an advantage in the diagnosis of all pathologies that involve microcalcifications or any type of strong refractive index fluctuations on a sub-resolution length scale (e.g. structural changes of the lung alveoli [Bech et al., 2013] or urate deposition [Scherer et al., 2015a] among others). As the signal also arises at material borders, strong electron density fluctuations or from strongly absorbing materials, radiologists must be trained on the interpretation of this novel signal and especially on drawing conclusions from correlations between the different image channels.

4.5.5 Conclusion

Within this thesis, various specific applications for grating-based X-ray imaging have been described or proposed. Other than most of these applications, the concept of grating-based material decomposition is not restricted to a specific pathology or organ system but offers a novel type of image processing available for all grating-based imaging applications. By that, the diagnostic information density generated with a single CT acquisition can be increased and grating-based imaging can provide similar information as dual-energy CT. Compared to dual-energy CT, the inherent registration of the images, the direct access to the electron density and most importantly, the availability of the dark-field image can provide particular diagnostic benefit. For the implementation of the method into the clinical routine the availability of the conventional attenuation image might be a further advantage as it doesn't have to be artificially generated from the high and low energy channels in dual-energy imaging.

While the above described experiments demonstrate the general feasibility of the approach at conventional X-ray tube sources with polychromatic X-ray spectra for clinically relevant in-vitro experiments, the used technology is not yet available for clinical imaging. The major challenges concern the stable implementation of a Talbot-Lau setup into the rotating gantry of a clinical CT system and the fabrication of gratings with a high aspect ratio covering the full field of view. However, the method itself is not restricted to CT imaging but could also be applied to radiography data by including a phase integration step. Together with the X-ray dark-field contrast agents, this is one of the more challenging but also very promising applications that would provide the improved diagnostic value of the combined attenuation, phase and dark-field images to a huge group of patients.

Chapter 5

Conclusion and outlook

In the last fifteen years, grating-based X-ray imaging has undergone rapid development in terms of technological progress as well as regarding the range of potential diagnostic applications. With the introduction of the combined Talbot-Lau interferometer, additional contrast modalities became available at conventional X-ray tube sources, which were until then restricted to large-scale synchrotron sources. It has been recognized within the early days that the improved soft-tissue contrast and the specific sensitivity to scattering by microcalcifications might be beneficial for mammography. While first studies demonstrated the improved diagnostic value of the three-fold image signal, the imaging parameters like dose, acquisition time and field-of-view were not compatible with clinical requirements. However, constant technological progress in grating fabrication, hardware components and the basic signal acquisition recently led to the first demonstration of a Talbot-Lau mammography system approved for clinical in-vivo imaging [Arboleda et al., 2020]. The scientific as well as the clinical community await the results of a first patient study with great excitement.

Also for the visualization of structural changes of lung tissue, the synchrotron community was very aware of the improved image contrast accessible through phase-retrieval methods. With the introduction of the Talbot-Lau interferometer, the dark-field signal additionally came into play. It has been recognized that the dark-field signal changes characteristically with specific pathological changes of the lung tissue. Major widespread diseases like COPD, pulmonary fibrosis, acute lung inflammation and pneumothorax among others change the interface between the alveoli and the surrounding air and thereby decrease the dark-field signal strength. In contrast to mammography, chest radiography requires higher X-ray energies and a large field of view. With conceptual changes of the interferometer design from table-top configuration to a swing-mode, the technique has as well reached a state where it could be approved for clinical imaging. The first results on a large scale

COPD study are expected to be published, soon [Willer, 2019].

Additional to these two big applications, which have reached the state of clinical approval, there are numerous further applications that have been demonstrated in preclinical experiments. While the diagnostic benefit could be demonstrated within preclinical ex-vivo or in-vitro experiments, the realization under clinically compatible boundary conditions can be challenging.

Within this thesis, two further applications have been proposed which are related to minor technical requirements due to the distant position of the relevant body parts.

It has been demonstrated that with grating-based radiography the simultaneous detection of metallic and wooden foreign body materials in the extremities is possible. While metallic particles are visible in conventional radiography, the additional dark-field signal allows the detection of wooden splinters even at a dose level where the metallic particles are not detectable in conventional radiography any more. The further clinical evaluation of grating-based foreign body detection could profit from the recent progress in mammography and lung imaging in form of the availability of approved Talbot-Lau radiography systems.

A further application concerning musculoskeletal imaging is the detection of the gout-related MSU crystal deposits in X-ray dark-field radiography. Here, we have presented a first proof that MSU crystals exhibit a strong dark-field signal in-vitro as well as in an experimental gout model with ex-vivo mice. Also in this case, the further clinical evaluation could profit from the availability of clinically approved Talbot-Lau systems. It is necessary to continue the investigation of the dark-field signal strength from MSU crystals in-situ and the detectable concentration limit to address early curable states of gout.

The timely clinical availability of these two applications could be beneficial for the concerned patients and also has the potential to simplify clinical workflow. The simultaneous development of a broad range of potential clinical applications can help to promote the method in the clinical community, but these applications might be less suitable to create serious attention in industry and related research fields.

The demonstration of a novel contrast agent for radiography and CT applications that can be applied to patients with renal dysfunction could cause a breakthrough for Talbot-Lau imaging. Microbubble-based ultrasound contrast agents are dealt as a potential candidate for a highly compatible X-ray dark-field contrast agent. In this work, the commercially available ultrasound contrast agents have been experimentally evaluated for their dark-field signal strength. It has been found that two of the three tested ultrasound contrast agents provide a clear dark-field signal. However, the in-vitro stability was not sufficient for further systematic tests or first preclinical demonstrations. Therefore, self-made PLGA spheres have been identified

as a potential candidate for further testing. They provide a high in-vitro stability and could be used for further systematic tests in regards to signal optimization. Especially the lower concentration limit that causes a significant dark-field signal must be evaluated with previously optimized microspheres in order to make a prediction on the clinical feasibility of this approach. In case of positive research results, the technique could directly be beneficial for a large group of patients and it could also push the further development of grating-based X-ray imaging and motivate further investments.

Additionally, it has been proposed, how the threefold image signal can be used for quantitative material decomposition from a single CT acquisition. Similar as in dual-energy CT imaging, the measured quantities can be interpreted as basis vectors spanning a vector system. By simple algebraic basis transformation, it is then possible to extract material specific information. This additional knowledge can be used for improved stroke diagnosis. Other than in commercially available dual-energy machines, the method is independent of the used detector system, the images are spatially perfectly registered and the diagnostically relevant electron density can directly be accessed. The most important advantage of the method is the availability of the dark-field signal which provides additional diagnostic information and can be used for three-material decomposition. By that it is not only possible to provide the same functions with Talbot-Lau CT as with dual-energy CT but there is additional information that cannot be provided by any other clinical imaging method. However, the technical realization of a grating-based CT system for dose relevant clinical imaging is still an ambitious task. While the single technological steps have been demonstrated individually in numerous experimental studies within the last years, the actual combined technical demonstration of such a CT system is still pending.

Recently, studies on the combination of phase-contrast imaging with dual-energy imaging or spectral imaging have started [Mechlem et al., 2019, 2020]. Especially the progress in the field of single photon-counting detectors with multiple energy bins can be beneficial for grating-based imaging. By that, it can be expected that the improved photon statistics will lead to a reduction of the required X-ray dose. But especially the possibility to separate different X-ray energies can help to suppress image artifacts and to further increase the amount of diagnostic information within a single image acquisition. Further progress can be expected in the field of advanced image processing and computer aided diagnosis for example in the form of machine-learning and neural networks. Finally, the concept of phase-stepping will probably be replaced by faster acquisition processes in clinical setups, as is already the case for the recently introduced clinical mammography and lung scanners based on different fringe scanning approaches.

Within the next years, the first results of the clinical studies at the clinically approved Talbot-Lau radiography systems will evaluate if the predicted diagnostic benefits are actually available within the clinical environment. In case of positive results, close interdisciplinary collaborations can identify further potential applications in the future to make the benefits available for as many patients as possible.

Bibliography

- J. Als-Nielsen and Des McMorrow. *Elements of modern X-ray physics*. John Wiley, Chichester, West Sussex, 2011. ISBN 978-0470973943. doi: 10.1002/9781119998365. URL <http://site.ebrary.com/lib/alltitles/docDetail.action?docID=10510633>.
- R. E. Alvarez. Estimator for photon counting energy selective x-ray imaging with multibin pulse height analysis. *Medical physics*, 38(5):2324–2334, 2011.
- R. E. Alvarez and A. Macovski. Energy-selective reconstructions in X-ray computerised tomography. *Physics in Medicine and Biology*, 21(5):733, 1976. doi: 10.1088/0031-9155/21/5/002. URL <http://stacks.iop.org/0031-9155/21/i=5/a=002>.
- M. A. Anderson, W. L. Newmeyer III, and E. S. Kilgore Jr. Diagnosis and treatment of retained foreign bodies in the hand. *The American Journal of Surgery*, 144(1): 63–67, 1982.
- J. Andrejewski. Characterization of a large field-of-view x-ray dark-field setup and energy resolved dark-field measurements. Master’s thesis, Technische Universität München, 2017.
- G. Anton, F. Bayer, M. W. Beckmann, J. Durst, P. A. Fasching, W. Haas, A. Hartmann, T. Michel, G. Pelzer, M. Radicke, et al. Grating-based darkfield imaging of human breast tissue. *Zeitschrift für Medizinische Physik*, 23(3):228–235, 2013.
- C. Arboleda, Z. Wang, T. Koehler, G. Martens, U. Van Stevendaal, M. Bartels, P. Villanueva-Perez, E. Roessl, and M. Stampanoni. Sensitivity-based optimization for the design of a grating interferometer for clinical x-ray phase contrast mammography. *Optics express*, 25(6):6349–6364, 2017.
- C. Arboleda, Z. Wang, K. Jefimovs, T. Koehler, U. Van Stevendaal, N. Kuhn, B. David, S. Prevrhal, K. Lång, S. Forte, et al. Towards clinical grating-interferometry mammography. *European radiology*, 30(3):1419–1425, 2020.

- F. Arfelli, R.-H. Menk, H.-J. Besch, L. Rigon, and H. Plathow-Besch. Contrast improvement with diffraction enhanced imaging for scattering materials. In *Proceedings IEEE International Symposium on Biomedical Imaging*, pages 133–136. IEEE, 2002.
- F. Arfelli, L. Rigon, R.-H. Menk, and H.-J. Besch. On the possibility of utilizing scattering-based contrast agents in combination with diffraction-enhanced imaging. In *Medical Imaging 2003: Physics of Medical Imaging*, volume 5030, pages 274–283. International Society for Optics and Photonics, 2003.
- F. Arfelli, L. Rigon, and R. Menk. Microbubbles as x-ray scattering contrast agents using analyzer-based imaging. *Physics in Medicine & Biology*, 55(6):1643, 2010.
- S. Auweter, J. Herzen, M. Willner, S. Grandl, K. Scherer, F. Bamberg, M. Reiser, F. Pfeiffer, and K. Hellerhoff. X-ray phase-contrast imaging of the breast—advances towards clinical implementation. *The British journal of radiology*, 87(1034):20130606, 2014.
- S. Bachche, M. Nonoguchi, K. Kato, M. Kageyama, T. Koike, M. Kuribayashi, and A. Momose. Laboratory-based x-ray phase-imaging scanner using talbot-lau interferometer for non-destructive testing. *Scientific Reports*, 7(1):1–7, 2017.
- A. N. Baer, T. Kurano, U. J. Thakur, G. K. Thawait, M. K. Fuld, J. W. Maynard, M. McAdams-DeMarco, E. K. Fishman, and J. A. Carrino. Dual-energy computed tomography has limited sensitivity for non-tophaceous gout: a comparison study with tophaceous gout. *BMC musculoskeletal disorders*, 17(1):91, 2016.
- R. Ballabriga, J. Alozy, M. Campbell, E. Frojdh, E. Heijne, T. Koenig, X. Llopart, J. Marchal, D. Pennicard, T. Poikela, et al. Review of hybrid pixel detector readout asics for spectroscopic x-ray imaging. *Journal of Instrumentation*, 11(01):P01007, 2016.
- T. Baum, E. Eggl, A. Malecki, F. Schaff, G. Potdevin, O. Gordijenko, E. G. Garcia, R. Burgkart, E. J. Rummeny, P. B. Noël, et al. X-ray dark-field vector radiography—a novel technique for osteoporosis imaging. *Journal of computer assisted tomography*, 39(2):286–289, 2015.
- M. Bech. *X-ray imaging with a grating-interferometer*. PhD thesis, University of Copenhagen, 5 2009.
- M. Bech, O. Bunk, T. Donath, R. Feidenhans, C. David, and F. Pfeiffer. Quantitative x-ray dark-field computed tomography. *Physics in Medicine & Biology*, 55(18):5529, 2010.

- M. Bech, A. Tapfer, A. Velroyen, A. Yaroshenko, B. Pauwels, J. Hostens, P. Bruyndonckx, A. Sasov, and F. Pfeiffer. In-vivo dark-field and phase-contrast x-ray imaging. *Scientific reports*, 3:3209, 2013.
- J. L. Becton and J. J. Christian. Foreign bodies in the hand in children. *Southern medical journal*, 70(2):147–149, 1977.
- R. Behling. *Modern Diagnostic X-Ray Sources: Technology, Manufacturing, Reliability*. CRC Press, 2015.
- R. Behling and F. Grüner. Diagnostic x-ray sources—present and future. *Nuclear Instruments and Methods in Physics Research Section A: Accelerators, Spectrometers, Detectors and Associated Equipment*, 878:50–57, 2018.
- L. Birnbacher. *High-sensitivity grating-based phase-contrast computed tomography with incoherent sources*. PhD thesis, Technical University of Munich, 7 2018.
- L. Birnbacher, M. Willner, A. Velroyen, M. Marschner, A. Hipp, J. Meiser, F. Koch, T. Schröter, D. Kunka, J. Mohr, et al. Experimental realisation of high-sensitivity laboratory x-ray grating-based phase-contrast computed tomography. *Scientific Reports*, 6:24022, 2016.
- L. Birnbacher, S. Maurer, K. Scheidt, J. Herzen, F. Pfeiffer, and T. Fromme. Electron density of adipose tissues determined by phase-contrast computed tomography provides a measure for mitochondrial density and fat content. *Frontiers in physiology*, 9:707, 2018a.
- L. Birnbacher, M. Willner, M. Marschner, D. Pfeiffer, F. Pfeiffer, and J. Herzen. Accurate effective atomic number determination with polychromatic grating-based phase-contrast computed tomography. *Opt. Express*, 26(12):15153–15166, 2018b. ISSN 10944087. doi: 10.1364/OE.26.015153. URL <http://www.opticsexpress.org/abstract.cfm?URI=oe-26-12-15153>.
- M. S. Bittencourt, B. Schmidt, M. Seltmann, G. Muschiol, D. Ropers, W. G. Daniel, and S. Achenbach. Iterative reconstruction in image space (iris) in cardiac computed tomography: initial experience. *The international journal of cardiovascular imaging*, 27(7):1081–1087, 2011.
- J. Boone and A. Chavez. Comparison of x-ray cross sections for diagnostic and therapeutic medical physics. *Medical Physics*, 23(12):1997–2005, 1996. doi: 10.1118/1.597899.
- E.-M. Braig, L. Birnbacher, F. Schaff, L. Gromann, A. Fingerle, J. Herzen, E. Rummeny, P. Noël, F. Pfeiffer, and D. Muenzel. Simultaneous wood and metal particle

- detection on dark-field radiography. *European radiology experimental*, 2(1):1–7, 2018a.
- E.-M. Braig, J. Böhm, M. Dierolf, C. Jud, B. Günther, K. Mechlem, S. Allner, T. Sellerer, K. Achterhold, B. Gleich, et al. Direct quantitative material decomposition employing grating-based x-ray phase-contrast ct. *Scientific reports*, 8(1):16394, 2018b.
- E.-M. Braig, D. Pfeiffer, M. Willner, T. Sellerer, K. Taphorn, C. Petrich, J. Scholz, L. Birnbacher, L. M. Petzold, M. Dierolf, et al. Single spectrum three-material decomposition with grating-based x-ray phase-contrast ct. *Physics in Medicine & Biology*, 2020a.
- E.-M. Braig, N. Roiser, M. A. Kimm, M. Busse, J. Andrejewski, J. Scholz, C. Petrich, A. Gustschin, A. Sauter, J. Bodden, et al. X-ray dark-field radiography: Potential for visualization of monosodium urate deposition. *Investigative Radiology*, 2020b.
- M. Braunagel, L. Birnbacher, M. Willner, M. Marschner, F. De Marco, M. Viermetz, S. Notohamiprodjo, K. Hellbach, S. Auweter, V. Link, et al. Qualitative and quantitative imaging evaluation of renal cell carcinoma subtypes with grating-based x-ray phase-contrast ct. *Scientific Reports*, 7(1):1–11, 2017.
- A. Bravin, P. Coan, and P. Suortti. X-ray phase-contrast imaging: from pre-clinical applications towards clinics. *Physics in Medicine & Biology*, 58(1):R1, 2012.
- P. W. Bray, J. L. Mahoney, and J. P. Campbell. Sensitivity and specificity of ultrasound in the diagnosis of foreign bodies in the hand. *The Journal of hand surgery*, 20(4):661–666, 1995.
- B. Brendel, M. von Teuffenbach, P. B. Noël, F. Pfeiffer, and T. Koehler. Penalized maximum likelihood reconstruction for x-ray differential phase-contrast tomography. *Medical physics*, 43(1):188–194, 2016.
- M. Broeders, S. Moss, L. Nyström, S. Njor, H. Jonsson, E. Paap, N. Massat, S. Duffy, E. Lynge, and E. Paci. The impact of mammographic screening on breast cancer mortality in europe: a review of observational studies. *Journal of medical screening*, 19(1_suppl):14–25, 2012.
- M. Brüggemann. Leitlinie der bundesärztekammer zur qualitätssicherung in der computertomographie. https://www.bundesaerztekammer.de/fileadmin/user_upload/downloads/LeitCT2007Korr-1.pdf, 2007a. Accessed: 2020-27-03.

- M. Brüggemann. Leitlinie der bundesärztekammer zur qualitätssicherung in der röntgendiagnostik. https://www.bundesaerztekammer.de/fileadmin/user_upload/downloads/LeitRoentgen2008Korr2.pdf, 2007b. Accessed: 2020-27-03.
- Bundesamt für Strahlenschutz. Wichtige Grenzwerte und typische Dosiswerte im Vergleich. <https://www.bfs.de/DE/themen/ion/strahlenschutz/grenzwerte/grenzwerte.html>, 2007a. Accessed: 2020-27-03.
- Bundesamt für Strahlenschutz. Qualitätssicherungs-richtlinie (qs-rl). Technical report, Referat Bundesaufsicht, 2007b.
- T. M. Buzug. Computed tomography. In *Springer Handbook of Medical Technology*, pages 311–342. Springer, 2011.
- E. Castelli, F. Arfelli, D. Dreossi, R. Longo, T. Rokvic, M. A. Cova, E. Quaia, M. Tonutti, F. Zanconati, A. Abrami, et al. Clinical mammography at the symep beam line. *Nuclear Instruments and Methods in Physics Research Section A: Accelerators, Spectrometers, Detectors and Associated Equipment*, 572(1):237–240, 2007.
- E. Castelli, M. Tonutti, F. Arfelli, R. Longo, E. Quaia, L. Rigon, D. Sanabor, F. Zanconati, D. Dreossi, A. Abrami, et al. Mammography with synchrotron radiation: first clinical experience with phase-detection technique. *Radiology*, 259(3):684–694, 2011.
- M. Chabior. *Contributions to the characterization of grating-based X-ray phase-contrast imaging*. PhD thesis, Technical University of Munich, 9 2011.
- S. N. Christiansen, M. Østergaard, and L. Terslev. Ultrasonography in gout: utility in diagnosis and monitoring. *Clin Exp Rheumatol*, 36(114):S61–S67, 2018.
- P. Coan, F. Bamberg, P. C. Diemoz, A. Bravin, K. Timpert, E. Mützel, J. G. Raya, S. Adam-Neumair, M. F. Reiser, and C. Glaser. Characterization of osteoarthritic and normal human patella cartilage by computed tomography x-ray phase-contrast imaging: a feasibility study. *Investigative radiology*, 45(7):437–444, 2010.
- P. Coan, A. Bravin, and G. Tromba. Phase-contrast x-ray imaging of the breast: recent developments towards clinics. *Journal of Physics D: Applied Physics*, 46(49):494007, 2013.
- D. Cosgrove. Ultrasound contrast agents: an overview. *European journal of radiology*, 60(3):324–330, 2006.

- J. Davis, B. Czerniski, A. Au, S. Adhikari, I. Farrell, and J. M. Fields. Diagnostic accuracy of ultrasonography in retained soft tissue foreign bodies: a systematic review and meta-analysis. *Academic Emergency Medicine*, 22(7):777–787, 2015.
- F. De Marco, K. Willer, L. B. Gromann, J. Andrejewski, K. Hellbach, A. Bähr, M. Dmochewitz, T. Koehler, H.-I. Maack, F. Pfeiffer, et al. Contrast-to-noise ratios and thickness-normalized, ventilation-dependent signal levels in dark-field and conventional in vivo thorax radiographs of two pigs. *PloS one*, 14(6), 2019.
- A. M. den Harder, M. J. Willeminck, Q. M. de Ruyter, A. M. Schilham, G. P. Krestin, T. Leiner, P. A. de Jong, and R. P. Budde. Achievable dose reduction using iterative reconstruction for chest computed tomography: a systematic review. *European journal of radiology*, 84(11):2307–2313, 2015.
- T. Djurdjevic, R. Rehwald, M. Knoflach, B. Matosevic, S. Kiechl, E. R. Gizewski, B. Glodny, and A. E. Grams. Prediction of infarction development after endovascular stroke therapy with dual-energy computed tomography. *European radiology*, 27(3):907–917, 2017.
- M. Doherty, T. L. Jansen, G. Nuki, E. Pascual, F. Perez-Ruiz, L. Punzi, A. K. So, and T. Bardin. Gout: why is this curable disease so seldom cured? *Annals of the rheumatic diseases*, 71(11):1765–1770, 2012.
- T. Donath, F. Pfeiffer, O. Bunk, C. Grünzweig, E. Hempel, S. Popescu, P. Vock, and C. David. Toward clinical x-ray phase-contrast ct: demonstration of enhanced soft-tissue contrast in human specimen. *Investigative radiology*, 45(7):445–452, 2010.
- D. Dreossi, A. Bergamaschi, B. Schmitt, E. Vallazza, F. Arfelli, R. Longo, R. Menk, L. Rigon, T. Rokvic, C. Venanzi, et al. Clinical mammography at the symep beam line: Toward the digital detection system. *Nuclear Instruments and Methods in Physics Research Section A: Accelerators, Spectrometers, Detectors and Associated Equipment*, 576(1):160–163, 2007.
- Drugbank. Drugbank perflutren. <https://www.drugbank.ca/drugs/DB00556>, 2020. Accessed: 2020-20-02.
- N. Dubey, R. Bakshi, M. Wasay, and J. Dmochowski. Early computed tomography hypodensity predicts hemorrhage after intravenous tissue plasminogen activator in acute ischemic stroke. *Journal of neuroimaging*, 11(2):184–188, 2001.
- I. F. Dunn, D. H. Kim, P. A. Rubin, R. Blinder, J. Gates, and A. J. Golby. Orbitocranial wooden foreign body: a pre-, intra-, and postoperative chronicle: case report. *Neurosurgery*, 65(2):E383–E384, 2009.

- A. Ebrahimi, M. Radmanesh, S. Rabiei, et al. Surgical removal of neglected soft tissue foreign bodies by needle-guided technique. *Iranian journal of otorhinolaryngology*, 25(70):29, 2013.
- E. Ettl, A. Malecki, F. Schaff, G. Potdevin, P. B. Noël, J. S. Bauer, O. Gordijenko, E. Grande García, R. Burgkart, E. J. Rummeny, et al. Prediction of vertebral failure load by using x-ray vector radiographic imaging. *Radiology*, 275(2):553–561, 2015a.
- E. Ettl, S. Schleede, M. Bech, K. Achterhold, R. Loewen, R. D. Ruth, and F. Pfeiffer. X-ray phase-contrast tomography with a compact laser-driven synchrotron source. *Proceedings of the National Academy of Sciences*, 112(18):5567–5572, 2015b.
- E. Ettl, M. Dierolf, K. Achterhold, C. Jud, B. Günther, E. Braig, B. Gleich, and F. Pfeiffer. The Munich Compact Light Source: Initial performance measures. *Journal of Synchrotron Radiation*, 23, 2016. ISSN 16005775 09090495. doi: 10.1107/S160057751600967X.
- E. Ettl, S. Grandl, A. Sztrókay-Gaul, M. Dierolf, C. Jud, L. Heck, K. Burger, B. Günther, K. Achterhold, D. Mayr, et al. Dose-compatible grating-based phase-contrast mammography on mastectomy specimens using a compact synchrotron source. *Scientific reports*, 8(1):1–10, 2018.
- S. Ehn, T. Sellerer, K. Mechlem, A. Fehring, M. Epple, J. Herzen, F. Pfeiffer, and P. Noël. Basis material decomposition in spectral ct using a semi-empirical, polychromatic adaption of the beer–lambert model. *Phys Med Biol*, 62:N1–N17, 2017a.
- S. Ehn, T. Sellerer, D. Muenzel, A. A. Fingerle, F. Kopp, M. Duda, K. Mei, B. Renger, J. Herzen, J. Dangelmaier, B. J. Schwaiger, A. Sauter, I. Riederer, M. Renz, R. Braren, E. J. Rummeny, F. Pfeiffer, and P. B. Noël. Assessment of quantification accuracy and image quality of a full-body dual-layer spectral CT system. *Journal of Applied Clinical Medical Physics*, 42(7):204–217, 2017b. ISSN 15269914. doi: 10.1002/acm2.12243. URL <http://doi.wiley.com/10.1002/acm2.12243>.
- H. Einarsdóttir, M. J. Emerson, L. H. Clemmensen, K. Scherer, K. Willer, M. Bech, R. Larsen, B. K. Ersbøll, and F. Pfeiffer. Novelty detection of foreign objects in food using multi-modal x-ray imaging. *Food Control*, 67:39–47, 2016.
- M. Elad and M. Aharon. Image denoising via sparse and redundant representations over learned dictionaries in wavelet domain. *Proceedings of the 5th International*

- Conference on Image and Graphics, ICIG 2009*, 15(12):754–758, 2010. ISSN 10577149. doi: 10.1109/ICIG.2009.101.
- EMA. European public assessment report, summary of product characteristics sonovue. https://www.ema.europa.eu/en/documents/product-information/sonovue-epar-product-information_de.pdf, 11 2007. Accessed: 2020-20-02.
- EMA. European public assessment report, summary of product characteristics optison. https://www.ema.europa.eu/en/documents/product-information/optison-epar-product-information_en.pdf, 08 2008. Accessed: 2020-20-02.
- EMA. European public assessment report, summary of product characteristics luminity. https://www.ema.europa.eu/en/documents/product-information/luminity-epar-product-information_en.pdf, 09 2009. Accessed: 2020-20-02.
- T. Endo, S. Ichihara, S. Moritani, M. Ooiwa, M. Shiraiwa, T. Morita, Y. Sato, J. Kiyohara, and S. Nagatsuka. Development of new imaging system based on grating interferometry: Preclinical study in breast imaging. In *International Workshop on Digital Mammography*, pages 488–493. Springer, 2014.
- K. J. Engel, D. Geller, T. Köhler, G. Martens, S. Schusser, G. Vogtmeier, and E. Rössl. Contrast-to-noise in x-ray differential phase contrast imaging. *Nuclear Instruments and Methods in Physics Research Section A: Accelerators, Spectrometers, Detectors and Associated Equipment*, 648:S202–S207, 2011.
- M. Engelhardt, C. KOTTLER, O. BUNK, C. DAVID, C. Schroer, J. Baumann, M. SCHUSTER, and F. PFEIFFER. The fractional talbot effect in differential x-ray phase-contrast imaging for extended and polychromatic x-ray sources. *Journal of microscopy*, 232(1):145–157, 2008.
- F. Epple, G. Potdevin, P. Thibault, S. Ehn, J. Herzen, A. Hipp, F. Beckmann, and F. Pfeiffer. Unwrapping differential x-ray phase-contrast images through phase estimation from multiple energy data. *Optics express*, 21(24):29101–29108, 2013.
- S. Faby, S. Kuchenbecker, S. Sawall, D. Simons, H.-p. Schlemmer, M. Lell, M. Kachelrieß, S. Faby, S. Kuchenbecker, and S. Sawall. Performance of today’s dual energy CT and future multi energy CT in virtual non-contrast imaging and in iodine quantification : A simulation study. *Medical physics*, 4349, 2015. doi: 10.1118/1.4922654. URL <http://dx.doi.org/10.1118/1.4922654>.
- A. A. Fingerle, F. De Marco, J. Andrejewski, K. Willer, L. B. Gromann, W. Noichl, F. Kriner, F. Fischer, C. Braun, H.-I. Maack, et al. Imaging features in post-mortem x-ray dark-field chest radiographs and correlation with conventional x-ray and ct. *European radiology experimental*, 3(1):25, 2019.

- G. Gennaro. Clinical mammographic and tomosynthesis units. *Handbook of X-ray Imaging: Physics and Technology*, page 457, 2017.
- F. J. Gilbert, R. Campbell, and A. Bayliss. The role of ultrasound in the detection of non-radiopaque foreign bodies. *Clinical radiology*, 41(2):109–112, 1990.
- S. Gkoumas, P. Villanueva-Perez, Z. Wang, L. Romano, M. Abis, and M. Stambanoni. A generalized quantitative interpretation of dark-field contrast for highly concentrated microsphere suspensions. *Scientific reports*, 6:35259, 2016.
- I. A. f. R. o. C. GLOBOCAN. Cancer fact sheets: breast. <http://gco.iarc.fr/today/data/factsheets/cancers/20-Breast-fact-sheet.pdf>, 03 2019. Accessed: 2020-06-04.
- S. Grandl, M. Willner, J. Herzen, A. Sztrókay-Gaul, D. Mayr, S. D. Auweter, A. Hipp, L. Birnbacher, M. Marschner, M. Chabior, et al. Visualizing typical features of breast fibroadenomas using phase-contrast ct: an ex-vivo study. *PLoS one*, 9(5), 2014.
- S. Grandl, K. Scherer, A. Sztrókay-Gaul, L. Birnbacher, K. Willer, M. Chabior, J. Herzen, D. Mayr, S. D. Auweter, F. Pfeiffer, et al. Improved visualization of breast cancer features in multifocal carcinoma using phase-contrast and dark-field mammography: an ex vivo study. *European radiology*, 25(12):3659–3668, 2015.
- GratXray. Gratxray-home. <https://www.gratxray.com/>, 2017. Accessed: 2020-03-07.
- T. G. Grobe, H. Dörning, and F. W. Schwartz. Barmer gek arztreport 2011. *Schriftreihe zur Gesundheitsanalyse*, 6, 2011.
- L. Gromann. *Development of a large-animal X-ray dark-field scanner*. PhD thesis, Technische Universität München, 2017.
- L. B. Gromann, F. De Marco, K. Willer, P. B. Noël, K. Scherer, B. Renger, B. Gleich, K. Achterhold, A. A. Fingerle, D. Muenzel, S. Auweter, K. Hellbach, M. Reiser, A. Baehr, M. Dmochewitz, T. J. Schroeter, F. J. Koch, P. Meyer, D. Kunka, J. Mohr, A. Yaroshenko, H. I. Maack, T. Pralow, H. Van Der Heijden, R. Proksa, T. Koehler, N. Wieberneit, K. Rindt, E. J. Rummeny, F. Pfeiffer, and J. Herzen. In-vivo X-ray dark-field chest radiography of a pig. *Scientific Reports*, 7(1):4807, 2017a. ISSN 20452322. doi: 10.1038/s41598-017-05101-w.
- L. B. Gromann, F. De Marco, K. Willer, P. B. Noël, K. Scherer, B. Renger, B. Gleich, K. Achterhold, A. A. Fingerle, D. Muenzel, et al. In-vivo x-ray dark-field chest radiography of a pig. *Scientific reports*, 7(1):4807, 2017b.

- A. Gücük and U. Üyetürk. Usefulness of hounsfield unit and density in the assessment and treatment of urinary stones. *World journal of nephrology*, 3(4):282, 2014.
- J.-P. Guigay. On fresnel diffraction by one-dimensional periodic objects, with application to structure determination of phase objects. *Optica Acta: International Journal of Optics*, 18(9):677–682, 1971.
- B. Günther, R. Gradl, C. Jud, E. Eggl, J. Huang, S. Kulpe, K. Achterhold, B. Gleich, M. Dierolf, and F. Pfeiffer. The versatile x-ray beamline of the munich compact light source: design, instrumentation and applications. *Journal of Synchrotron Radiation*, 27(5), 2020.
- R. Gupta, C. M. Phan, C. Leidecker, T. J. Brady, J. A. Hirsch, R. G. Nogueira, and A. J. Yoo. Evaluation of dual-energy ct for differentiating intracerebral hemorrhage from iodinated contrast material staining. *Radiology*, 257(1):205–211, 2010.
- G. W. Halaas. Management of foreign bodies in the skin. *American family physician*, 76(5), 2007.
- A. K. Hara, R. G. Paden, A. C. Silva, J. L. Kujak, H. J. Lawder, and W. Pavlicek. Iterative reconstruction technique for reducing body radiation dose at ct: feasibility study. *American Journal of Roentgenology*, 193(3):764–771, 2009.
- K. M. Hasebroock and N. J. Serkova. Toxicity of mri and ct contrast agents. *Expert opinion on drug metabolism & toxicology*, 5(4):403–416, 2009.
- C. Hauke, P. Bartl, M. Leghissa, L. Ritschl, S. Sutter, T. Weber, J. Zeidler, J. Freudenberger, T. Mertelmeier, M. Radicke, et al. A preclinical talbot–lau prototype for x-ray dark-field imaging of human-sized objects. *Medical physics*, 45(6):2565–2571, 2018.
- K. Hellbach, A. Yaroshenko, F. G. Meinel, A. Ö. Yildirim, T. M. Conlon, M. Bech, M. Mueller, A. Velroyen, M. Notohamiprodjo, F. Bamberg, et al. In vivo dark-field radiography for early diagnosis and staging of pulmonary emphysema. *Investigative radiology*, 50(7):430–435, 2015.
- K. Hellbach, A. Yaroshenko, K. Willer, T. Pritzke, A. Baumann, N. Hesse, S. Auweter, M. F. Reiser, O. Eickelberg, F. Pfeiffer, et al. Facilitated diagnosis of pneumothoraces in newborn mice using x-ray dark-field radiography. *Investigative radiology*, 51(10):597–601, 2016.

- K. Hellbach, A. Yaroshenko, K. Willer, T. M. Conlon, M. B. Braunagel, S. Auweter, A. Ö. Yildirim, O. Eickelberg, F. Pfeiffer, M. F. Reiser, et al. X-ray dark-field radiography facilitates the diagnosis of pulmonary fibrosis in a mouse model. *Scientific reports*, 7(1):340, 2017.
- K. Hellbach, A. Baehr, F. De Marco, K. Willer, L. B. Gromann, J. Herzen, M. Dmochewitz, S. Auweter, A. A. Fingerle, P. B. Noël, et al. Depiction of pneumothoraces in a large animal model using x-ray dark-field radiography. *Scientific reports*, 8(1):1–8, 2018a.
- K. Hellbach, F. G. Meinel, T. M. Conlon, K. Willer, A. Yaroshenko, A. Velroyen, M. Braunagel, S. Auweter, M. F. Reiser, O. Eickelberg, et al. X-ray dark-field imaging to depict acute lung inflammation in mice. *Scientific reports*, 8(1):2096, 2018b.
- K. Hellerhoff, L. Birnbacher, A. Sztrókay-Gaul, S. Grandl, S. Auweter, M. Willner, M. Marschner, D. Mayr, M. F. Reiser, F. Pfeiffer, et al. Assessment of intraductal carcinoma in situ (dcis) using grating-based x-ray phase-contrast ct at conventional x-ray sources: An experimental ex-vivo study. *Plos one*, 14(1):e0210291, 2019.
- B. Hemdal, L. Herrnsdorf, I. Andersson, G. Bengtsson, B. Heddson, and M. Olsson. Average glandular dose in routine mammography screening using a sectra microdose mammography unit. *Radiation protection dosimetry*, 114(1-3):436–443, 2005.
- J. Herzen, T. Donath, F. Pfeiffer, O. Bunk, C. Padeste, F. Beckmann, A. Schreyer, and C. David. Quantitative phase-contrast tomography of a liquid phantom using a conventional x-ray tube source. *Optics express*, 17(12):10010–10018, 2009.
- H. Hetterich, N. Webber, M. Willner, J. Herzen, L. Birnbacher, A. Hipp, M. Marschner, S. D. Auweter, C. Habbel, U. Schüller, et al. Aha classification of coronary and carotid atherosclerotic plaques by grating-based phase-contrast computed tomography. *European radiology*, 26(9):3223–3233, 2016.
- M. Hoheisel. Review of medical imaging with emphasis on x-ray detectors. *Nuclear Instruments and Methods in Physics Research Section A: Accelerators, Spectrometers, Detectors and Associated Equipment*, 563(1):215–224, 2006.
- S. B. Hooper, M. J. Kitchen, M. J. Wallace, N. Yagi, K. Uesugi, M. J. Morgan, C. Hall, K. K. Siu, I. M. Williams, M. Siew, et al. Imaging lung aeration and lung liquid clearance at birth. *The FASEB Journal*, 21(12):3329–3337, 2007.

- S. Hu, F. Yang, M. Griffa, R. Kaufmann, G. Anton, A. Maier, and C. Rieß. Towards quantification of kidney stones using x-ray dark-field tomography. In *2017 IEEE 14th International Symposium on Biomedical Imaging (ISBI 2017)*, pages 1112–1115. IEEE, 2017.
- Z. Huang and R. D. Ruth. Laser-electron storage ring. *Physical review letters*, 80(5):976, 1998.
- S. Hubbell, J.H.; Seltzer. Tables of x-ray mass attenuation coefficients and mass energy-absorption coefficients 1 keV to 20 meV for elements $z = 1$ to 92 and 48 additional substances of dosimetric interest. Technical report, National Inst. of Standards and Technology - PL, Gaithersburg, MD (United States). Ionizing Radiation Div., 1995.
- J. C. Hutter, H. Luu, P. M. Mehlhaff, A. L. Killam, and H. C. Dittrich. Physiologically based pharmacokinetic model for fluorocarbon elimination after the administration of an octafluoropropane-albumin microsphere sonographic contrast agent. *Journal of ultrasound in medicine*, 18(1):1–11, 1999.
- D. F. Jackson and D. J. Hawkes. X-ray attenuation coefficients of elements and mixtures. *Physics Reports*, 70(3):169–233, 1981.
- J. Jahns and A. W. Lohmann. The lau effect (a diffraction experiment with incoherent illumination). *Optics communications*, 28(3):263–267, 1979.
- R. W. James. *The Optical Principles of the Diffraction of X-rays*. G. Bell and Sons, 1954.
- T. H. Jensen, M. Bech, O. Bunk, T. Donath, C. David, R. Feidenhans, and F. Pfeiffer. Directional x-ray dark-field imaging. *Physics in Medicine & Biology*, 55(12):3317, 2010a.
- T. H. Jensen, M. Bech, I. Zanette, T. Weitkamp, C. David, H. Deyhle, S. Rutishauser, E. Reznikova, J. Mohr, R. Feidenhans, et al. Directional x-ray dark-field imaging of strongly ordered systems. *Physical Review B*, 82(21):214103, 2010b.
- I. Jerjen, V. Revol, P. Schuetz, C. Kottler, R. Kaufmann, T. Luethi, K. Jefimovs, C. Urban, and U. Sennhauser. Reduction of phase artifacts in differential phase contrast computed tomography. *Optics express*, 19(14):13604–13611, 2011.
- T. R. Johnson, B. Krauß, M. Sedlmair, M. Grasruck, H. Bruder, D. Morhard, C. Fink, S. Weckbach, M. Lenhard, B. Schmidt, T. Flohr, M. F. Reiser,

- and C. R. Becker. Material differentiation by dual energy CT: Initial experience. *European Radiology*, 17(6):1510–1517, 2007. ISSN 09387994. doi: 10.1007/s00330-006-0517-6.
- C. Jud. *X-ray Vector Radiography for Biomedical Applications*. PhD thesis, Technische Universität München, 2019.
- C. Jud, F. Schaff, I. Zanette, J. Wolf, A. Fehringer, and F. Pfeiffer. Dentinal tubules revealed with x-ray tensor tomography. *Dental materials*, 32(9):1189–1195, 2016.
- C. Jud, E.-M. Braig, M. Dierolf, E. Ettl, B. Günther, K. Achterhold, B. Gleich, E. Rummeny, P. Noël, F. Pfeiffer, et al. Trabecular bone anisotropy imaging with a compact laser-undulator synchrotron x-ray source. *Scientific reports*, 7(1):1–6, 2017.
- I. Jusué-Torres, S. S. Burks, C. G. Levine, R. G. Bhatia, R. Casiano, and R. Bullock. Wooden foreign body in the skull base: how did we miss it? *World neurosurgery*, 92:580–e5, 2016.
- A. C. Kak, M. Slaney, and G. Wang. Principles of computerized tomographic imaging, 2002.
- I. Kane, W. Whiteley, P. Sandercock, and J. Wardlaw. Availability of ct and mr for assessing patients with acute stroke. *Cerebrovascular Diseases*, 25(4):375–377, 2008.
- S. Kariya, A. Komemushi, M. Nakatani, R. Yoshida, S. Sawada, and N. Tanigawa. Co2 microbubble contrast enhancement in x-ray angiography. *Clinical radiology*, 68(4):346–351, 2013.
- J. Keyriläinen, A. Bravin, M. Fernández, M. Tenhunen, P. Virkkunen, and P. Suortti. Phase-contrast x-ray imaging of breast. *Acta radiologica*, 51(8):866–884, 2010.
- Y. Kim, Y. K. Kim, B. E. Lee, S. J. Lee, Y. J. Ryu, J. H. Lee, and J. H. Chang. Ultra-low-dose ct of the thorax using iterative reconstruction: evaluation of image quality and radiation dose reduction. *American Journal of Roentgenology*, 204(6):1197–1202, 2015.
- M. J. Kitchen, D. Paganin, R. A. Lewis, N. Yagi, K. Uesugi, and S. T. Mudie. On the origin of speckle in x-ray phase contrast images of lung tissue. *Physics in medicine & biology*, 49(18):4335, 2004.

- M. J. Kitchen, R. Lewis, N. Yagi, K. Uesugi, D. Paganin, S. B. Hooper, G. Adams, S. Jureczek, J. Singh, C. Christensen, et al. Phase contrast x-ray imaging of mice and rabbit lungs: a comparative study. *The British journal of radiology*, 78(935): 1018–1027, 2005.
- O. Klein and Y. Nishina. Über die streuung von strahlung durch freie elektronen nach der neuen relativistischen quantendynamik von dirac. *Zeitschrift für Physik*, 52(11-12):853–868, 1929.
- T. Koehler, H. Daerr, G. Martens, N. Kuhn, S. Löscher, U. Van Stevendaal, and E. Roessl. Slit-scanning differential x-ray phase-contrast mammography: Proof-of-concept experimental studies. *Medical Physics*, 42(4):1959–1965, 2015. ISSN 00942405. doi: 10.1118/1.4914420. URL <http://dx.doi.org/10.1118/1.4914420>.
- J. D. Koonce, R. Vliegthart, U. J. Schoepf, B. Schmidt, A. E. Wahlquist, P. J. Nietert, G. Bastarrika, T. G. Flohr, and F. G. Meinel. Accuracy of dual-energy computed tomography for the measurement of iodine concentration using cardiac ct protocols: validation in a phantom model. *European radiology*, 24(2):512–518, 2014.
- A. Korn, M. Fenchel, B. Bender, S. Danz, T. Hauser, D. Ketelsen, T. Flohr, C. Claussen, M. Heuschmid, U. Ernemann, et al. Iterative reconstruction in head ct: image quality of routine and low-dose protocols in comparison with standard filtered back-projection. *American journal of neuroradiology*, 33(2): 218–224, 2012.
- E. Kotter and M. Langer. Digital radiography with large-area flat-panel detectors. *European radiology*, 12(10):2562–2570, 2002.
- S. Kudo and T. Takei. Computed tomography settings for optimal detection of wooden foreign bodies. *The American journal of emergency medicine*, 34(11): 2237–2238, 2016.
- R. L. Lammers. Soft tissue foreign bodies. *Annals of emergency medicine*, 17(12): 1336–1347, 1988.
- D. B. Larson, L. W. Johnson, B. M. Schnell, S. R. Salisbury, and H. P. Forman. National trends in ct use in the emergency department: 1995–2007. *Radiology*, 258(1):164–173, 2011.
- E. Lau. Beugungserscheinungen an doppelrastern. *Annalen der Physik*, 437(7-8): 417–423, 1948.

- L. Lehmann, R. Alvarez, A. Macovski, W. Brody, N. Pelc, S. J. Riederer, and A. Hall. Generalized image combinations in dual kvp digital radiography. *Medical physics*, 8(5):659–667, 1981.
- M. R. Levine, S. M. Gorman, C. F. Young, and D. M. Courtney. Clinical characteristics and management of wound foreign bodies in the ed. *The American journal of emergency medicine*, 26(8):918–922, 2008.
- D. Lewis, A. Jivraj, P. Atkinson, and R. Jarman. My patient is injured: identifying foreign bodies with ultrasound. *Ultrasound*, 23(3):174–180, 2015.
- L. Li, Q. Wang, H. Li, M. Yuan, and M. Yuan. Preparation, characterization, in vitro release and degradation of cathelicidin-bf-30-plga microspheres. *PLoS One*, 9(6):e100809, 2014.
- J. N. Loeb. The influence of temperature on the solubility of monosodium urate. *Arthritis & Rheumatism: Official Journal of the American College of Rheumatology*, 15(2):189–192, 1972.
- R. Loewen. A compact light source: design and technical feasibility study of a laser-electron storage ring x-ray source. Technical report, Stanford Linear Accelerator Center, Menlo Park, CA (US), 2004.
- V. Ludwig, M. Seifert, T. Niepold, G. Pelzer, J. Rieger, J. Ziegler, T. Michel, and G. Anton. Non-destructive testing of archaeological findings by grating-based x-ray phase-contrast and dark-field imaging. *Journal of Imaging*, 4(4):58, 2018.
- V. Ludwig, M. Seifert, C. Hauke, K. Hellbach, F. Horn, G. Pelzer, M. Radicke, J. Rieger, S.-M. Sutter, T. Michel, et al. Exploration of different x-ray talbot-lau setups for dark-field lung imaging examined in a porcine lung. *Physics in Medicine & Biology*, 64(6):065013, 2019.
- S. K. Lynch, V. Pai, J. Auxier, A. F. Stein, E. E. Bennett, C. K. Kemble, X. Xiao, W.-K. Lee, N. Y. Morgan, and H. H. Wen. Interpretation of dark-field contrast and particle-size selectivity in grating interferometers. *Applied optics*, 50(22):4310–4319, 2011.
- A. Malecki, G. Potdevin, and F. Pfeiffer. Quantitative wave-optical numerical analysis of the dark-field signal in grating-based x-ray interferometry. *EPL (Europhysics Letters)*, 99(4):48001, 2012.
- M. Marschner, M. Willner, G. Potdevin, A. Fehringer, P. Noël, F. Pfeiffer, and J. Herzen. Helical x-ray phase-contrast computed tomography without phase stepping. *Scientific reports*, 6:23953, 2016a.

- M. Marschner, M. Willner, G. Potdevin, A. Fehringer, P. B. Noël, F. Pfeiffer, and J. Herzen. Helical X-ray phase-contrast computed tomography without phase stepping. *Scientific Reports*, 6:23953, 2016b. ISSN 20452322. doi: 10.1038/srep23953. URL <http://dx.doi.org/10.1038/srep23953>.
- M. Marschner, L. Birnbacher, M. Willner, M. Chabior, J. Herzen, P. B. Noël, and F. Pfeiffer. Revising the lower statistical limit of x-ray grating-based phase-contrast computed tomography. *PloS one*, 12(9):e0184217, 2017.
- C. H. McCollough, S. Leng, L. Yu, and J. G. Fletcher. Dual- and multi-energy CT: Principles, technical approaches, and clinical applications. *Radiology*, 276(3):637–653, 2015a. ISSN 1527-1315. doi: 10.1148/radiol.2015142631. URL <http://pubs.rsna.org/doi/10.1148/radiol.2015142631>.
- C. H. McCollough, S. Leng, L. Yu, and J. G. Fletcher. Dual-and multi-energy ct: principles, technical approaches, and clinical applications. *Radiology*, 276(3): 637–653, 2015b.
- K. Mechlem, S. Allner, S. Ehn, K. Mei, E.-M. Braig, D. Münzel, F. Pfeiffer, and P. B. Noël. A post-processing algorithm for spectral CT material selective images using learned dictionaries. *Biomedical Physics & Engineering Express*, 3(2):025009, 2017. ISSN 2057-1976. doi: 10.1088/2057-1976/aa6045. URL <http://stacks.iop.org/2057-1976/3/i=2/a=025009?key=crossref.aad80be976f68495a7972244cd92a200>.
- K. Mechlem, T. Sellerer, S. Ehn, D. Münzel, E.-M. Braig, J. Herzen, P. B. Noël, and F. Pfeiffer. Spectral angiography material decomposition using an empirical forward model and a dictionary-based regularization. *IEEE transactions on medical imaging*, 37(10):2298–2309, 2018.
- K. Mechlem, T. Sellerer, M. Viermetz, J. Herzen, and F. Pfeiffer. Spectral differential phase contrast x-ray radiography. *IEEE transactions on medical imaging*, 39(3):578–587, 2019.
- K. Mechlem, T. Sellerer, M. Viermetz, J. Herzen, and F. Pfeiffer. A theoretical framework for comparing noise characteristics of spectral, differential phase-contrast and spectral differential phase-contrast x-ray imaging. *Physics in Medicine & Biology*, 65(6):065010, 2020.
- F. G. Meinel, F. Schwab, S. Schleede, M. Bech, J. Herzen, K. Achterhold, S. Auweter, F. Bamberg, A. Ö. Yildirim, A. Bohla, et al. Diagnosing and mapping pulmonary emphysema on x-ray projection images: incremental value of grating-based x-ray dark-field imaging. *PloS one*, 8(3), 2013a.

- F. G. Meinel, F. Schwab, A. Yaroshenko, A. Velroyen, M. Bech, K. Hellbach, J. Fuchs, T. Stiewe, A. Ö. Yildirim, F. Bamberg, et al. Lung tumors on multi-modal radiographs derived from grating-based x-ray imaging—a feasibility study. *Physica Medica*, 30(3):352–357, 2013b.
- F. G. Meinel, A. Yaroshenko, K. Hellbach, M. Bech, M. Müller, A. Velroyen, F. Bamberg, O. Eickelberg, K. Nikolaou, M. F. Reiser, et al. Improved diagnosis of pulmonary emphysema using in vivo dark-field radiography. *Investigative radiology*, 49(10):653–658, 2014.
- P. R. Mendonca, P. Lamb, and D. V. Sahani. A flexible method for multi-material decomposition of dual-energy CT images. *IEEE Transactions on Medical Imaging*, 33(1):99–116, 2014. ISSN 02780062. doi: 10.1109/TMI.2013.2281719.
- R. J. Meyer. *Natrium: Ergänzungsband, Lieferung 7. Halogenide Systeme. Lösungen*. Springer Berlin Heidelberg, 1972. doi: 10.1007/978-3-662-11947-1.
- T. Michel, J. Rieger, G. Anton, F. Bayer, M. W. Beckmann, J. Durst, P. A. Fasching, W. Haas, A. Hartmann, G. Pelzer, et al. On a dark-field signal generated by micrometer-sized calcifications in phase-contrast mammography. *Physics in Medicine & Biology*, 58(8):2713, 2013.
- D. L. Miglioretti, E. Johnson, A. Williams, R. T. Greenlee, S. Weinmann, L. I. Solberg, H. S. Feigelson, D. Roblin, M. J. Flynn, N. Vanneman, et al. The use of computed tomography in pediatrics and the associated radiation exposure and estimated cancer risk. *JAMA pediatrics*, 167(8):700–707, 2013.
- A. Mileto, L. S. Guimaraes, C. H. McCollough, J. G. Fletcher, and L. Yu. State of the art in abdominal ct: The limits of iterative reconstruction algorithms. *Radiology*, 293(3):491–503, 2019.
- T. Millard, M. Endrizzi, L. Rigon, F. Arfelli, R. Menk, J. Owen, E. Stride, and A. Olivo. Quantification of microbubble concentration through x-ray phase contrast imaging. *Applied Physics Letters*, 103(11):114105, 2013.
- T. Millard, M. Endrizzi, N. Everdell, L. Rigon, F. Arfelli, R. Menk, E. Stride, and A. Olivo. Evaluation of microbubble contrast agents for dynamic imaging with x-ray phase contrast. *Scientific reports*, 5:12509, 2015.
- E. A. Miller, T. A. White, B. S. McDonald, and A. Seifert. Phase contrast x-ray imaging signatures for security applications. *IEEE Transactions on Nuclear Science*, 60(1):416–422, 2013.

- M. Mokin, P. Kan, T. Kass-Hout, A. A. Abla, T. M. Dumont, K. V. Snyder, L. N. Hopkins, A. H. Siddiqui, and E. I. Levy. Intracerebral hemorrhage secondary to intravenous and endovascular intraarterial revascularization therapies in acute ischemic stroke: an update on risk factors, predictors, and management. *Neurosurgical focus*, 32(4):E2, 2012.
- A. Momose, W. Yashiro, K. Kido, J. Kiyohara, C. Makifuchi, T. Ito, S. Nagatsuka, C. Honda, D. Noda, T. Hattori, T. Endo, and J. Tanaka. X-ray phase imaging : from synchrotron to hospital Subject Areas :. *Philosophical Transactions of the Royal Society A*, 372(2010):20130023, 2014a. doi: 10.1098/rsta.2013.0023.
- A. Momose, W. Yashiro, K. Kido, J. Kiyohara, C. Makifuchi, T. Ito, S. Nagatsuka, C. Honda, D. Noda, T. Hattori, et al. X-ray phase imaging: from synchrotron to hospital. *Philosophical Transactions of the Royal Society A: Mathematical, Physical and Engineering Sciences*, 372(2010):20130023, 2014b.
- K. S. Morgan, K. K. W. Siu, and D. Paganin. The projection approximation and edge contrast for x-ray propagation-based phase contrast imaging of a cylindrical edge. *Optics Express*, 18(10):9865–9878, 2010.
- M. Nagashima, J. Tanaka, J. Kiyohara, C. Makifuchi, K. Kido, and A. Momose. Application of x-ray grating interferometry for the imaging of joint structures. *Anatomical science international*, 89(2):95–100, 2014.
- T. Neogi, T. L. T. A. Jansen, N. Dalbeth, J. Fransen, H. R. Schumacher, D. Berendsen, M. Brown, H. Choi, N. L. Edwards, H. J. Janssens, et al. 2015 gout classification criteria: an american college of rheumatology/european league against rheumatism collaborative initiative. *Arthritis & rheumatology*, 67(10):2557–2568, 2015.
- M. S. Nielsen, T. Lauridsen, L. B. Christensen, and R. Feidenhans. X-ray dark-field imaging for detection of foreign bodies in food. *Food Control*, 30(2):531–535, 2013.
- S. Notohamiprodjo, N. Webber, L. Birnbacher, M. Willner, M. Viermetz, J. Herzen, M. Marschner, D. Mayr, H. Bartsch, T. Saam, et al. Qualitative and quantitative evaluation of structural myocardial alterations by grating-based phase-contrast computed tomography. *Investigative radiology*, 53(1):26–34, 2018.
- V. Paefgen, D. Doleschel, and F. Kiessling. Evolution of contrast agents for ultrasound imaging and ultrasound-mediated drug delivery. *Frontiers in pharmacology*, 6:197, 2015.

- D. Paganin. *Coherent X-ray optics*. Oxford University Press on Demand, 2006.
- D. W. Parsons, K. Morgan, M. Donnelley, A. Fouras, J. Crosbie, I. Williams, R. C. Boucher, K. Uesugi, N. Yagi, and K. K. Siu. High-resolution visualization of airspace structures in intact mice via synchrotron phase-contrast x-ray imaging (pcxi). *Journal of Anatomy*, 213(2):217–227, 2008.
- T. Pascart and F. Lioté. Gout: state of the art after a decade of developments. *Rheumatology*, 58(1):27–44, 2018.
- J. J. Pasternak and E. E. Williamson. Clinical pharmacology, uses, and adverse reactions of iodinated contrast agents: a primer for the non-radiologist. In *Mayo Clinic Proceedings*, volume 87, pages 390–402. Elsevier, 2012.
- K. Paturski. I the self-imaging phenomenon and its applications. In *Progress in optics*, volume 27, pages 1–108. Elsevier, 1989.
- S. Payabvash, M. H. Qureshi, S. M. Khan, M. Khan, S. Majidi, S. Pawar, and A. I. Qureshi. Differentiating intraparenchymal hemorrhage from contrast extravasation on post-procedural noncontrast ct scan in acute ischemic stroke patients undergoing endovascular treatment. *Neuroradiology*, 56(9):737–744, 2014.
- N. J. Pelc. Recent and future directions in ct imaging. *Annals of biomedical engineering*, 42(2):260–268, 2014.
- G. J. Pelgrim, R. W. van Hamersvelt, M. J. Willeminck, B. T. Schmidt, T. Flohr, A. Schilham, J. Milles, M. Oudkerk, T. Leiner, and R. Vliegthart. Accuracy of iodine quantification using dual energy ct in latest generation dual source and dual layer ct. *European radiology*, 27(9):3904–3912, 2017.
- C. M. Perrin, M. A. Dobish, E. Van Keuren, and J. A. Swift. Monosodium urate monohydrate crystallization. *CrystEngComm*, 13(4):1111–1117, 2011.
- F. Pfeiffer, T. Weitkamp, O. Bunk, and C. David. Phase retrieval and differential phase-contrast imaging with low-brilliance X-ray sources. *Nature Physics*, 2(4):258–261, 2006a. ISSN 1745-2473. doi: 10.1038/nphys265. URL <http://www.nature.com/doifinder/10.1038/nphys265>.
- F. Pfeiffer, T. Weitkamp, O. Bunk, and C. David. Phase retrieval and differential phase-contrast imaging with low-brilliance x-ray sources. *Nature physics*, 2(4):258, 2006b.
- F. Pfeiffer, O. Bunk, C. Kottler, and C. David. Tomographic reconstruction of three-dimensional objects from hard X-ray differential phase contrast projection

- images. *Nuclear Instruments and Methods in Physics Research, Section A*, 580(2):925–928, 2007. ISSN 01689002. doi: 10.1016/j.nima.2007.06.104.
- F. Pfeiffer, J. Herzen, M. Willner, M. Chabior, S. Auweter, M. Reiser, and F. Bamberg. Grating-based x-ray phase contrast for biomedical imaging applications. *Zeitschrift für medizinische Physik*, 23(3):176–185, 2013.
- C. Phan, A. Yoo, J. Hirsch, R. Nogueira, and R. Gupta. Differentiation of hemorrhage from iodinated contrast in different intracranial compartments using dual-energy head ct. *American Journal of Neuroradiology*, 33(6):1088–1094, 2012.
- A. A. Postma, P. A. Hofman, A. A. Stadler, R. J. van Oostenbrugge, M. P. Tijssen, and J. E. Wildberger. Dual-energy CT of the brain and intracranial vessels. *AJR. American journal of roentgenology*, 199(5 Suppl):26–33, 2012. ISSN 15463141. doi: 10.2214/AJR.12.9115.
- G. Potdevin, A. Malecki, T. Biernath, M. Bech, T. H. Jensen, R. Feidenhans, I. Zanette, T. Weitkamp, J. Kenntner, J. Mohr, et al. X-ray vector radiography for bone micro-architecture diagnostics. *Physics in Medicine & Biology*, 57(11):3451, 2012.
- M. Pouliot, M. J. James, S. R. McColl, P. H. Naccache, and L. G. Cleland. Monosodium urate microcrystals induce cyclooxygenase-2 in human monocytes. *Blood*, 91(5):1769–1776, 1998.
- F. Prade. *Grating-based X-ray dark-field imaging - Theory and applications in materials research*. PhD thesis, Technical University of Munich, 1 2017.
- F. Prade, A. Yaroshenko, J. Herzen, and F. Pfeiffer. Short-range order in mesoscale systems probed by x-ray grating interferometry. *EPL (Europhysics Letters)*, 112(6):68002, 2016.
- F. Prade, F. Schaff, S. Senck, P. Meyer, J. Mohr, J. Kastner, and F. Pfeiffer. Non-destructive characterization of fiber orientation in short fiber reinforced polymer composites with x-ray vector radiography. *NDT & E International*, 86:65–72, 2017.
- Z. Qi, J. Zambelli, N. Bevins, and G.-H. Chen. Quantitative imaging of electron density and effective atomic number using phase contrast CT. *Physics in Medicine and Biology*, 55(9):2669–2677, 2010a. ISSN 0031-9155. doi: 10.1088/0031-9155/55/9/016. URL <http://stacks.iop.org/0031-9155/55/i=9/a=016?key=crossref.58176d71d60fd4460de09d7f2684fcbf>.

- Z. Qi, J. Zambelli, N. Bevins, and G.-H. Chen. Quantitative imaging of electron density and effective atomic number using phase contrast ct. *Physics in Medicine & Biology*, 55(9):2669, 2010b.
- E. Quaia. Microbubble ultrasound contrast agents: an update. *European radiology*, 17(8):1995–2008, 2007.
- A. Raichur, Y. Nakajima, Y. Nagaoka, T. Maekawa, and D. S. Kumar. Hollow polymeric (plga) nano capsules synthesized using solvent emulsion evaporation method for enhanced drug encapsulation and release efficiency. *Materials Research Express*, 1(4):045407, 2014.
- T. Rauch, J. Rieger, G. Pelzer, F. Horn, R. Erber, M. Wunderle, J. Emons, N. Nabieva, N. Fuhrich, T. Michel, et al. Discrimination analysis of breast calcifications using x-ray dark-field radiography. *Medical Physics*, 2020.
- R. Raupach and T. Flohr. Performance evaluation of x-ray differential phase contrast computed tomography (pct) with respect to medical imaging. *Medical physics*, 39(8):4761–4774, 2012.
- R. Raupach and T. G. Flohr. Analytical evaluation of the signal and noise propagation in x-ray differential phase-contrast computed tomography. *Physics in Medicine & Biology*, 56(7):2219, 2011.
- M. Reiser, F.-P. Kuhn, J. Debus, et al. *Duale reihe radiologie. Stuttgart, Deutschland: Georg Thieme Verlag KG*, 2011.
- V. Revol, C. Kottler, R. Kaufmann, U. Straumann, and C. Urban. Noise analysis of grating-based x-ray differential phase contrast imaging. *Review of Scientific Instruments*, 81(7):073709, 2010.
- P. Richette, M. Doherty, E. Pascual, V. Barskova, F. Becce, J. Castaneda, M. Coyfish, S. Guillo, T. Jansen, H. Janssens, et al. 2018 updated european league against rheumatism evidence-based recommendations for the diagnosis of gout. *Annals of the rheumatic diseases*, 79(1):31–38, 2020.
- V. Richter, M. S. Willner, J. Henningsen, L. Birnbacher, M. Marschner, J. Herzen, M. A. Kimm, P. B. Noël, E. J. Rummeny, F. Pfeiffer, et al. Ex vivo characterization of pathologic fluids with quantitative phase-contrast computed tomography. *European journal of radiology*, 86:99–104, 2017.
- J. Rieger, P. Meyer, F. Horn, G. Pelzer, T. Michel, J. Mohr, and G. Anton. Optimization procedure for a talbot-lau x-ray phase-contrast imaging system. *Journal of Instrumentation*, 12(04):P04018, 2017.

- A. Ritter, F. Bayer, J. Durst, K. Gödel, W. Haas, T. Michel, J. Rieger, T. Weber, L. Wucherer, and G. Anton. Simultaneous maximum-likelihood reconstruction for x-ray grating based phase-contrast tomography avoiding intermediate phase retrieval. *arXiv preprint arXiv:1307.7912*, 2013.
- G. Rodgers, G. Schulz, H. Deyhle, S. Marathe, C. Bikis, T. Weitkamp, and B. Müller. A quantitative correction for phase wrapping artifacts in hard x-ray grating interferometry. *Applied Physics Letters*, 113(9):093702, 2018.
- E. Roessl and R. Proksa. K-edge imaging in x-ray computed tomography using multi-bin photon counting detectors. *Physics in Medicine and Biology*, 52(15):4679–4696, 2007. doi: 10.1088/0031-9155/52/15/020.
- E. Roessl, H. Daerr, T. Koehler, G. Martens, and U. van Stevendaal. Clinical boundary conditions for grating-based differential phase-contrast mammography. *Philosophical Transactions of the Royal Society A: Mathematical, Physical and Engineering Sciences*, 372(2010):20130033, 2014.
- P. Russo. *Handbook of X-ray imaging: physics and technology*. CRC press, 2017.
- A. Sarapata, M. Willner, M. Walter, T. Duttchenhofer, K. Kaiser, P. Meyer, C. Braun, A. Fingerle, P. B. Noël, F. Pfeiffer, et al. Quantitative imaging using high-energy x-ray phase-contrast ct with a 70 kvp polychromatic x-ray spectrum. *Optics Express*, 23(1):523–535, 2015.
- A. P. Sauter, J. Andrejewski, F. De Marco, K. Willer, L. B. Gromann, W. Noichl, F. Kriner, F. Fischer, C. Braun, T. Koehler, et al. Optimization of tube voltage in x-ray dark-field chest radiography. *Scientific reports*, 9(1):1–9, 2019.
- F. Schaff. *Directional Small-Angle X-ray Scattering Computed Tomography*. PhD thesis, Technical University of Munich, 5 2017.
- F. Schaff, A. Malecki, G. Potdevin, E. Eggl, P. B. Noël, T. Baum, E. G. Garcia, J. S. Bauer, and F. Pfeiffer. Correlation of x-ray vector radiography to bone micro-architecture. *Scientific reports*, 4:3695, 2014.
- K. Scherer. *Grating-based X-ray phase-contrast mammography*. PhD thesis, Technische Universität München, 2015.
- K. Scherer, L. Birnbacher, M. Chabior, J. Herzen, D. Mayr, S. Grandl, A. Sztrókay-Gaul, K. Hellerhoff, F. Bamberg, and F. Pfeiffer. Bi-directional x-ray phase-contrast mammography. *PloS one*, 9(5), 2014.

- K. Scherer, E.-M. Braig, K. Willer, M. Willner, A. A. Fingerle, M. Chabior, J. Herzen, M. Eiber, B. Haller, M. Straub, et al. Non-invasive differentiation of kidney stone types using x-ray dark-field radiography. *Scientific reports*, 5(1):1–7, 2015a.
- K. Scherer, K. Willer, L. Gromann, L. Birnbacher, E.-M. Braig, S. Grandl, A. Sztrókay-Gaul, J. Herzen, D. Mayr, K. Hellerhoff, et al. Toward clinically compatible phase-contrast mammography. *PLoS one*, 10(6):e0130776, 2015b.
- K. Scherer, L. Birnbacher, K. Willer, M. Chabior, J. Herzen, and F. Pfeiffer. Correspondence: Quantitative evaluation of x-ray dark-field images for microcalcification analysis in mammography. *Nature communications*, 7(1):1–3, 2016a.
- K. Scherer, E.-M. Braig, S. Ehn, J. Schock, J. Wolf, L. Birnbacher, M. Chabior, J. Herzen, D. Mayr, S. Grandl, et al. Improved diagnostics by assessing the micromorphology of breast calcifications via x-ray dark-field radiography. *Scientific reports*, 6:36991, 2016b.
- K. Scherer, A. Yaroshenko, D. A. Bölükbas, L. B. Gromann, K. Hellbach, F. G. Meinel, M. Braunagel, J. von Berg, O. Eickelberg, M. F. Reiser, et al. X-ray dark-field radiography-in-vivo diagnosis of lung cancer in mice. *Scientific reports*, 7(1):402, 2017.
- D. Schlager, A. B. Sanders, D. Wiggins, and W. Boren. Ultrasound for the detection of foreign bodies. *Annals of emergency medicine*, 20(2):189–191, 1991.
- S. Schleede, F. G. Meinel, M. Bech, J. Herzen, K. Achterhold, G. Potdevin, A. Malecki, S. Adam-Neumair, S. F. Thieme, F. Bamberg, et al. Emphysema diagnosis using x-ray dark-field imaging at a laser-driven compact synchrotron light source. *Proceedings of the National Academy of Sciences*, 109(44):17880–17885, 2012.
- J. Schlomka, E. Roessl, R. Dorscheid, S. Dill, G. Martens, T. Istel, C. Bäumer, C. Herrmann, R. Steadman, G. Zeitler, et al. Experimental feasibility of multi-energy photon-counting k-edge imaging in pre-clinical computed tomography. *Physics in Medicine & Biology*, 53(15):4031, 2008.
- J. Scholz, L. Birnbacher, C. Petrich, M. Riedel, L. Heck, S. Gkoumas, T. Sellerer, K. Achterhold, and J. Herzen. Biomedical x-ray imaging with a gas photon-counting detector: A comparative study. *APL Photonics*, 5(10):106108, 2020.
- T. Schoonjans, A. Brunetti, B. Golosio, M. Sanchez del Rio, V. A. Solé, C. Ferrero, and L. Vincze. The xraylib library for X-ray–matter interactions. Recent

- developments. *Spectrochimica Acta Part B: Atomic Spectroscopy*, 66(11-12):776–784, 11 2011. ISSN 0584-8547. doi: 10.1016/J.SAB.2011.09.011. URL <https://www.sciencedirect.com/science/article/pii/S0584854711001984>.
- J. J. Schreiber, P. A. Anderson, H. G. Rosas, A. L. Buchholz, and A. G. Au. Hounsfield units for assessing bone mineral density and strength: a tool for osteoporosis management. *JBJS*, 93(11):1057–1063, 2011.
- F. Schwab, S. Schleede, D. Hahn, M. Bech, J. Herzen, S. Auweter, F. Bamberg, K. Achterhold, A. Yildirim, A. Bohla, et al. Comparison of contrast-to-noise ratios of transmission and dark-field signal in grating-based x-ray imaging for healthy murine lung tissue. *Zeitschrift für Medizinische Physik*, 23(3):236–242, 2013.
- M. Seifert, V. Ludwig, M. Gallersdörfer, C. Hauke, K. Hellbach, F. Horn, G. Pelzer, M. Radicke, J. Rieger, S.-M. Sutter, et al. Single-shot talbot-lau x-ray dark-field imaging of a porcine lung applying the moiré imaging approach. *Physics in Medicine & Biology*, 63(18):185010, 2018.
- M. Seifert, V. Ludwig, S. Kaeppler, F. Horn, P. Meyer, G. Pelzer, J. Rieger, D. Sand, T. Michel, J. Mohr, et al. Talbot-lau x-ray phase-contrast setup for fast scanning of large samples. *Scientific reports*, 9(1):1–11, 2019.
- T. SELLERER, P. B. Noël, M. Patino, A. Parakh, S. Ehn, S. Zeiter, J. A. Holz, J. Hammel, A. A. Fingerle, F. Pfeiffer, D. Maintz, E. J. Rummeny, D. Muenzel, and D. V. Sahani. Dual-energy CT : a phantom comparison of different platforms for abdominal imaging. *European Radiology*, 2018. ISSN 0938-7994. doi: <https://doi.org/10.1007/s00330-017-5238-5>.
- E. Shefer, A. Altman, R. Behling, R. Goshen, L. Gregorian, Y. Roterman, I. Uman, N. Wainer, Y. Yagil, and O. Zarchin. State of the art of ct detectors and sources: a literature review. *Current Radiology Reports*, 1(1):76–91, 2013.
- T. Shibata, S. Okubo, D. Iwai, J. Kiyohara, S. Nagatsuka, and Y. Kodera. Investigation of dependence on the object orientation in visibility-contrast imaging with the x-ray talbot-lau interferometer. In *International Workshop on Digital Mammography*, pages 482–487. Springer, 2014.
- S. Si-Mohamed, D. Bar-Ness, M. Sigovan, D. P. Cormode, P. Coulon, E. Coche, A. Vlassenbroek, G. Normand, L. Bousel, and P. Douek. Review of an initial experience with an experimental spectral photon-counting computed tomography system. *Nuclear Instruments and Methods in Physics Research Section A: Accelerators, Spectrometers, Detectors and Associated Equipment*, 873:27–35, 2017.

- J. Siewerdsen, A. Waese, D. Moseley, S. Richard, and D. Jaffray. Spektr: A computational tool for x-ray spectral analysis and imaging system optimization. *Medical physics*, 31(11):3057–3067, 2004.
- V. P. Singh, N. M. Badiger, and N. Kucuk. Determination of effective atomic numbers using different methods for some low- Z materials. *Journal of Nuclear Chemistry*, 2014:1–7, 2014. ISSN 2314-4955. doi: 10.1155/2014/725629. URL <http://www.hindawi.com/journals/jnc/2014/725629/>.
- S. Sirsi and M. Borden. Microbubble compositions, properties and biomedical applications. *Bubble Science, Engineering & Technology*, 1(1-2):3–17, 2009.
- M. Stampanoni, Z. Wang, T. Thüring, C. David, E. Roessl, M. Trippel, R. A. Kubik-Huch, G. Singer, M. K. Hohl, and N. Hauser. The first analysis and clinical evaluation of native breast tissue using differential phase-contrast mammography. *Investigative radiology*, 46(12):801–806, 2011.
- R. Steadman, C. Herrmann, O. Mühlens, D. G. Maeding, J. Colley, T. Firlit, R. Luhta, M. Chappo, B. Harwood, and D. Kosty. Chromaix: a high-rate energy-resolving photon-counting ASIC for spectral computed tomography. In *Medical Imaging 2010: Physics of Medical Imaging*, volume 7622, page 762220. International Society for Optics and Photonics, 2010.
- M. Strobl. General solution for quantitative dark-field contrast imaging with grating interferometers. *Scientific reports*, 4:7243, 2014.
- R. Sudol and B. Thompson. Lau effect: theory and experiment. *Applied optics*, 20(6):1107–1116, 1981.
- A. Sztrókay, J. Herzen, S. D. Auweter, S. Liebhardt, D. Mayr, M. Willner, D. Hahn, I. Zanette, T. Weitkamp, K. Hellerhoff, et al. Assessment of grating-based x-ray phase-contrast CT for differentiation of invasive ductal carcinoma and ductal carcinoma in situ in an experimental ex vivo set-up. *European radiology*, 23(2):381–387, 2013.
- K. Taguchi and J. S. Iwanczyk. Vision 20/20: Single photon counting x-ray detectors in medical imaging. *Medical physics*, 40(10), 2013.
- H. F. Talbot. Lxxvi. facts relating to optical science. no. iv. *The London, Edinburgh, and Dublin Philosophical Magazine and Journal of Science*, 9(56):401–407, 1836.
- J. Tanaka, M. Nagashima, K. Kido, Y. Hoshino, J. Kiyohara, C. Makifuchi, S. Nishino, S. Nagatsuka, and A. Momose. Cadaveric and in vivo human joint

- imaging based on differential phase contrast by x-ray talbot-lau interferometry. *Zeitschrift für medizinische Physik*, 23(3):222–227, 2013.
- R. Tang, Y. Xi, W.-M. Chai, Y. Wang, Y. Guan, G.-Y. Yang, H. Xie, and K.-M. Chen. Microbubble-based synchrotron radiation phase contrast imaging: basic study and angiography applications. *Physics in Medicine & Biology*, 56(12):3503, 2011.
- X. Tang and Y. Yang. X-ray differential phase contrast and dark-field computed tomography and radiography with microbubbles as contrast agent. In *2013 IEEE 10th International Symposium on Biomedical Imaging*, pages 1248–1251. IEEE, 2013.
- A. Tapfer, M. Bech, A. Velroyen, J. Meiser, J. Mohr, M. Walter, J. Schulz, B. Pauwels, P. Bruyndonckx, X. Liu, et al. Experimental results from a pre-clinical x-ray phase-contrast ct scanner. *Proceedings of the National Academy of Sciences*, 109(39):15691–15696, 2012.
- K. Taphorn. Evaluation of x-ray dark-field signal imaging ex-situ human lung specimens and structure size determination. Master’s thesis, Technische Universität München, 2018.
- R. Terkeltaub and N. Edwards. *Gout: Diagnosis and Management of Gouty Arthritis and Hyperuricemia*. Professional Communications, 2011. ISBN 9781932610703. URL <https://books.google.de/books?id=13G07HEVWkC>.
- S. F. Thieme, C. R. Becker, M. Hacker, K. Nikolaou, M. F. Reiser, and T. R. Johnson. Dual energy CT for the assessment of lung perfusion-Correlation to scintigraphy. *European Journal of Radiology*, 68(3):369–374, 2008. ISSN 0720048X. doi: 10.1016/j.ejrad.2008.07.031.
- T. Thüring, R. Guggenberger, H. Alkadhi, J. Hodler, M. Vich, Z. Wang, C. David, and M. Stambanoni. Human hand radiography using x-ray differential phase contrast combined with dark-field imaging. *Skeletal radiology*, 42(6):827–835, 2013.
- M. Tijssen, P. Hofman, A. Stadler, W. Van Zwam, R. De Graaf, R. Van Oostenbrugge, E. Klotz, J. Wildberger, and A. Postma. The role of dual energy ct in differentiating between brain haemorrhage and contrast medium after mechanical revascularisation in acute ischaemic stroke. *European radiology*, 24(4):834–840, 2014.

- M. Töpperwien, F. van der Meer, C. Stadelmann, and T. Salditt. Three-dimensional virtual histology of human cerebellum by x-ray phase-contrast tomography. *Proceedings of the National Academy of Sciences*, 115(27):6940–6945, 2018.
- I. Turkcuer, R. Atilla, H. Topacoglu, S. Yanturali, S. Kiyani, N. Kabakci, S. Bozkurt, and A. A. Cevik. Do we really need plain and soft-tissue radiographies to detect radiolucent foreign bodies in the ed? *The American journal of emergency medicine*, 24(7):763–768, 2006.
- A. Velroyen. *X-ray Phase-Contrast and Dark-Field Imaging of Small Animals: Contrast Enhancement and in vivo Imaging*. PhD thesis, Technical University of Munich, 1 2015.
- A. Velroyen, M. Bech, A. Malecki, A. Tapfer, A. Yaroshenko, M. Ingrisch, C. Cyran, S. Auweter, K. Nikolaou, M. Reiser, et al. Microbubbles as a scattering contrast agent for grating-based x-ray dark-field imaging. *Physics in Medicine & Biology*, 58(4):N37, 2013.
- A. Velroyen, M. Bech, A. Tapfer, A. Yaroshenko, M. Müller, P. Paprottka, M. Ingrisch, C. C. Cyran, S. D. Auweter, K. Nikolaou, et al. Ex vivo perfusion-simulation measurements of microbubbles as a scattering contrast agent for grating-based x-ray dark-field imaging. *PloS one*, 10(7), 2015.
- M. von Teuffenbach, T. Koehler, A. Fehringer, M. Viermetz, B. Brendel, J. Herzen, R. Proksa, E. J. Rummeny, F. Pfeiffer, and P. B. Noël. Grating-based phase-contrast and dark-field computed tomography: a single-shot method. *Scientific reports*, 7(1):7476, 2017.
- Z. Wang and B. Han. Advanced iterative algorithm for phase extraction of randomly phase-shifted interferograms. *Optics letters*, 29(14):1671–1673, 2004.
- Z. Wang, N. Hauser, G. Singer, M. Trippel, R. A. Kubik-Huch, C. W. Schneider, and M. Stampanoni. Non-invasive classification of microcalcifications with phase-contrast x-ray mammography. *Nature communications*, 5(1):1–9, 2014.
- Z. Wang, N. Hauser, G. Singer, M. Trippel, R. A. Kubik-Huch, C. W. Schneider, and M. Stampanoni. Correspondence: Reply to ‘quantitative evaluation of x-ray dark-field images for microcalcification analysis in mammography’. *Nature communications*, 7(1):1–3, 2016.
- Y. Watanabe, K. Uotani, T. Nakazawa, M. Higashi, N. Yamada, Y. Hori, S. Kan-zaki, T. Fukuda, T. Itoh, and H. Naito. Dual-energy direct bone removal CT angiography for evaluation of intracranial aneurysm or stenosis: Comparison

- with conventional digital subtraction angiography. *European Radiology*, 19(4):1019–1024, 2009. ISSN 09387994. doi: 10.1007/s00330-008-1213-5.
- W. R. Webb, W. E. Brant, and N. M. Major. *Fundamentals of Body CT E-Book*. Elsevier Health Sciences, 2019.
- T. Weber, P. Bartl, F. Bayer, J. Durst, W. Haas, T. Michel, A. Ritter, and G. Anton. Noise in x-ray grating-based phase-contrast imaging. *Medical physics*, 38(7):4133–4140, 2011.
- T. Weber, F. Bayer, W. Haas, G. Pelzer, J. Rieger, A. Ritter, L. Wucherer, J. M. Braun, J. Durst, T. Michel, et al. Investigation of the signature of lung tissue in x-ray grating-based phase-contrast imaging. *arXiv preprint arXiv:1212.5031*, 2012.
- T. Weitkamp, A. Diaz, C. David, F. Pfeiffer, M. Stampanoni, P. Cloetens, and E. Ziegler. X-ray phase imaging with a grating interferometer. *Optics express*, 13(16):6296–6304, 2005.
- D. White. An analysis of the z-dependence of photon and electron interactions. *Physics in Medicine & Biology*, 22(2):219, 1977.
- WHO. Fact-sheet top ten causes of death. <https://www.who.int/en/news-room/fact-sheets/detail/the-top-10-causes-of-death>, 2018. Accessed: 2020-17-07.
- WHO CVD. Fact-sheet cardiovascular diseases. [https://www.who.int/news-room/fact-sheets/detail/cardiovascular-diseases-\(cvds\)](https://www.who.int/news-room/fact-sheets/detail/cardiovascular-diseases-(cvds)), 2020. Accessed: 2020-27-05.
- M. J. Willemink and P. B. Noël. The evolution of image reconstruction for ct—from filtered back projection to artificial intelligence. *European radiology*, 29(5):2185–2195, 2019.
- M. J. Willemink, M. Persson, A. Pourmorteza, N. J. Pelc, and D. Fleischmann. Photon-counting ct: technical principles and clinical prospects. *Radiology*, 289(2):293–312, 2018.
- K. Willer. Performance of the first dark-field chest x-ray system for patients. https://www.xnpig2019.com/pdf/XNPIG2019Program_Poster.pdf, 2019. Accessed: 2020-31-08.
- K. Willer, A. A. Fingerle, L. B. Gromann, F. De Marco, J. Herzen, K. Achterhold, B. Gleich, D. Muenzel, K. Scherer, M. Renz, et al. X-ray dark-field imaging of the

- human lung—a feasibility study on a deceased body. *PloS one*, 13(9):e0204565, 2018.
- M. Willner, M. Bech, J. Herzen, I. Zanette, D. Hahn, J. Kenntner, J. Mohr, A. Rack, T. Weitkamp, and F. Pfeiffer. Quantitative X-ray phase-contrast computed tomography at 82 keV. *Optics Express*, 21(4):4155, 2013a. ISSN 1094-4087. doi: 10.1364/OE.21.004155. URL <https://www.osapublishing.org/oe/abstract.cfm?uri=oe-21-4-4155>.
- M. Willner, M. Bech, J. Herzen, I. Zanette, D. Hahn, J. Kenntner, J. Mohr, A. Rack, T. Weitkamp, and F. Pfeiffer. Quantitative x-ray phase-contrast computed tomography at 82 kev. *Optics express*, 21(4):4155–4166, 2013b.
- M. Willner, G. Fior, M. Marschner, L. Birnbacher, J. Schock, C. Braun, A. A. Fingerle, P. B. Noël, E. J. Rummeny, F. Pfeiffer, et al. Phase-contrast hounsfield units of fixated and non-fixated soft-tissue samples. *PloS one*, 10(8):e0137016, 2015.
- A. Winklehner, C. Karlo, G. Puipe, B. Schmidt, T. Flohr, R. Goetti, T. Pfammatter, T. Frauenfelder, and H. Alkadhi. Raw data-based iterative reconstruction in body cta: evaluation of radiation dose saving potential. *European radiology*, 21(12):2521–2526, 2011.
- J. Wolf, J. I. Sperl, F. Schaff, M. Schüttler, A. Yaroshenko, I. Zanette, J. Herzen, and F. Pfeiffer. Lens-term-and edge-effect in x-ray grating interferometry. *Biomedical optics express*, 6(12):4812–4824, 2015.
- D. Wu, M. D. Wong, K. Yang, A. Yan, Y. Li, L. Fajardo, B. Zheng, X. Wu, and H. Liu. Using microbubble as contrast agent for high-energy x-ray in-line phase contrast imaging: demonstration and comparison study. *IEEE Transactions on Biomedical Engineering*, 65(5):1117–1123, 2017.
- Y. Xi, R. Tang, Y. Wang, and J. Zhao. Microbubbles as contrast agent for in-line x-ray phase-contrast imaging. *Applied Physics Letters*, 99(1):011101, 2011.
- M. Yaffe and J. Rowlands. X-ray detectors for digital radiography. *Physics in Medicine & Biology*, 42(1):1, 1997.
- K. Yanagisawa, F. Moriyasu, T. Miyahara, M. Yuki, and H. Iijima. Phagocytosis of ultrasound contrast agent microbubbles by kupffer cells. *Ultrasound in medicine & biology*, 33(2):318–325, 2007.

- A. Yaroshenko, F. G. Meinel, M. Bech, A. Tapfer, A. Velroyen, S. Schleede, S. Auweter, A. Bohla, A. Ö. Yildirim, K. Nikolaou, et al. Pulmonary emphysema diagnosis with a preclinical small-animal x-ray dark-field scatter-contrast scanner. *Radiology*, 269(2):427–433, 2013.
- A. Yaroshenko, K. Hellbach, A. Ö. Yildirim, T. M. Conlon, I. E. Fernandez, M. Bech, A. Velroyen, F. G. Meinel, S. Auweter, M. Reiser, et al. Improved in vivo assessment of pulmonary fibrosis in mice using x-ray dark-field radiography. *Scientific reports*, 5:17492, 2015.
- A. Yaroshenko, T. Pritzke, M. Koschlig, N. Kamgari, K. Willer, L. Gromann, S. Auweter, K. Hellbach, M. Reiser, O. Eickelberg, et al. Visualization of neonatal lung injury associated with mechanical ventilation using x-ray dark-field radiography. *Scientific reports*, 6(1):1–8, 2016.
- W. Yashiro, Y. Terui, K. Kawabata, and A. Momose. On the origin of visibility contrast in x-ray talbot interferometry. *Optics express*, 18(16):16890–16901, 2010.
- H. Yoshioka, Y. Kadono, Y. T. Kim, H. Oda, T. Maruyama, Y. Akiyama, T. Mimura, J. Tanaka, M. Niitsu, Y. Hoshino, et al. imaging evaluation of the cartilage in rheumatoid arthritis patients with an x-ray phase imaging apparatus based on talbot-lau interferometry. *Scientific Reports*, 10(1):1–9, 2020.
- I. Zanette. *Interférométrie X à réseaux pour l'imagerie et l'analyse de front d'ondes au synchrotron*. PhD thesis, Université de Grenoble, 12 2011.
- R. Zhang, B. Qin, Y. Ge, B. Whiting, K. Li, F. Villanueva, and G.-H. Chen. Potential use of microbubbles (mbs) as contrast material in x-ray dark field (df) imaging: How does the df signal change with the characteristic parameters of the mbs? In *Medical Imaging 2016: Physics of Medical Imaging*, volume 9783, page 97830N. International Society for Optics and Photonics, 2016.
- S. Zhang and Y. Xia. Ct image reconstruction algorithms: A comprehensive survey. *Concurrency and Computation: Practice and Experience*, page e5506, 2019.

Appendix

A Propagation of electromagnetic waves

In the following, the equations and physical relations necessary for understanding the occurrence of the Talbot effect will be introduced. For a detailed description of X-ray optics please see [Paganin, 2006]. From the Maxwell equations, the d'Alembert wave equation for the electrical field can be derived

$$(\mu_0\epsilon_0\frac{\partial^2}{\partial t^2} - \nabla^2)\mathbf{E} = 0. \quad (5.1)$$

A solution for this equation is a wave propagating along the z-axis

$$\mathbf{E} = \mathbf{C}\cos(kz - \omega t + \phi), \quad (5.2)$$

with the wave vector k , the angular frequency $\omega = 2\pi\nu$ and the wave amplitude \mathbf{C} . By inserting Eq. 5.2 into the wave equation (Eq. 5.1) one can see that $\nu\lambda = \frac{1}{\sqrt{\mu_0\epsilon_0}}$ and thus $c = \frac{1}{\sqrt{\mu_0\epsilon_0}}$ which is the speed of light in vacuum. The variables x , y and z denote the usual Cartesian coordinate system. The wave vector \vec{k} has a magnitude of $k = 2\pi/\lambda$ and points into the direction of propagation. A number of approximations lead to the concept of a time independent scalar wave $\Psi(x, y, z)$, which is sufficient to describe the propagation of X-rays.

Fresnel diffraction integral We are considering free space propagation in the near-field regime (Fresnel regime). Based on the Huygens-Fresnel principle, a wave front can be considered as the superposition of spherical wavelets with each point on the wavefront being the source of a spherical wave. The wave front at a distant point can then be calculated by integration over all these wavelets as described by the Fresnel diffraction integral

$$\Psi(x, y, z) = \frac{e^{ikz}}{i\lambda z} \iint \Psi(x_0, y_0, 0) e^{\frac{ik}{2z}[(x-x_0)^2 + (y-y_0)^2]} dx_0 dy_0, \quad (5.3)$$

with x_0, y_0 being the x and y components in the plane $z = 0$. The Fresnel integral follows from the Kirchoff diffraction integral under the paraxial approximation, i.e. the assumption of small angular deviations of the plane wave components from the optical axis. By defining the propagator function

$$P_d = \frac{e^{ikd}}{i\lambda d} e^{ik(x^2+y^2)/2d}, \quad (5.4)$$

the Fresnel diffraction integral can be interpreted as a convolution of the wave function Ψ and the propagator to calculate the wavefront at position $z = d$. With this interpretation, the Fourier convolution theorem provides a simple solution for the task of wave propagation. As it states that a convolution in real space equals a simple multiplication in Fourier space, we can propagate a wave front by multiplication with the propagator function in Fourier space.

Fourier transform The two-dimensional Fourier transform $\hat{\Psi}$ of the wave function Ψ is given by

$$\hat{\Psi}(k_x, k_y) = \int \int \Psi_0(x, y) e^{-i(k_x x + k_y y)} dx dy. \quad (5.5)$$

And the respective inverse Fourier transform is

$$\Psi(x, y) = \frac{1}{(2\pi)^2} \int \int \hat{\Psi}_0(k_x, k_y) e^{i(k_x x + k_y y)} dk_x dk_y. \quad (5.6)$$

Refractive index Let's now consider a monochromatic plane wave propagating in z direction in vacuum. It can be described by

$$\Psi(\vec{r}) = E_0 e^{i\vec{k} \cdot \vec{r}} = E_0 e^{i\frac{2\pi}{\lambda} z} = E_0 e^{i\phi}, \quad (5.7)$$

with $\phi = 2\pi z/\lambda$ the constant phase in a plane perpendicular to the propagation direction. Let's now additionally consider an object consisting of a specific material with a thickness d in propagation direction. Compared to vacuum, the speed of light in this medium is $c_m < c$. This can be used to define the classical refractive index $n = c_m/c$. However, the full description of a propagating wave is possible by the complex refractive index

$$\mathbf{n} = 1 - \delta + i\beta, \quad (5.8)$$

with the real part describing the phase shifting properties of a material and the imaginary part describing its absorption under the projection approximation (see below). A wave propagating in z -direction through a medium with refractive index

n can then be expressed as

$$\Psi(z) = E_0 e^{ink_z z} = E_0 e^{ik_z z} e^{-ik_z z \delta} e^{-k_z z \beta}, \quad (5.9)$$

Paraxial approximation For a monochromatic wave, propagating in z direction, the z -component of the wave vector can explicitly be calculated such that

$$k_z = \sqrt{k^2 - k_x^2 - k_y^2}. \quad (5.10)$$

If $k_x^2 + k_y^2 \ll k^2$, i.e. for very small deflections from the z -direction, the expression for k_z can be simplified with the Taylor approximation for the square root

$$k_z = k \sqrt{1 - \frac{k_x^2}{k^2} - \frac{k_y^2}{k^2}} \approx k - \frac{k_x^2 + k_y^2}{2k}. \quad (5.11)$$

This is known as the paraxial approximation.

Projection approximation The projection approximation connects geometric optics with wave optics. It assumes that all scattering within an object can be described with the exit wave without substantial diffraction within the object. By that, transverse phase and intensity changes are imprinted at the nominal exit plane [Morgan et al., 2010].

Talbot effect Let's now consider a periodic wave-front with a period p . The Fourier transform of this function is discrete as only Fourier components with $k_x, k_y = 2\pi m/p$ are non-zero. In the simplified one-dimensional case, the Fourier space propagator is

$$\hat{P}_d(k_x = 2\pi m/p) = e^{ikd} e^{-ik_x^2/2k} = e^{ikd} e^{-i(2\pi m/p)^2/2k}. \quad (5.12)$$

At a specific distance $d' = 2p^2/\lambda$ the Fourier propagator shrinks down to

$$\hat{P}_{d'}(k_x = 2\pi m/p) = e^{ikd'} e^{-i\frac{\lambda}{4\pi} \frac{2p^2}{\lambda} \left(\frac{2\pi m}{p}\right)^2} = e^{ikd'} e^{-i2\pi m^2} = e^{ikd'}. \quad (5.13)$$

At those propagation distances d' the original wave front of the periodic wave function is recreated, which is often described as self image. This effect has first been described by Henry Talbot for optical light and absorption gratings. The distance $d' = d_T$ is therefore known as Talbot distance. As the self image is a perfect replication of the wavefront caused by the periodic object, a solely phase-shifting object will not create self images in that sense. However, it has been shown by Guigay et al. [Guigay, 1971] that the periodic phase modulation introduced by a mainly

phase shifting object will as well cause periodic intensity modulations at certain distances. These distances are fractions of the Talbot distances and are therefore called fractional Talbot distances. Here, we refer to [Zanette, 2011] for a more detailed derivation of the possible constellations and only give the (fractional) Talbot distances for the most commonly used grating types

$$d_{T,f} = \eta \frac{2p^2}{\lambda}, \quad \eta = \begin{cases} n & \text{for an absorption grating} \\ n/4 & \text{for a } \pi/2 \text{ phase grating} \\ n/16 & \text{for a } \pi \text{ phase grating,} \end{cases} \quad (5.14)$$

with n being the Talbot order. In case of π -shifting phase gratings, the self image has half the period of the grating.

B Measurement of the refraction angle

To understand the formation of phase-contrast by a sample we consider a plane monochromatic wave illuminating a homogeneous wedge with an opening angle of β (see Fig. 5.1). The optical path length through the object is then given by $T(x) = x \tan\alpha$. Over this path the wave travels with the reduced speed of light inside the medium according to its refractive index n

$$\Psi = E_0 e^{ik \int n(z) dz}. \quad (5.15)$$

The real part of the refractive index therefore describes the phase shift of the wave-front related to the optical path length through the medium, resulting in a linear phase gradient $d\phi/dx$ behind the wedge. As illustrated in Fig. 5.1, this phase gradient causes an angular deflection of the wave-front, which can be related to the phenomenon of refraction as known from geometrical optics. The resulting refraction angle α , by which the wave vector is deflected from its original direction, can be related to the phase gradient by the following geometrical consideration: the points P_1 and P_2 in Fig. 5.1 are chosen such that they represent positions with a phase difference of 2π and therefore a distance of one wavelength λ in the direction of the wave vector \vec{k}' . Thus, the distance P_1P_2 can be expressed as $P_1P_2 = \lambda/\sin\alpha$. The phase shift over this distance is 2π and therefore the linear phase gradient can be expressed as

$$\frac{1}{k} \left| \frac{d\phi}{dx} \right| = \sin\alpha \approx \alpha. \quad (5.16)$$

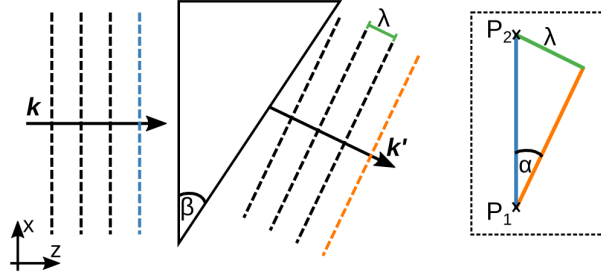


Figure 5.1: Refraction angle. If the wave front propagates through an object with a wedge-like form the X-rays are refracted by an angle α . The straight lines perpendicular to the wave vector k mark positions of equal phase of the incident electromagnetic wave. The points P_1 and P_2 mark positions with a distance of one wavelength λ in the direction of the wave vector \vec{k}' and thus a distance of $\frac{d\phi}{dx} = \frac{2\pi}{\lambda} \sin\alpha$ in x-direction.

where the last approximation is valid for small angles α . This angular deflection will cause a lateral displacement of the wavefront by

$$\Delta x = d \tan\alpha \approx d\alpha. \quad (5.17)$$

The considerations above are based on the chapter about refractive optical elements in [Paganin, 2006]. In a Talbot interferometer, an intensity modulation is imprinted onto the wavefront in form of the self image. By that, the lateral displacement of this intensity modulation can be measured. As the displacement is rather small for X-rays and clinically compatible interferometer configurations, the signal is acquired by stepping a further grating over one period p_2 of the intensity modulation. The resulting sinusoidal stepping curve will be laterally shifted by phase objects according to Eq. 5.17. This displacement is measured as a phase shift of the stepping curve relative to the reference curve without sample

$$\Delta\varphi = \frac{2\pi}{p_2} \Delta x. \quad (5.18)$$

With Eq. 2.7, 5.16 and 5.17 the measured phase-shift of the stepping curve can be related to the gradient of the refractive index decrement

$$\Delta\varphi = \frac{2\pi}{p_2} d\alpha = \frac{2\pi}{p_2} d \frac{1}{k} \left| \frac{d\phi}{dx} \right| = \frac{2\pi}{p_2} d \frac{d}{dx} \int \delta(x) dz. \quad (5.19)$$

C Computed tomography

In the following it will be briefly derived, how three-dimensional volume data can be reconstructed from a series of angular projections. For the purpose of X-ray imaging,

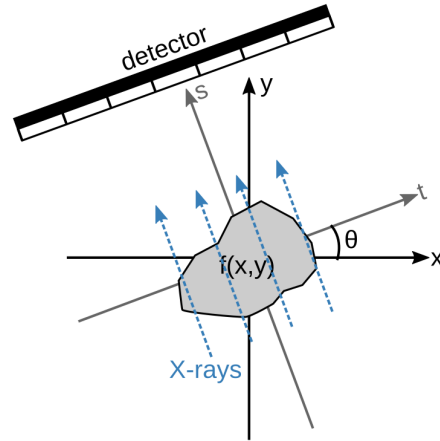


Figure 5.2: Rotated coordinate system in tomographic imaging. A function $f(x, y)$ describes the two-dimensional distribution of a measurable quantity. With computed tomography this function can be reconstructed from a set of projections onto the detector plane. The coordinate system (s, t) is rotating with the imaging system such that t is parallel to the detector lines and s is parallel to the projection lines with θ describing the rotation angle.

a two dimensional layer of an object can be described by the spatial distribution of its attenuation coefficients (or any other measurable material characteristic) with a function $f(x, y)$. If the object is placed in an X-ray imaging system consisting of an X-ray source and a detector, the detector will record the remaining X-ray intensity behind the object and therefore the attenuation caused by the object (Fig. 5.2). The X-ray intensity can hereby be calculated by the Beer-Lambert law, relating the signal strength to the line integral of the attenuation coefficients of the object along the beam path s

$$I = I_0 e^{-\int \mu(x,y) ds}. \quad (5.20)$$

The mathematical operation of projection $p_\theta(t)$ along a straight line $s = \text{const.}$ is described by the Radon transform \mathcal{R}

$$p_\theta(t) = \mathcal{R}_\theta(f(s, t)) = \int_{(\theta, t) \text{ line}} f(s, t) ds = \int_{-\infty}^{\infty} \int_{-\infty}^{\infty} f(x, y) \delta(x \cos \theta + y \sin \theta - t) dx dy, \quad (5.21)$$

with (t, s) the coordinate system rotated by an angle θ compared to the original coordinate system (x, y) . $t = x \cos \theta + y \sin \theta$ describes the projection line and $\delta(x)$ is the delta function. The key for the widely used filtered backprojection algorithm is the Fourier slice theorem which relates the measurable intensity projection with the original object function in Fourier space.

Fourier slice theorem The one-dimensional Fourier transform of a parallel projection $p_\theta(t)$

$$\hat{p}_\theta(\omega) = \int_{-\infty}^{\infty} p_\theta(t) e^{-2\pi i t \omega} dt, \quad (5.22)$$

equals a slice through the two dimensional Fourier transform of this function

$$\hat{f}(u, v)|_{slice} = \int_{-\infty}^{\infty} f(x, y) e^{-2\pi i(xu+yv)} dx dy = \int_{-\infty}^{\infty} f(x, y) e^{-2\pi i \omega(x \cos \theta + y \sin \theta)} dx dy, \quad (5.23)$$

at the spatial frequency $(u, v) = (\omega \cos \theta, \omega \sin \theta)$. In short

$$\hat{p}_\theta(\omega) = \hat{f}(\omega, \theta). \quad (5.24)$$

This implies that, in principle, the object function can be reconstructed from the projections by inverse Fourier transform. To sample all points in the (u, v) plane an infinite number of projection angles θ would be required. In practice, only a finite, discrete number of projections can be acquired and $\hat{f}(u, v)$ is only known along a finite number of straight lines in the frequency domain. However, as a digital image is discrete as well, the space is sampled sufficiently if the minimum number of projections fullfills the Nyquist theorem $N \geq \pi/2n_{px}$ with n_{px} the width of the reconstructed volume in detector pixels.

Filtered backprojection One possible implementation of the backtransformation of the Radon transform of the function $f(x, y)$ is the filtered backprojection

$$f(x, y) = \int_0^\pi \int_{-\infty}^{+\infty} |\omega| \hat{p}_\theta(\omega) e^{2\pi i \omega t} d\omega d\theta. \quad (5.25)$$

The term $|\omega|$ represents the spatial frequency filtration and is introduced when transforming the rectangular (u, v) coordinates to polar coordinates $(\omega \cos \theta, \omega \sin \theta)$. This step is a convolution with the frequency, i.e. frequencies are weighted proportional to their absolute value. Therefore, additional window functions are often used to suppress high frequency image noise.

Further details about tomographic reconstruction and the derivation of the above described equations can be found in [Kak et al., 2002, Buzug, 2011].

Reconstruction of differential data In grating-based CT imaging, not only the attenuation coefficient but also the gradient of the electron density is measured. In that case, the measured signal is the line integral of the first derivative of a

function $g(s, t)$ along the stepping direction

$$p_\theta(t) = \int_{(\theta,t)\text{line}} \frac{\partial}{\partial t} g(s, t) ds. \quad (5.26)$$

The original function can directly be reconstructed with an adaptation of the filter function in the FBP algorithm. The Fourier derivative theorem states that the Fourier transform of the derivative $f'(x)$ of a function $f(x)$ is given by

$$\hat{f}'(x) = 2\pi i x \hat{f}(x). \quad (5.27)$$

Therefore, the original function can be reconstructed by using the filter function

$$\hat{h}(\omega) = \frac{1}{2\pi i \cdot \text{sgn}(\omega)}, \quad (5.28)$$

with ω being the spatial frequency defined as above and sgn being the sign function. $\hat{h}(\omega)$ corresponds then to a ramp filter with an additional integration step. By that, the original function - here the refractive index decrement (or the electron density) - can be reconstructed.

D Basis transformation

Assume a three-dimensional vector space and a set of basis vectors $B = (\vec{b}_1, \vec{b}_2, \vec{b}_3)$ that spans this vector space. A basis is a set of linear independent vectors that allows to express the coordinates $\vec{p} = (p_x, p_y, p_z)$ of every point p in this vector space as a linear combination of those basis vectors in the form

$$v_1 \cdot \begin{pmatrix} b_{1,x} \\ b_{1,y} \\ b_{1,z} \end{pmatrix} + v_2 \cdot \begin{pmatrix} b_{2,x} \\ b_{2,y} \\ b_{2,z} \end{pmatrix} + v_3 \cdot \begin{pmatrix} b_{3,x} \\ b_{3,y} \\ b_{3,z} \end{pmatrix} = \begin{pmatrix} p_x \\ p_y \\ p_z \end{pmatrix}. \quad (5.29)$$

The coefficients v_1, v_2, v_3 can then be interpreted as the vector components of the vector \vec{v} in the basis B . For many applications it can be convenient to change from a given basis system into another one. In this work, this is the case for the transformation from the measured quantities linear attenuation coefficient μ , electron density ρ_e and dark-field signal strength df to a representation of the relative material contribution (m_i) so that $B = (\vec{\mu}, \vec{\rho}_e, \vec{df})$ and $\tilde{B} = (\vec{m}_1, \vec{m}_2, \vec{m}_3)$. The material contribution is the volume fraction of a specific material in this image voxel.

For basis systems of two- or three-dimensional vector spaces, linear algebra offers simple transformation algorithms that can be implemented with minor computational effort. In the following it is explained how the transformation matrix can be

found that transforms each image vector \vec{v} in the system of the measurement quantities (basis set B) to the respective vector \vec{w} in the material basis system (\tilde{B}). For example, the attenuation coefficient, the electron density and the dark-field signal strength in a voxel of the specific reconstructed volume form the components of the vector \vec{v} , the relative amount of iodine, water and calcium at this specific point form the components in the vector \vec{w} . To interchange between those two representations, we will derive the respective transformation matrix \mathbf{T} such that $\vec{v} = \mathbf{T} \cdot \vec{w}$.

We define the matrices \mathbf{B} and $\tilde{\mathbf{B}}$ which contain the basis vectors as columns such that

$$\mathbf{B} \cdot \vec{v} = \tilde{\mathbf{B}} \cdot \vec{w}, \quad (5.30)$$

$$\vec{v} = \mathbf{B}^{-1} \tilde{\mathbf{B}} \cdot \vec{w} = \mathbf{T} \cdot \vec{w}, \quad (5.31)$$

$$\mathbf{B}^{-1} \tilde{\mathbf{B}} = \mathbf{T}. \quad (5.32)$$

From here on, we describe, how the transformation matrix for specific basis materials can be found in the three-dimensional case. The task is to transform from the system of measured variables (μ, ρ_e, df) to the material contributions of water (w), iodine (i) and calcium-oxalate (c). They are now expressed as vectors in the old (i.e. the measurement) basis system $B = (\vec{\mu}, \vec{\rho}_e, \vec{df})$ and written as columns of the matrix

$$\mathbf{B} = \begin{pmatrix} \mu_w & \rho_{e,w} & df_w \\ \mu_i & \rho_{e,i} & df_i \\ \mu_c & \rho_{e,c} & df_c \end{pmatrix}. \quad (5.33)$$

The second step is to find the transformation matrix \mathbf{T} . The new basis system $\tilde{B} = (\vec{w}, \vec{i}, \vec{c})$ which is spanned by the relative amount of the respective materials is a standard basis (\mathbf{I}) and therefore $\mathbf{B}^{-1} \mathbf{I} = \mathbf{B}^{-1} = \mathbf{T}$.

The inversion of a 3×3 matrix \mathbf{A} has a simple analytical solution

$$\mathbf{A}^{-1} = \begin{pmatrix} a & b & c \\ d & e & f \\ g & h & i \end{pmatrix}^{-1} = \frac{1}{\det A} \begin{pmatrix} ei - fh & ch - bi & bf - ce \\ fg - di & ai - cg & cd - af \\ dh - eg & bg - ah & ae - bd \end{pmatrix}, \quad (5.34)$$

with $\det A$ being the determinant of the matrix \mathbf{A} . Therefore, the transformation matrix \mathbf{T} can easily be found by inverting the matrix \mathbf{B} .

List of publications and scientific presentations

First-authored publications

E.-M. Braig, L. Birnbacher, F. Schaff, L. Gromann, A. Fingerle, J. Herzen, E. Rummeny, P. Noël, F. Pfeiffer, D. Muenzel. Simultaneous wood and metal particle detection on dark-field radiography. *European Radiology Experimental* 2, 1 (2018).

E.-M. Braig, J. Böhm, M. Dierolf, Ch. Jud, B. Günther, K. Mechlem, S. Allner, T. Sellerer, K. Achterhold, B. Gleich, P. Noël, D. Pfeiffer, E. Rummeny, J. Herzen, F. Pfeiffer. Direct quantitative material decomposition employing grating-based X-ray phase-contrast CT. *Scientific Reports* 8, 1 (2018).

E.-M. Braig and N. Roiser, M. Kimm, M. Busse, J. Andrejewski, J. Scholz, C. Petrich, A. Gustschin, A. Sauter, J. Bodden, F. Meurer, R. Korbel, F. Pfeiffer, J. Herzen, D. Pfeiffer. X-ray dark-field radiography: potential for visualization of monosodium urate deposition. *Investigative Radiology* 55, 8 (2020).

E.-M. Braig, D. Pfeiffer, M. Willner, T. Sellerer, K. Taphorn, Ch. Petrich, J. Scholz, L. Petzold, L. Birnbacher, M. Dierolf, F. Pfeiffer, J. Herzen. Single spectrum three-material decomposition with grating-based X-ray phase-contrast CT. *Physics in Medicine & Biology* 65, 18 (2020).

Co-authored publications

S. Kulpe, M. Dierolf, E.-M. Braig, B. Günther, K. Achterhold, B. Gleich, J. Herzen, E. Rummeny, F. Pfeiffer, D. Pfeiffer. K-edge subtraction imaging for coronary angiography with a compact synchrotron X-ray source. *PloS one* 13, 12 (2018).

K.Mechlem, T. Sellerer, S. Ehn, D. Münzel, E.-M. Braig, J. Herzen, P. Noël, F. Pfeiffer. Spectral angiography material decomposition using an empirical forward

model and a dictionary-based regularization. *IEEE transactions on medical imaging* 37, 10 (2018).

C. Jud, E.-M. Braig, M. Dierolf, E. Eggl, B. Günther, K. Achterhold, B. Gleich, E. Rummeny, P. Noël, F. Pfeiffer, D. Münzel. Trabecular bone anisotropy imaging with a compact laser-undulator synchrotron X-ray source. *Scientific reports* 7, 1 (2017).

K. Mechlem, S. Ehn, T. Sellerer, E.-M. Braig, D. Münzel, F. Pfeiffer, P. Noël. Joint statistical iterative material image reconstruction for spectral computed tomography using a semi-empirical forward model. *IEEE transactions on medical imaging* 37, 1 (2017).

K. Mechlem, S. Allner, S. Ehn, K. Mei, E.-M. Braig, D. Münzel, F. Pfeiffer, P. Noël. A post-processing algorithm for spectral CT material selective images using learned dictionaries. *Biomedical Physics and Engineering Express* 3, 2 (2017).

E. Eggl, K. Mechlem, E.-M. Braig, S. Kulpe, M. Dierolf, B. Günther, K. Achterhold, J. Herzen, B. Gleich, E. Rummeny, P. Noël, F. Pfeiffer, D. Münzel. Mono-energy coronary angiography with a compact synchrotron source. *Scientific reports* 7 (2017).

K. Scherer, E.-M. Braig, S. Ehn, J. Schock, J. Wolf, L. Birnbacher, M. Chabior, J. Herzen, D. Mayr, S. Grandl, A. Sztrókay-Gaul, K. Hellerhoff, F. Pfeiffer. Improved diagnostics by assessing the micromorphology of breast calcifications via X-ray dark-field radiography. *Scientific reports* 6 (2016).

E. Eggl, M. Dierolf, K. Achterhold, C. Jud, B. Günther, E.-M. Braig, B. Gleich, F. Pfeiffer. The munich compact light source: initial performance measures. *Journal of synchrotron radiation* 23, 5 (2016).

K. Scherer, K. Willer, L. Gromann, L. Birnbacher, E.-M. Braig, S. Grandl, A. Sztrókay-Gaul, J. Herzen, D. Mayr, K. Hellerhoff, F. Pfeiffer. Toward clinically compatible phase-contrast mammography. *PloS one* 10, 6 (2015).

K. Scherer, E.-M. Braig, K. Willer, M. Willner, A. Fingerle, M. Chabior, J. Herzen, M. Eiber, B. Haller, M. Straub, H. Schneider, E. Rummeny, P. Noël, F. Pfeiffer. Non-invasive differentiation of kidney stone types using X-ray dark-field radiography. *Scientific reports* 10, 6 (2015).

Oral presentations

Jan. 2017 – IMXP – *Improved foreign body detection with preclinical X-ray dark-field imaging*, Garmisch-Partenkirchen, Germany

Jan. 2018 – IMXP – *Recent milestones in grating-based X-ray phase-contrast mammography*, Garmisch-Partenkirchen, Germany

Jan. 2019 – IMXP – *Direct quantitative material decomposition with X-ray phase-contrast CT*, Garmisch-Partenkirchen, Germany

Aug. 2019 – SPIE – *Single-energy material decomposition with grating-based X-ray phase-contrast CT*, San Diego, California

Jan. 2020 – IMXP – *Detection of monosodium urate crystal deposition in X-ray dark-field radiography*, München, Germany

Poster presentations

Feb. 2017 – SPIE – *Preclinical X-ray dark-field imaging: Foreign body detection*, San Diego, California

Acknowledgements

The generous and motivating support of my supervisors, colleagues, family and friends enabled me to have the amazing opportunity to work in a unique, friendly and supportive research group on a fascinating topic. For this I would like to thank all these people.

Franz, thank you for giving me the opportunity to be a member of the Chair of Biomedical Physics already during my Bachelor studies. Since then I have profited a lot from the great scientific equipment, the incredible expertise of the whole group and equally from the unique friendly working atmosphere. Thank you for creating such an incredible working environment, for giving me the opportunity to be a part of this group and especially for supporting, advising and motivating me during the whole time.

Thank you, Julia, for your great support in all fields. You were always there to discuss experimental issues and to find solutions for all kinds of problems in the lab and everywhere else. By providing your enormous expertise you contributed a big part to the success of my experiments. Thank you for always supporting me in research and also personally! And thank you for great times in all of our group's social activities.

Daniela, it was great to have you as a mentor for my PhD project. You were always available for my questions, provided me great support for the interdisciplinary projects and you have inspired me with your uncomplicated, effective and super friendly manner. Thank you very much for your support, for the inspiration and for opening the clinical world up to me.

Thank you Peter, for all your help, for motivating me and for providing insights into the ways of some healthcare companies. It was always great fun to go on business trips and conferences with you. Thank you for always being supportive and open.

Klaus, thank you for helping me to find my way into the group through a large number of fish. Thank you for your never ending patience when supervising my first steps with the VtomeX, for sharing your knowledge and for making the 120

fish a funny and educative project. Further, I would like to thank you for all your support with administrative subjects, for taking care of our radiation safety and for making the safety instructions enjoyable.

Thanking you, Martin, is a never ending story. Thank you for your patient explanations, for establishing and maintaining an extraordinaire infrastructure at the chair. This concerns software and hardware documentation, managing the whereabouts of equipment and most important the maintenance of the chair's own IT infrastructure which allows convenient and efficient working from any workplace or even from the home office. I admire your dedication to science which is visible in form of an enormous knowledge - in theory and experiment, in your working hours but especially in your great support of everyone within the research group. Thank you, Martin, it was a great privilege to work with you and to learn from you!

Thank you Nelly for all your help with administration and thank you for sharing your talent to make bureaucracy less bureaucratic. Thank for all the nice talks at IPP and for surviving all the nerd chatter.

Thank you Bernhard, Veronica and Madleen for keeping the MSB alive, for your administrative support and for maintaining and supervising the security in the MSB labs.

I would like to thank the „IT- and Reco-guys“, Sebastian, Wolfgang and Lorenz H., for their patience and for their great support with reconstruction, programming and with all IT related issues. I really appreciate your selfless commitment to maintaining and enriching the software and IT-infrastructure of the chair. Without your help, my experiments would not have been possible.

Thorsten and Korbinian, thank you for a great PhD time, for a lot of fun at conferences and on business trips and for substantial contributions, corrections and feedback to my experiments and projects.

Thank you to all my office mates, more recently also Kirsten, Josef, Manuel and Johannes for making our office a very nice working space, for great discussions and for always being available for questions or support. Thorsten, Kirsten, Josef and Christoph, thank you for your help at the experimental setups and with proofreading the manuscripts and parts of my thesis. Lorenz B., thank you for all your input during the ancient Mammo project, your help with numerous measurements, for a lot of fun at the Lab or at the soccer field and also for your motivation and companionship during our time-extensive hobby. And thank you, Kai, for supervising both my Bachelor and my Master thesis, for always providing me great feedback and for all the fun time.

Thanks to all the people who helped me with proof-reading this thesis and the

related manuscripts. Thank you Benedikt, Jana, Josef, Kirsten, Korbinian, Lisa, Lorenz, Stephanie, Simone and Thorsten for your feedback on my thesis.

Thank you, Nathalie, for the great cooperation in the gout detection project. I really enjoyed working with you. A special thanks goes also to all our interdisciplinary cooperation partners in the clinics and also to Juliana for her help with the microsphere production.

Within my PhD project I was supported by two Master students, Stephanie and Jessica. I would like to thank you for your contributions, for your dedication and for your focused way of working. It was a pleasure working with you.

All together, I would like to thank the whole E17 family and all our relatives in the Klinikum or in different cooperation projects. I enjoyed working with all of you without exception. Thank you for the great time and for creating such an exceptionally collegial atmosphere.

Finally, I would like to thank my family, especially my parents, for their generous and loving support. Thank you for never putting any pressure on me, for giving me complete freedom and for making all these great experiences possible for me. Maxi, it was great to go the whole way together with you and to share all these experiences. I am not sure if I would have done it without you, thank you for everything!